

https://dspace.org/

Prediction of the initiation and orientation of the extension fractures ahead of and around faces and walls of mechanically driven excavations and their effect of stability

Mokgohloa, Matthews Chuene

2017

https://hdl.handle.net/10539/24196

Mokgohloa, Matthews Chuene (2017) Prediction of the initiation and orientation of the extension fractures ahead of and around faces and walls of mechanically driven excavations and their effect of stability, University of the Witwatersrand, Johannesburg, <http://hdl.handle.net/10539/24196>

Downloaded from a DSpace repository. https://dspace.org/

PREDICTION OF THE INITIATION AND ORIENTATION OF THE EXTENSION FRACTURES AHEAD OF AND AROUND FACES AND WALLS OF MECHANICALLY DRIVEN EXCAVATIONS AND THEIR EFFECT ON STABILITY

Matthews Mokgohloa

A research report submitted to the Faculty of Engineering and the Built Environment, University of the Witwatersrand, Johannesburg, in partial fulfilment of the requirements for the degree of Master of Science in Engineering.

Johannesburg, 2017

DECLARATION

I declare that this research report is my own, unaided work. It is being submitted for the Degree of Master of Science in the University of the Witwatersrand, Johannesburg. It has not been submitted before for any degree or examination in any other University.

……

(Signature of candidate)

…… day of …..... (Year) …..

at ……...

ABSTRACT

Boring of shafts and tunnels in hard rock mines is more prevalent in recent years in South Africa. This normally takes place under substantial stress conditions, where fracturing of rock occurs around the boundaries and ahead of advancing faces of excavations. Fracturing can have a significant impact on boring activities, in some instances causing sidewall spalling which can be extensive, with machine grippers unable to reach the sidewalls. In brittle rock, these fractures are commonly extensional in nature.

This research has been undertaken to predict the initiation of extension fractures and their orientations ahead of machine driven tunnels. Furthermore, it will help to assess the stability of the excavations, by evaluating the potential for slab/plate failures. This was based on the typical in situ stress fields for underground deep level mines.

The numerical analyses involved the generation of different plots:

- Principal stress contour plots, depicting stress distributions around and ahead of tunnel excavation, using cutting planes;
- Isosurfaces, showing zones of extension or potential extents of fracturing, applying the extension strain criterion; and
- Trajectory ribbons, to demonstrate the orientations of fractures.

Based on the results of the stress analyses, potential slab or plate formation was determined. It was noted that the fracture zone is a function of a tunnel size. For instance, a four-metre diameter tunnel is less likely to give boring problems than an eight-metre diameter tunnel.

The failure of the tunnels was predicted by employing slab analysis methods. An eight-metre diameter tunnel had slenderness ratio as low as 22.3 as compared with a four-metre diameter tunnel with a slenderness ratio of 27. Looking at buckling stress versus slenderness ratio, this translates to buckling stress values of above 100 MPa for an eight-metre tunnel and to values just below 50 MPa for a four-metre tunnel.

The outcome of the research gives a clear indication that boring activities could be undertaken under severe conditions. This could be detrimental to the cutter head, since large slabs and blocks could be encountered during boring. The results of this research can be beneficial in the evaluation of boring conditions prior to and during boring activities.

ACKNOWLEDGEMENTS

I would like to express my sincere appreciation for the assistance and support rendered by the following persons and institution:

1) Professor T.R. Stacey for his supervision, guidance, encouragement and inspiration throughout this research.
2) University of the Witwatersrand for giving me the opportunity to embark on this research.
3) Family and friends for their motivation and support.

TABLE OF CONTENTS

Contents Page

DECLARATION ..... **I**

ABSTRACT ..... **II**

ACKNOWLEDGEMENTS ..... **IV**

LIST OF FIGURES ..... **IX**

LIST OF TABLES ..... **XVII**

LIST OF SYMBOLS ..... **XVIII**

CHAPTER 1 ..... **1**

INTRODUCTION **1**

1.1 Background 1

1.2 Definition of the Problem 3

1.3 Research Questions 6

1.4 Objectives 7

1.5 Research Methodology 7

1.6 Content of the Report 8

CHAPTER 2 ..... **10**

FACTORS AFFECTING STABILITY OF MECHANICAL EXCAVATIONS AND PREDICTION OF EXTENSION FRACTURES **10**

2.1 Introduction 10

2.2 Mechanical Excavations 11

2.2.1 Raise boring technology 11
2.2.2 Tunnel boring 14
2.3 Factors Affecting Stability of the Excavations 16
2.3.1 Stress distributions 17
2.3.2 Fracture initiation and propagation in the rock 23
2.4 Prediction of Fractures 35
2.4.1 Mohr and Griffith criteria 35
2.4.2 Extension strain criterion 38
2.5 Conclusion 40

CHAPTER 3 41
APPLICATION OF EXTENSION STRAIN CRITERION 41
3.1 Introduction 41
3.2 Uses of Extension Strain Criterion 41
3.2.1 Laboratory studies 42
3.2.2 In situ studies 42
3.2.3 Numerical studies 43
3.3 Conclusion 46

CHAPTER 4 47
THE IMPACT OF THE EXTENSION FRACTURES 47
4.1 Introduction 47
4.2 Failure of the Excavations by Fracturing 47
4.3 Effects of Fracturing on Boring Machines 62
4.4 Case Studies 66

4.4.1. Introduction 66

4.4.2. In situ monitoring of rock-burst nucleation and evolution in the deeply buried tunnels of Jinping II hydropower station (Li et al, 2012) 66

4.4.3. Rock burst and slabbing failure and its influence on TBM excavation at headrace tunnels in Jinping II hydropower station (Gong et al, 2012) 73

4.4.4. Engineering geology of Alpine tunnels: past, present and future (Loew et al, 2010) 76

4.5 Conclusion 79

CHAPTER 5 ..... **81**

NUMERICAL MODELLING AND MODELLING METHODOLOGY **81**

5.1 Introduction 81

5.2 Numerical Modelling Methods 82

5.3 Modelling Methodology 83

5.4 Conclusion 85

CHAPTER 6 ..... **86**

RESULTS OF NUMERICAL MODELLING AND DISCUSSION **86**

6.1 Introduction 86

6.2 Stress Distributions around Excavations 86

6.2.1 Analyses results for an eight-metre diameter tunnel (σ_x= 70 MPa, σ_y= 35 MPa, σ_z= 70 MPa) 90

6.2.2 Analyses results for an eight-metre diameter tunnel (σ_x= 35 MPa, σ_y= 35 MPa, σ_z= 70 MPa) 93

6.2.3 Analyses results for an eight-metre diameter tunnel (σx= 52.5 MPa, σy= 25 MPa, σz= 70 MPa) 97

6.2.4 Analyses results for an eight-metre diameter tunnel (σx= 35 MPa, σy= 17.5 MPa, σz= 52.5 MPa) 101

6.2.5 Analyses results for an eight-meter diameter tunnel (σx= 52.5 MPa, σy= 70 MPa, σz= 25 MPa) 105

6.2.6 Summary of the results 109

6.3 Predicted Zone of Extension 111

6.4 Orientation of Extension Fractures 122

6.5 Potential Slab for Buckling 132

6.6 Conclusion 143

CHAPTER 7 ..... **144**

CONCLUSIONS **144**

REFERENCES **147**

APPENDIX **162**

8.1 Isosurfaces Depicting Areas of Extension and Summary of Results from Examine3D 162

LIST OF FIGURES

FIGURES

Figure 1.2.1: Stress fracturing around a deep stope mined in strong, brittle quartzite (Jager and Ryder, 1999)..... 5
Figure 2.2.1: a) Raise Boring b) Down Reaming c) Blind Boring (Ferreira, n.d.) 13
Figure 2.2.2: The relationship between boring rate and stress level (Wesseloo and Stacey, 2000) 16
Figure 2.3.1: In situ stress data for South African mines (Wesseloo and Stacey, 2006)..... 18
Figure 2.3.2: An illustration of the front and rear regions with respect to the tunnel face location together with critical stress paths and the representative points, A, B, C and D (Read, et al., 1998). 20
Figure 2.3.3: Examples of tunnel instability and brittle failure as a function of Rock Mass Rating (RMR) and the ratio of the maximum far-field stress σ) to the unconfined compressive strength (σ_c) (Martin et al. 1998)..... 22
Figure 2.3.4: a) Borehole break-out b) Tunnel wall break-out. c) Micro-slabbing deterioration of crown pillar d) Initiation of micro-slabbing (Ortlepp, 1997)..... 25
Figure 2.3.5: Mechanism of brittle fracture under multi-axial compression, (Bieniawski, 1967a)..... 26
Figure 2.3.6: Stress-strain diagram showing the phases of crack formation (Nicksiar and Martin, 2012) 29
Figure 2.3.7: Tensile crack initiation, strain localization and peak strength for Lac du Bonnet granite from tests from Hoek and Martin (2014) by Lau and Gorski (1992). 31
Figure 2.3.8: Tensile crack initiation in various rocks from Nicksiar and Martin (2013), modified by Hoek and Martin (2014)..... 32

Figure 2.3.9: A 3-D representation of a wing growth as an extension of initial crack (Dyskin and Salganik, 1987) 33
Figure 2.3.10: Crack propagation from stress rotation: (a) rotation of σ1 and σ3; (b) rotation of σ3 and σ2 (Diederichs et al, 2004) 34
Figure 3.2.1: Prediction of fracture in layered media (Steffanizzi, et al., 2007)..... 44
Figure 3.2.2: FRANCOD models of the Beaumont tunnel fracturing for $\sigma_h/\sigma_v = 0.33$ (Barton and Shen 2017) 45
Figure 3.2.3: FRANCOD models of the Beaumont tunnel fracturing for $\sigma_h/\sigma_v = 2$ (Barton and Shen 2017) 45
Figure 4.2.1: Buckling stress versus slenderness ratio for buckling failure using Euler's formula (Kazakidis, 2002) and (Iannacchione, et al., 1998)..... 51
Figure 4.2.2: Notation for defining a local change in wall thickness (Krenzke and Charles, 1963). 53
Figure 4.2.3: Development of Slabs around underground openings (McGarr, 1997)..... 54
Figure 4.2.4: The outline of the slab with thickness (h) and dimension (L) and applied stress (S) (McGarr, 1997). 55
Figure 4.2.5: True triaxial loading-unloading tests showing the formation of extension fractures and slabs (Qiu, et al., 2014)..... 57
Figure 4.2.6: The development of slabbing, buckling and rock bursting (Qiu et al, 2014) 58
Figure 4.2.7: An elliptical model showing fracturing zone and rock slabs that occurred near the deep level tunnels (Qiu, et al., 2014) 59
Figure 4.3.1: Examples of spalling resulting from crack growth (Diederichs, 2007). 65
Figure 4.4.1: Three-dimensional numerical model of tunnels in the rock-burst test zone (Li et al, 2012). 68
Figure 4.4.2: Numerical simulation of tunnel excavation at the horizontal a) Distribution of failure approach index (FAI—Failure

Approach Index), b) Distribution of the maximum principal stress (σ1) (Li et al, 2012)..... 69
Figure 4.4.3: Layout of monitoring facilities around test tunnels B and F in Jinping II hydropower station (Li et al, 2012)..... 70
Figure 4.4.4: Sketch plan of crack development measured at different times: a) before excavation; b) excavation of top heading of test tunnel F complete; c) 10.0 m of bench excavated, before rock-burst; (d) 21.0 m of bench excavated, before rock-burst (Li et al, 2012). 71
Figure 4.4.5: Phenomena of rock burst and spalling in the field (Gong, et al., 2012). 74
Figure 4.4.6: Slabbing characteristics of rock samples (Gong et al., 2012)..... 75
Figure 4.4.7: Increasing levels of brittle spalling and operational challenges: a) spalling initiation (small scales on the wall); b) spalling pieces of grain thickness penetrating into wall; c) parallel wall slabs; d) strain bursting of spall damaged ground due to high stresses (Loew et al, 2010)..... 78
Figure 4.4.8: Spalling and energetic slab generation behind TBM shield (Loew, et al. 2010). 79
Figure 6.2.1: The perspective view depicting the cutting planes of σ1 distribution plots on an eight-metre diameter tunnel. 89
Figure 6.2.2: The perspective view depicting the cutting planes of σ3 distribution plots on an eight-metre diameter tunnel. 89
Figure 6.2.3: Top view of cutting plane depicting σ1 distribution through the roof of an eight-metre diameter tunnel (σx= 70 MPa, σy= 35 MPa, σz= 70 MPa). 90
Figure 6.2.4: Front view of the cutting plane depicting σ1 distribution through a section of an eight-metre tunnel (σx= 70 MPa, σy= 35 MPa, σz= 70 MPa) 91

Figure 6.2.5: Front view of cutting plane depicting σ3 distribution through a section of an eight-metre tunnel (σx= 70 MPa, σy= 35 MPa, σz= 70 MPa). 92
Figure 6.2.6: Top view of cutting plane depicting σ3 distribution through the roof of an eight-metre diameter tunnel (σx= 70 MPa, σy= 35 MPa, σz= 70 MPa). 93
Figure 6.2.7: Front view of cutting plane depicting σ1 distribution through a section of an eight-metre diameter tunnel (σx= 35MPa, σy= 35 MPa, σz= 70 MPa). 94
Figure 6.2.8: Top view of cutting plane depicting σ1 distribution through the roof of an eight-metre diameter tunnel (σx= 35 MPa, σy= 35 MPa, σz= 70 MPa). 95
Figure 6.2.9: Front view of cutting plane depicting σ3 distribution through a section of an eight-metre diameter tunnel (σx= 35 MPa, σy= 35 MPa, σz= 70 MPa). 96
Figure 6.2.10: Top view of cutting plane depicting σ3 distribution through the roof of an eight-metre diameter tunnel (σx= 35 MPa, σy= 35 MPa, σz= 70 MPa). 97
Figure 6.2.11: Front view of cutting plane depicting σ1 distribution through a section of an eight-metre diameter tunnel (σx= 52.5 MPa, σy= 25 MPa, σz= 70 MPa)..... 98
Figure 6.2.12: Top view of cutting plane depicting σ1 distribution through the roof of an eight-metre diameter tunnel (σx= 52.5 MPa, σy= 25 MPa, σz= 70 MPa)..... 99
Figure 6.2.13: Front view of cutting plane depicting σ3 distribution through a section of an eight-metre diameter tunnel (σx= 52.5 MPa, σy= 25 MPa, σz= 70 MPa)..... 100
Figure 6.2.14: Top view of cutting plane depicting σ3 distribution through the roof of an eight-metre diameter tunnel (σx= 52.5 MPa, σy= 25 MPa, σz= 70 MPa). 101

Figure 6.2.15: Front view of cutting plane depicting σ1 distribution through a section of an eight-metre diameter tunnel (σx= 35 MPa, σy= 17.5 MPa, σz= 52.5 MPa)..... 102
Figure 6.2.16: Top view of cutting plane depicting σ1 distribution through the roof of an eight-metre diameter tunnel (σx= 35 MPa, σy= 17.5 MPa, σz= 52.5 MPa)..... 103
Figure 6.2.17: Top view of cutting plane depicting σ3 distribution through the roof of an eight-metre diameter tunnel (σx= 35 MPa, σy= 17.5 MPa, σz= 52.5 MPa)..... 104
Figure 6.2.18: Front view of cutting plane depicting σ3 distribution through a section of an eight-metre diameter tunnel (σx= 35 MPa, σy= 17.5 MPa, σz= 52.5 MPa)..... 105
Figure 6.2.19: Top view of cutting plane depicting σ1 distribution through a section of an eight-metre diameter tunnel (σx= 52.5 MPa, σy= 70 MPa, σz= 25 MPa)..... 106
Figure 6.2.20: Front view of cutting plane depicting σ1 distribution through a section of an eight-metre diameter tunnel (σx= 52.5 MPa, σy= 70 MPa, σz= 25 MPa)..... 107
Figure 6.2.21: Top view of cutting plane depicting σ3 distribution through a section of an eight-metre diameter tunnel (σx= 52.5, MPa, σy= 70 MPa, σz= 25 MPa)..... 108
Figure 6.2.22: Front view of cutting plane depicting σ3 distribution through a section of an eight-metre diameter tunnel (σx= 52.5 MPa, σy= 70 MPa, σz= 25 MPa)..... 109
Figure 6.3.1: The predicted failure depth for different stress ratios for Poisson's ratio of 0.2. 114
Figure 6.3.2: The predicted failure depth for different stress ratios for Poisson's ratio of 0.2. 114
Figure 6.3.3 The predicted failure depth for different stress ratios for Poisson's ratio of 0.3. 115

Figure 6.3.4: The predicted failure depth for different stress ratios for Poisson's ratio of 0.3. 115
Figure 6.3.5: Isosurfaces of fracture/crack initiation for a six-metre diameter tunnel according to extension strain criterion for Poisson's ratio of 0.2 a) top view of the tunnel b) side view of the tunnel and c) frond view of the tunnel (σx= 70 σy= 35 σz= 70). 116
Figure 6.3.6: Isosurfaces of fracture/crack initiation for an eight-metre diameter tunnel according to extension strain criterion for Poisson's ratio of 0.2, a) top view of the tunnel b) side view of the tunnel c) front view of the tunnel (σx= 70 σy= 35 σz= 70). 117
Figure 6.3.7: Isosurfaces of fracture/crack failure on an eight-metre diameter tunnel according to extension strain criterion for Poisson's ratio of 0.2, a) top view of the tunnel b) side view of the tunnel c) front view of the tunnel (σx= 70 σy= 35 σz= 70). 118
Figure 6.3.8: Isosurfaces of fracture/crack initiation for a six-metre diameter tunnel according to extension strain criterion for Poisson's ratio of 0.3, a) top view of the tunnel b) side view of the tunnel c) front view of the tunnel (σx= 70 σy= 35 σz= 70). 119
Figure 6.3.9: Isosurfaces of fracture/crack initiation for an eight-metre diameter tunnel according to extension strain criterion for Poisson's ratio of 0.3, a) top view of the tunnel b) side view of the tunnel c) front view of the tunnel (σx= 70 σy= 35 σz= 70). 120
Figure 6.3.10: Isosurfaces of fracture/crack failure an eight-metre diameter tunnel according to extension strain criterion for Poisson's ratio of 0.3, a) top view of the tunnel b) side view of the tunnel c) front view of the tunnel (σx= 70 σy= 35 σz= 70). 121
Figure 6.4.1: Orientations of fractures around an eight-metre diameter tunnel depicting σ1 values (σx= 70 MPa, σy= 35 MPa and σz= 70 MPa). Stress units above are MPa. 123

Figure 6.4.2: Orientations of fractures around an eight-metre diameter tunnel depicting σ1 values (σx= 35 MPa, σy= 35 MPa and σz= 70 MPa). Stress units above are MPa. 124
Figure 6.4.3: Orientations of fractures around an eight-metre diameter tunnel depicting σ1 values (σx= 52.5 MPa, σy= 25 MPa and σz= 70 MPa). Stress units above are MPa. 125
Figure 6.4.4: Orientations of fractures around an eight-metre diameter tunnel depicting σ1 values (σx= 35 MPa, σy= 17.5 MPa and σz= 52.5 MPa). Stress units above are MPa. 126
Figure 6.4.5: Orientations of fractures around an eight-metre diameter tunnel depicting σ1 values (σx= 35 MPa, σy= 70 MPa and σz= 35 MPa). Stress units above are MPa 127
Figure 6.4.6: A vertical section across an eight-metre diameter tunnel depicting orientations of fractures on the footwall and hangingwall (σx= 70, σy= 35, σz= 70). 128
Figure 6.4.7: A vertical section across an eight-metre tunnel depicting orientations of fractures on the footwall and hangingwall (σx= 35 σy= 35, σz= 70) 128
Figure 6.4.8: A vertical section across an eight-metre diameter tunnel depicting orientations of fractures on the footwall and hangingwall (σx= 52.5 σy= 25, σz= 70). 129
Figure 6.4.9: A vertical section across an eight-metre diameter +tunnel depicting orientations of fractures on the footwall and hangingwall (σx= 35 σy= 17.5, σz= 52.5). 129
Figure 6.4.10: A vertical section across an eight-metre diameter tunnel depicting orientations of fractures on the sidewall (σx= 52.5 MPa σy= 70 MPa, σz= 25 MPa). 130
Figure 6.4.11: A vertical section across an eight-metre diameter tunnel depicting orientations of fractures on the sidewall (σx= 35 MPa σy= 70 MPa, σz= 35 MPa). 131

Figure 6.5.1: The potential slab geometry and the magnitudes of acting stresses depicted by contours for a six-metre diameter tunnel. 134
Figure 6.5.2: The potential slab geometry and the magnitudes of acting stresses depicted by contours for an eight-metre diameter tunnel. ... 135
Figure 6.5.3: Buckling stress versus slenderness ratio for buckling failure. 136
Figure 6.5.4: Buckling stress versus slenderness ratio for buckling failure 137
Figure 6.5.5: Determination of critical slenderness ratio for buckling analysis under eccentric load. 140
Figure 6.5.6: Determination for critical slenderness ratio of buckling analysis under eccentric load. 141
Figure 8.1.1: Isosurfaces of fracture/crack initiation for an eight-metre tunnel for Poisson's ratio of 0.2. 162
Figure 8.1.2: Isosurfaces of fracture/crack initiation for an eight-metre tunnel for Poisson's ratio of 0.2. 163
Figure 8.1.3: Isosurfaces of fracture/crack initiation for an eight-metre tunnel for Poisson's ratio of 0.2. 164
Figure 8.1.4: Isosurfaces of fracture/crack initiation for an eight-metre tunnel for Poisson's ratio of 0.3. 165
Figure 8.1.5: Buckling stress versus slenderness ratio for buckling failure using 166
Figure 8.1.6: Isosurfaces for critical strain of 200 microstain on a four-metre tunnel depicting fractured zone 168
Figure 8.1.7: Isosurfaces for critical strain of 200 microstain on a six-metre tunnel depicting fractured zone 168
Figure 8.1.8: Isosurfaces for critical strain of 200 microstain on a six-metre tunnel depicting fractured zone. 169

LIST OF TABLES

TABLE

Table 2.4.1: Critical values of extension strain (Stacey, 1981)..... 39
Table 4.2.1: Rock material parameters Qiu et al (2014)..... 61
Table 6.2.1: Input parameters of material properties obtained from literature..... 87
Table 6.2.2: Alternative in-situ stress fields obtained from Wesseloo and Stacey (2006). 88
Table 6.2.3: Modelling parameters used in Examine3D..... 88
Table 6.3.1: Summary of in situ stresses, Poisson's ratio and predicted Failure Depth 113
Table 6.5.1: Summary of slab thickness, slenderness ratios and buckling stresses. 135
Table 6.5.2: Summary of slab thickness, slenderness ratios, buckling stresses..... 136
Table 6.5.3: Results for eccentric load approach for the determining maximum compressive and tensile stresses for σx=35 MPa, σy = 35 MPa, σz= 70 MPa..... 139
Table 6.5.4: Results for eccentric load approach for the determining maximum compressive and tensile stresses for σx = 70 MPa, σy = 35 MPa, σz = 70 MPa..... 140
Table 6.5.5: Input parameters for analysis for buckling. 141
Table 8.1.1: Summary of slab thickness, slenderness ratios, buckling stresses..... 166
Table 8.1.2: Summary of the results from Examine3D 167

LIST OF SYMBOLS

SA	South Africa
3D	Three-dimensional
D	Diameter of tunnel
E	Static Young's modulus
G	Shear modulus
P_{cr}	Critical Load
PGV	Peak Ground Velocity
PPV	Peak Particle Velocity
t	Slab thickness of a test specimen
UCS or σ_c	Uniaxial compressive strength
$\Delta V/V$	Volumetric strain
LSR	Lateral Strain response
ε_3	minimum principal stress
ε_c	Critical extension strain
τ	Shear stress
ρ	Density

υ	Poisson's ratio
σ_1	Major principal stress
σ_2	Intermediate principal stress
σ_3	Minor principal stress
UTS	Uniaxial Tensile strength
σ_x	In situ horizontal stress
σ_y	In situ vertical stress
σ_z	In-situ horizontal stress

CHAPTER 1

INTRODUCTION

1.1 Background

Underground hard rock deep level mining in South Africa (SA) is undertaken to extract minerals such as gold, copper and platinum. SA gold and platinum deposits are amongst the world's richest deposits, originating from conglomerates of the Witwatersrand Basin and pyroxenites of the Bushveld Complex, which extend to depths of several kilometres (Durrheim, 2010). These orebodies are relatively easy to mine because of their tabular geometry and extraction is predominantly by means of conventional mining methods such as up-dip mining, scattered mining, long-wall mining, and sequential grid mining (Jager and Ryder, 1999). Access to the production sections is by means of vertical or decline shafts, through footwall haulages and crosscuts, and until the on-reef raises.

The majority of platinum and gold mining is still labour intensive, extraction is by means of handheld machines for drilling, and rock breakage is by means of explosive agents. Scraper winches do cleaning and transportation is, mainly, by battery-powered locomotives. With depths of gold mines, in particular, in the range of 2200m to 3900m, this poses serious challenges in terms of safety, profitability, infrastructure, and energy and labour costs. At these depths, there are high rock stresses, which have significant effects on stability of access tunnels and the ore extraction areas (stopes). These high rock stresses cause stress-induced failures such as rock bursts, which are sudden and uncontrolled failures (Aglawe, 1999). According to Durrheim

(2010) when greater depths are reached, with extensive stoping, mining-induced seismicity, which results in rock bursts, is encountered. Moreover, rock bursts continue to pose substantial risk in deep level mining operations, claiming the lives of mineworkers. Regardless of all the technical initiatives, rock bursts are still regarded as one of the least understood challenges.

South African gold and platinum mining industries generated R49 billion and R58 billion of revenue respectively, with 30% of the world gold resources and just less than 90% of the world platinum reserves (van der Merwe, 2011). These sectors (platinum and gold) contributed 22% and 11% to total gross domestic product (GDP), respectively (Chamber of Mines, 2015). In the 1980's gold, in particular, was SA's most important export commodity, however, presently it is ranking number four in the export market (Vogt, et al., 2015). Given that there is no control over commodity prices, the most profitable solution is to improve productivity, which can be achieved through employing new technology (Vogt, 2015). The existing mining methods are repetitive, non-continuous, and depend on equipment such as scraper winches, which have inadequate volume capacity and are not efficient. Therefore, substantial research is required to come up with designs, planning and mining methods to improve productivity.

In recent years, different technological solutions have been trialled to solve problems of deep to ultra-deep mining, for instance, rock cutting, mechanisation and automation (Pickering, 1996). In this research, circular openings, raises and tunnels produced by raise boring machines (RBM) and tunnel boring machines (TBM), are considered. Tunnel boring has proven to be popular in civil engineering, and raise boring is widely used in the mines in South Africa. There are advantages and disadvantages in using TBM's (Maidl, et al., 2008):

1. Advantages

- Higher advance rate;
- Precise excavation outline;
- Automated and continual working process;
- Low labour cost and
- Better working conditions and safety

2. Disadvantages

- Thorough geological data and investigation are important compared with the requirements of drilling and blasting;
- Longer lead time for design and assembly of the machine;
- Thorough planning required;
- Machine transportation with trailers to the tunnel entrance and
- Utilisation of the machine in adverse conditions, such as changing rock types and large water accumulations, is limited.

As far as raise boring is concerned, there are initiatives taking place: AngloGold Ashanti's Technology Innovation Consortium has confidence in reef boring, and it is regarded as the future solution to its deep level underground mining (Vogt, et al., 2015). In this type of boring only gold reef is mined.

1.2 **Definition of the Problem**

Some of the challenges pertaining to deep level underground mining include rock fracturing, spalling, buckling, strain bursting, etc. These challenges manifest because of, excavations being driven in highly stressed rock masses. In the process, fracturing of the rock takes place, adding to existing natural fractures. The coalescence of fractures forms networks of fracture surfaces, which are formed ahead of and around faces and walls of the excavations, under high or low stress conditions (Ortlepp and Stacey, 1994; Aglawe, 1999).

Daehnke et al. (2000) identified the three most prevalent discontinuity types in intermediate and deep level gold mine stopes, namely:

- Shear fractures, which are fractures related to highly stressed rock and are initiated six to eight metres ahead of the excavation face. They are oriented subparallel to the excavation face and are commonly spaced one to three metres apart and normally dip at 60 to 70 degrees;

- Extension fractures, which are initiated ahead of the excavation face and are formed after shear fractures have been propagated, and they terminate on parting planes. They are normally spaced some ten centimetres apart, dipping between 60 and 90 degrees. The direction of dip can be dictated by the hanging and footwall rock types; and

- Bedding planes

Moriya, et al. (2015) also identified macroscopic fractures, which occur as a result of high stress levels around the mining front, called vertical and secondary extension fractures. These types of fractures are said to be formed by the tensile failure of the rock near the excavation face when there is no confinement, and their presence compromises the stability of the excavations. Shear fractures (Ortlepp Shears) form as far as tens of metres ahead of the excavation face. These types of fractures are said to be associated with violent seismic events. Figure 1.2.1 illustrates different types of fractures that can be expected at great depths in hard rock mine stopes.

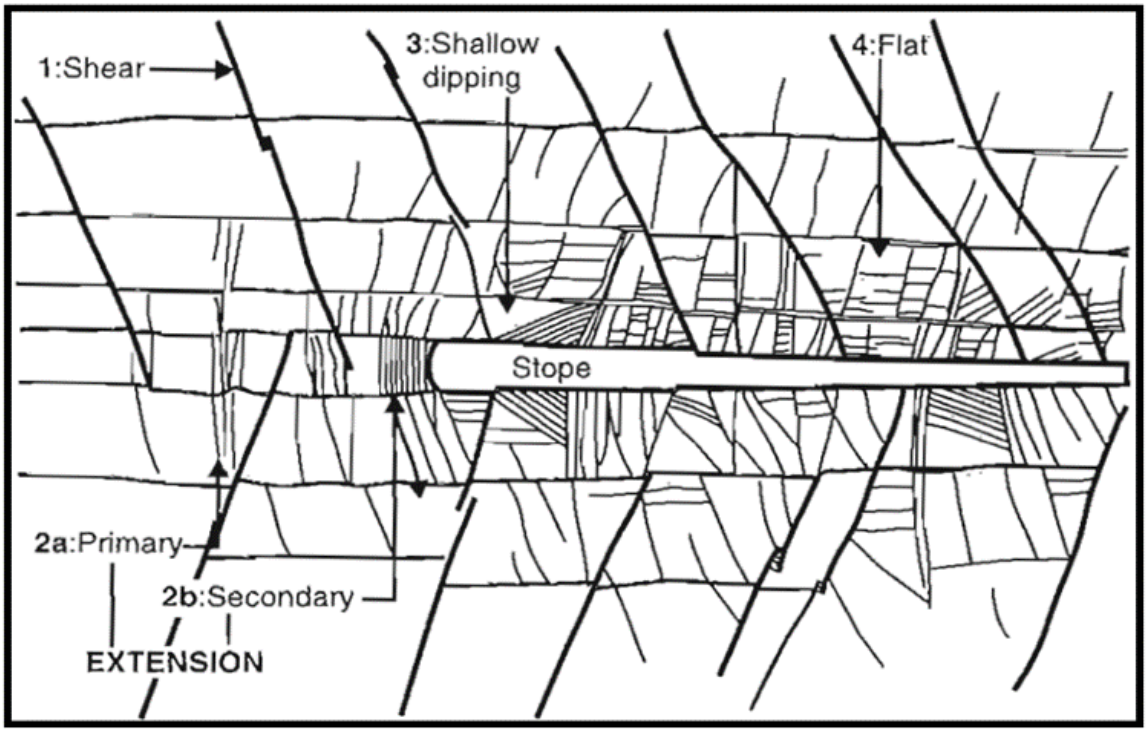


Figure 1.2.1: Stress fracturing around a deep stope mined in strong, brittle quartzite (Jager and Ryder, 1999)

The impact of such fractures can be detrimental to mining activities, resulting in unpredicted failures. This is evident in the case study described by Ortlepp and Stacey (2000), where a sudden failure occurred in a development of a main haulage at a depth of 2800 m, excavated in competent quartzite rock. This resulted in a self-mined tunnel, forming a cavity about 16 m long with the dimensions of the blasted haulage. The following were believed to have transpired, which led to the failure:

- An abnormal stress concentration existed in, or surrounding, a zone where cavity was formed;
- There was a release of high pressure gas;
- Extension fractures developed in the rock directly ahead of the face, oriented sub-parallel to the plane of the face creating thin slabs;

- The presence of high pressure gas and high stress facilitated the buckling and ejection of these plates and
- The formation of the cavity was a continuous process, which started from the newly created tunnel face, progressing to the end of the cavity.

It is clear that the creation or advancement of the tunnel into the critical extension zones facilitates free surfaces, surrounded by the unstable plates, which buckle out, with possibility of strain bursting.

Presently, there is no publication that has been reported, that deals with the behaviour of the excavations in deep level hard rock mining being affected by, for instance, extension fractures (their locations, orientations, etc.) and some of the occurrences discussed above. Therefore, knowledge, in this regard, can assist engineers to effectively implement mechanical mining (TBM or RBM) methods. For instance, spalling and slabbing of rocks from the sidewalls of bored tunnels, which can lead to rock bursting in some cases, can be predicted in advance, to formulate mitigating measures to prevent premature failure due to such occurrences.

1.3 **Research Questions**

When excavations are created underground, there is stress redistribution. Due to the triaxial compressive nature of the surroundings, there will always be zones of extension strain. When these excavations are driven in these conditions, fractures are initiated and may propagate and coalesce to form plate or slab surfaces. Depending on the stress conditions in the planes of these plates, if the critical instability point is reached, failure can occur in the form of buckling or strain bursting, depending on the amount of the energy stored in the rock mass. In the case of boring activities, excessive

bursting can have a negative impact on the machine utilization, resulting in low advance rates and possible machine damage.

This research was undertaken to answer the following questions:

- What effects do the in situ stress field and stress distributions have on rock fracturing?
- Can initiated fractures (extension fractures), their orientations and impact be predicted?

1.4 **Objectives**

The objectives of this research are to:

- Determine the stress distributions ahead of a tunnel using three dimensional (3D) stress analyses, (Examine 3D modelling software), for a range of in situ stress conditions;
- Determine the predicted zones of extension and define the potential failure volume at risk;
- Determine the induced principal stresses in the tunnel face area and hence the orientation of the potential extension fractures, together with the volume at risk;
- Predict the potential for rock bursting due to buckling of "plates" of rock defined by the geometry of the extension fracturing, and
- Estimate the energy, stored within the volume at risk, which will be released when a burst occurs.

1.5 **Research Methodology**

The research was conducted in the following manner:

a. A detailed literature review was conducted focusing on extension fracture initiation, propagation and prediction, in relation to

different in situ stress fields, and on the processes of strain bursting (beam/plate failure);

b. Numerical modelling (analysis), using Examine 3D, was conducted to:

- Analyse the stress distributions ahead of tunnels of different dimensions, under different in situ stress fields;
- Determine the zones of extension and interpret the critical zones;
- Identify the orientations of the extension fractures in these zones, and
- Determine the potential thicknesses of the plates/slabs, or the extent of blockiness and the possible instability (buckling and strain bursting).

c. Case studies relating to rock fracturing in both raise and tunnel boring, to contextualise the impact of extension fractures, for instance, stability of excavations, TBM utilization etc., were analysed.

1.6 **Content of the Report**

Chapter 2 presents a background literature review of mechanical excavations (raise boring and tunnel boring). The effect of stress distribution as excavations are created and advanced are discussed. In addition, the stability problems in these excavations and the criteria used to predict fracture initiations are outlined. In Chapter three applications of extension strain criterion, as one of the criteria used to predict extension fractures, are discussed. Whereas in Chapter four the impacts of extension fractures on stability of excavations, are discussed, as well as case studies emphasizing the behaviour of excavations under different stress levels. In Chapter five numerical modelling concepts, relevant to rock engineering, are discussed. Results of numerical modelling are presented in Chapter six. The

findings of the research and conclusions are provided in Chapter seven. Two appendices are included in this research report. Appendix A provides the stress distribution plots for different size tunnels, and Appendix B provides the Isosurfaces depicting areas of extension from Examine 3D.

CHAPTER 2

FACTORS AFFECTING STABILITY OF MECHANICAL EXCAVATIONS AND PREDICTION OF EXTENSION FRACTURES

2.1 Introduction

The continuous increase in competition and a high demand for metals, emphasize the need to improve the present deep level mining operations (Skawina et al, 2014). According to Pickering (1996), mining starts with the removal of the "easy" resources and advances to the more difficult ones. This compels the mining industry to employ advanced planning and technology, if mining costs are to be contained. Pickering et al (2006) further stated that mining by blasting is inherently cyclic, which puts the mining under severe limitations in terms of rate of face advance that can be attained and subsequently, the utilization of the invested capital is compromised. In order to overcome these constraints, narrow reef hard rock mining must follow the lead of the soft rock mining industry, by employing rock-cutting technology, known as mechanical mining. This can be defined as excavation by means of machines, which transfer energy as a force from cutting tools to the rock (Bilgin et al, 2014).

Rock cutting technology was introduced to serve as a selective mining method applicable to narrow reef mines, where less rock is removed from the stope, in order to improve working conditions (Joughin, 1976). This approach relies on the stress to fracture the rock at the face, with

a slot being cut into the weakened rock by the machine. Moreover, more experience has been attained in this regard. Pilot production trials having been completed, which resulted in production of about 30 000 metre square (m^2) without the use of explosives.

Trials have been conducted in both gold and platinum narrow reef mining industries, in order to evaluate the feasibility of mechanical mining. It is worth evaluating the usage of both tunnel boring machines (TBM) and raise borers (RBM), in order to appreciate their popularity and shortcomings under the current narrow reef mining conditions. Factors related to these mining methods, for instance, rock and rock mass behaviour in terms of fracturing, stress distributions, safety and profitability of mining, etc. are discussed in this chapter.

2.2 **Mechanical Excavations**

As far as this research report is concerned, the type of mechanical excavations that are discussed are, those driven by raise and tunnel boring technologies.

2.2.1 Raise boring technology

According to Bilgin et al (2014), the raise boring technology was established to fulfil the needs of underground mining industry. It also gained popularity in various applications in tunnelling for ventilation requirements and in very hard rock environments for development of deep shafts. It offers a safe way of excavating a shaft between two levels of a mine without the use of explosives. The boring operation involves the drilling of a small pilot hole, which is then reamed in one or more phases to the preferred dimensions. There are four ways of

excavating shafts by mechanical excavation technology (Bilgin et al 2014):

- Raise Boring

In this method, the pilot hole is drilled to the lower level, where, on holing, the drill bit is replaced by the reamer head, which is attached to the drill rod and drawn up, with the drill string in tension. The broken (bored) rock is collected at the bottom, driven by gravity.

- Down Reaming

In this method, the pilot hole is drilled to hole into the lower access level, and the reamer head is then pushed downwards.

- Box-holing

This method is an alternative to raise boring and it is used when there is not enough space between two levels that are to be connected.

- Drilling blind shaft with V Mole

In this method, a pilot hole is not necessary, and the shaft is bored using a cone-shaped boring head. These methods are shown in Figure 2.2.1

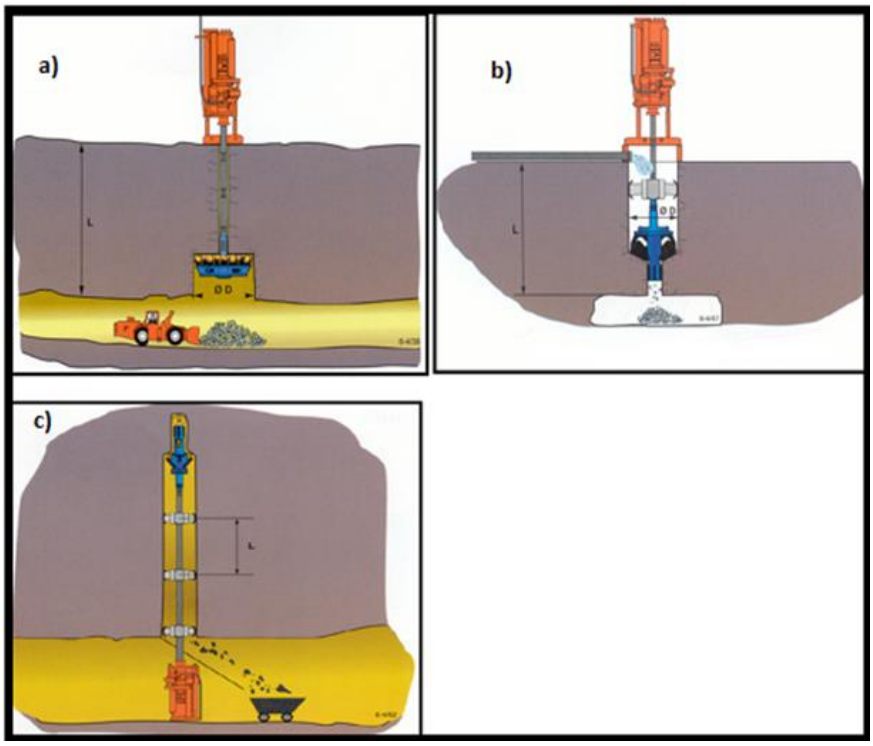


Figure 2.2.1: a) Raise Boring b) Down Reaming c) Blind Boring (Ferreira, n.d.)

In the early 1980's, diameters of raise bored holes varied from 1.2m to 2.44m, with a maximum of 3.6m, but in recent years, due to advancement of technology, diameters can be as high as 6m. Increasing raise bore hole diameters present instability problems to the walls and advancing face of the raise (McCracken and Stacey, 1989). Therefore, knowledge of the structural and strength properties of the rock mass and the in-situ stress conditions are essential prior to excavation of the raise.

The concept of mechanical mining, of tabular reef has been trialled. Stacey (1982) discussed the concept of stopecoring as an alternative to conventional drill and blast method for mining of narrow tabular reef. Crowley (2014) stated that AngloGold Ashanti Ltd, anticipated to prolong the life of its SA mines by at least 30 years by means of reef-

boring technology that contributes new ore from pillars in previously mined areas. The boring machines are able to remove the gold-bearing ore from the reef, backfilling the bored holes with high strength concrete as means of support. These machines allow ore from mined-out areas, in dangerous working places, where reserves have been written off, to be recovered. According to Nemanashi (2014), the method requires initial boring of parallel holes using a raise boring machine, and backfilling of these holes. The reef between the holes is subsequently bored out using the same technique, and the holes backfilled, which provides the required stability.

2.2.2 Tunnel boring

Since the introduction of TBMs in the 1950s, many boring projects have been completed successfully, such as construction of tunnels for traffic, hydropower, sewerage and water, underground storage and mining (Zheng et al, 2016). The advancement of technologies offered TBMs comparative advantage in achieving tunnels of different diameters over ground conditions varying from hard rock to soft soil and mixed grounds.

TBMs must be selected carefully, so that they are able to perform as per the anticipated ground conditions (Toan, 2006). According to Cigla et al (2001) it is clear that selecting TBMs over the drill and blast method has a huge economic impact, hence adequate mine planning and detailed performance analysis are crucial. In the same light Brox (2013) stated that there must be thorough mine planning, which takes place prior to the selection of the excavation method. This involves an appropriate level of geotechnical analysis, including the following:

- Geological considerations;
- Identification of prominent faults and shear zones;

- Drilling of investigation holes at the tunnel entrances, to obtain core samples for rock testing, to determine the strength and boreability; and
- Analysis of the rock mass genesis along the tunnel configuration.

Regarding mechanical mining technology, there are some aspects that have detrimental effects on its success, which must be considered. Fracturing and failure of strong rock, whether under high (Stacey and De Jongh,1977) or low stress (Stacey and Yathavan, 2003), present major challenges in rock boring:

- The instability of the surrounding rock;
- Potential buckling (failure) of the rock and possible rock bursting;
- Excessive support requirements, resulting in high cost implications and major production delays, and
- Reduced TBM or raise boring machine utilisation (excessive vibration and wear of the cutter head), which can result from fractures being induced ahead of the face.

According to Lee et al, (2004) rock masses in their natural form are in a state of stress equilibrium, until they are disturbed by an artificial excavation or natural disaster, such as a bore or an earthquake. Subsequently, there is a redistribution of stress because of the change in the state of equilibrium. The remaining rock mass would undergo excessive loading, and its surfaces would be displaced. Under these severe stress conditions, fracture of the rock would occur around the excavation and ahead of the face, causing spalling and breakouts or 'dog ears'. Fracturing can have a substantial effect on the rate of advance of a boring machine, as illustrated in Figure 2.2.2, which indicates the impact of stress level on boring rate. It can be noted that boring rate is plotted against stress levels, and two scenarios are represented, one for good quality jointed rock mass and the other for

massive rock mass. The interest in this research report is on the massive rock, where boring rate seemed to be constant, until high stress zones are reached and stress induced failures are initiated, which, have an impact on tunnel and raise boring activities.

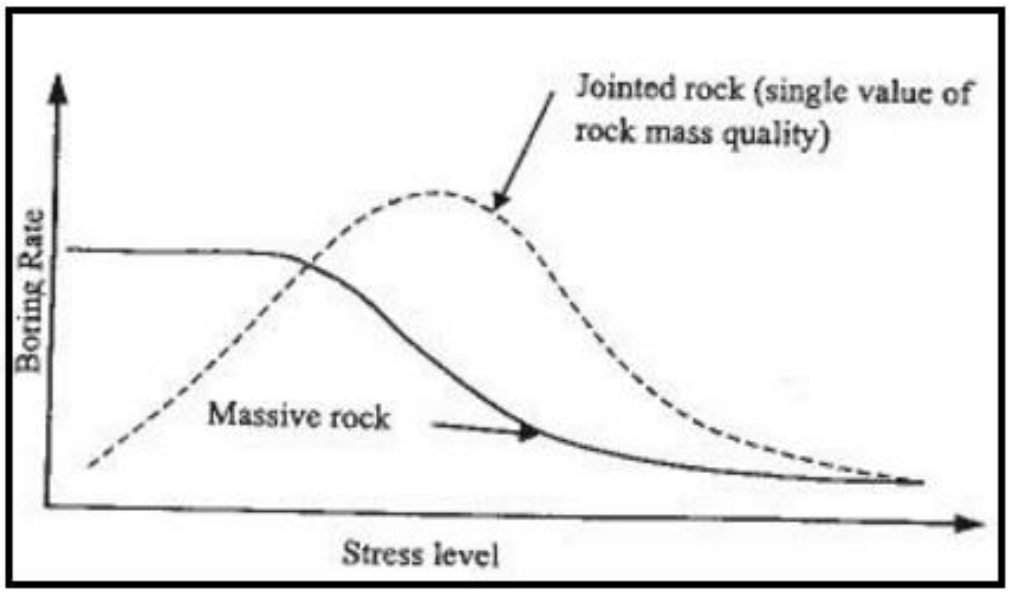


Figure 2.2.2: The relationship between boring rate and stress level (Wesseloo and Stacey, 2000)

It is now clear that the stress distribution (as a result of an excavation being driven in a rock mass), and associated fracture genesis, fracture initiation and propagation, play a pivotal role in stability assessment of excavations. The following sections outline these concepts in detail.

2.3 Factors Affecting Stability of the Excavations

The stability of underground openings in hard rock depends on the in situ stress magnitudes and the characteristics of the rock mass. At low in situ stress magnitudes, the stability is dependent on the continuity and distribution of the natural joints in the rock mass. With an increase in in situ stress magnitudes, the rock mass stability is

dependent on new stress-induced fractures around excavation boundary (Martin et al, 1998). Therefore, in order to appreciate the behaviour of excavations under different stress fields, the factors in the following sub-sections must be explained:

2.3.1 Stress distributions

Rock masses at great depths are subjected to stresses emanating from the weight of the overlying strata and those originating from the earth's crust. According to Jager and Ryder (1999) the magnitude of the vertical element (σ_v) of the virgin stress is a function of the density of the overburden rock (ρ), gravitational acceleration (g) (9.81 m/s^2) and the depth below surface (H), i.e., $\sigma_v = \rho gH$. According to Wesseloo and Stacey (2006), from mine planning perspective, in situ stress is an important parameter in modelling of excavations: if invalid assumptions are made, this could compromise the excavation stability and safety. Hence, a database of in-situ stress measurements across SA was created and the results of this investigation, applicable to platinum and gold mines in particular, are shown in Figure 2.3.1.

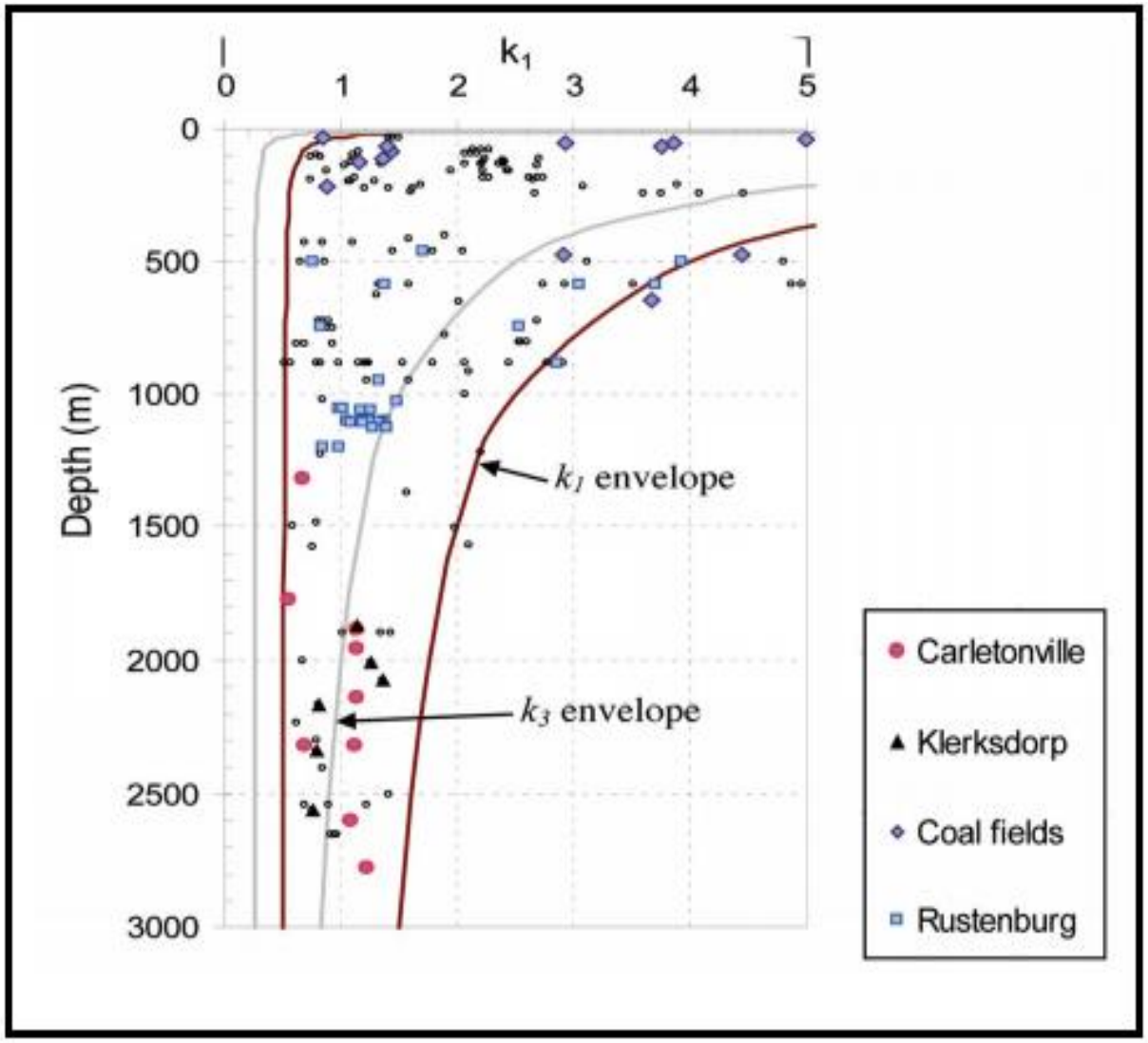


Figure 2.3.1: In situ stress data for South African mines (Wesseloo and Stacey, 2006)

When an excavation is created in a rock mass, there is a significant redistribution of the stress field, which results into a new set of stresses adjacent to the excavation (Hoek, 1987). Moreover, zones of compressive and tensile stress are formed, which could potentially exceed the host rock strengths. This could lead to fractures forming in the surrounding rock, resulting in buckling from the excavation surface. Zheng et al (1989) indicated that boreholes driven into a rock

mass, which is exposed to stresses that are of similar magnitudes to the strength of the rock, might cause the rock to fail adjacent to the borehole surface. In his study, Eberhardt (2001) pointed out that, in a stressed rock mass, the sequencing and advancement of a tunnel face results in the disturbance and redistribution of the original in situ stress field. This disturbance encompasses both alterations in magnitude and direction of the stress-field tensor in the vicinity of the tunnel boundary, which in turn play a role in the development of fractures and rock mass instability. Further away from an excavation surface, the stress tensor ultimately returns to in situ state. Similar work has been recorded by Abel and Lee (1973) and Martin (1997).

According to Martin et al (1998) the intact rock properties (rock stiffness, brittleness and its ability to store stain energy) and the fracture network determine the behaviour mechanism of the excavated opening, which could result in failure due to low or high stress magnitudes. Stacey and Yathavan (2003) indicated, as well, that stress induced fracturing does not only occur in high stress situations, but can also be observed even at low stress levels. They reported number of case studies which emphasised the issue of low ratios of major principal stresses to rock strengths (σ_1/ σ_c), in some cases as low as 0.1. This showed the potential for failure in cases where the in-situ stress levels are as low as 4% of the rock mass strength.

According to Read et al (1998), when a tunnel is created in a stressed rock mass there is a concentration of compressive stresses tangential to the excavation. The stress distribution depends on the magnitude and orientation of the applied stresses relative to the tunnel configuration and the shape of the excavation. Figure 2.3.2 was used to demonstrate the stress distribution after an opening has been created and advanced.

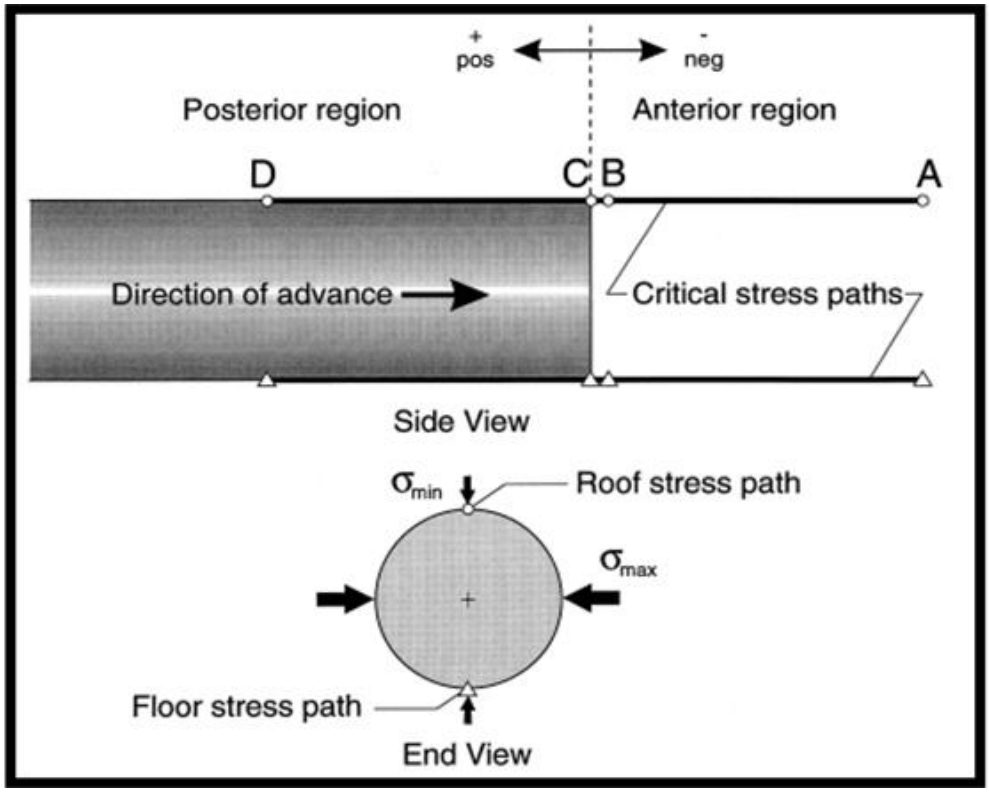


Figure 2.3.2: An illustration of the front and rear regions with respect to the tunnel face location together with critical stress paths and the representative points, A, B, C and D (Read, et al., 1998).

Viewing Figure 2.3.2, it can be noticed that the rock mass stress direction related to the tunnel excavation is distributed in two parts: the front element taking place ahead of the tunnel face position, and the rear element taking place behind the tunnel face position. Applied stress at a point ahead of the tunnel face undergoes an increase, then a decrease, together with variation in principal stress direction. Behind the face, on tunnel boundary, the radial stress is zero, and the tangential stress is directly proportional to the distance from the face, reaching the highest value as the plane strain environment is attained.

Points A, B, C and D (both in front and rear regions) indicate critical stress paths, which are parallel to the excavation boundaries on both sides. Subject to the position and intensity of the stress variations in this area of the rock mass, the rock would undergo failure or de-stressing, eventually resulting in a decrease in cohesive strength (Read et al., 1998).

Kaiser et al (2000) further explained that, failure of underground excavations in hard rock mining depends on the in situ stresses and the rock mass properties (the intact rock strength and the fracture formation). At relatively low stress conditions, failure is dictated by the concentration and distribution of natural fractures, whereas, as the stress magnitudes increase the natural fractures are clamped together and result in brittle failure associated with newly formed stress-induced fractures developing parallel to the excavation boundary. Martin et al (1998) emphasised the importance of the ratio of the field stresses and the strength of the rock mass relative to tunnel stability and ultimate failure, as shown by Figure 2.3.3. Zheng et al (1989) analysed the breakout developments in boreholes, as a result of stress redistribution. It is believed that the breakout in the borehole is a result of the enlargement of the cross section of the borehole in the direction of the minimum principal (compressive) stress normal to the borehole axis. Moreover, such breakouts are valuable indicators of the direction of the maximum compressive stress normal to the axis of the borehole. Their shapes may give an indication of the magnitudes of both the maximum and minimum stresses relative to the strength of the rock.

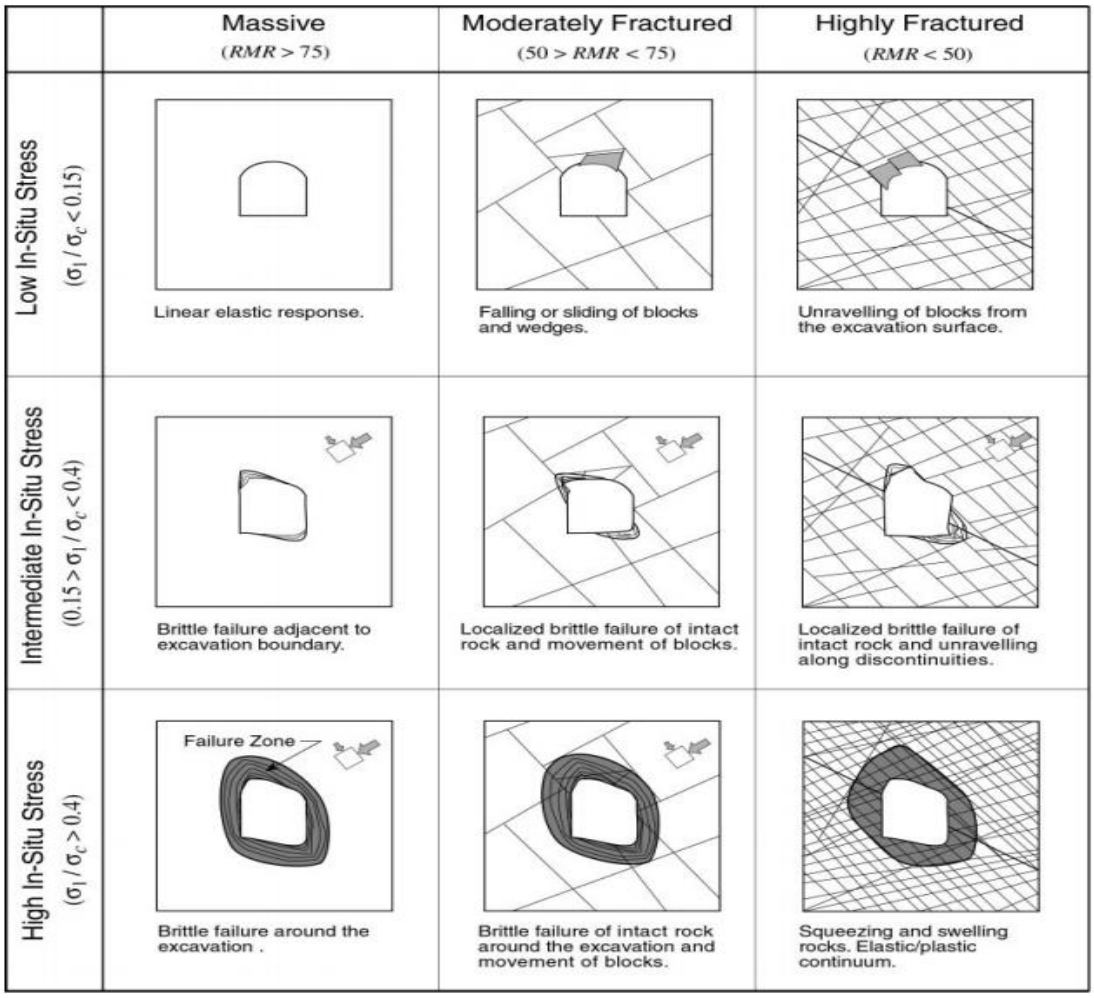


Figure 2.3.3: Examples of tunnel instability and brittle failure as a function of Rock Mass Rating (RMR) and the ratio of the maximum far-field stress σ) to the unconfined compressive strength (σ_c) (Martin et al. 1998)

Figure 2.3.3 is by Martin et al. (1998), and was modified from Hoek et al. (1995). It can be seen that, a rock mass quality is indicated by rock mass rating (RMR), which extends from zero to one hundred. The greater value of the RMR denotes a better quality of the rock mass.

Kaiser and McCreath (1994) pointed out that any excavation in rock, regardless of how it is excavated, changes the pre-existing stress field,

and causes rock mass deformation, possibly leading to rock mass failures. This behaviour depends on the magnitude of the induced stresses in relation to the rock mass strength. In essence, prior to any excavation, the stability of the openings must be assessed, and if there is any anticipation of failure, appropriate measures must be taken. This implies that, in boring projects, rock mechanics considerations must entail several machine performance aspects such as drillability or boreability of the rock, to determine the rate of penetration and tool wear.

Boring of shafts, orepasses and other service openings by mechanical means, at great depths, where rock mass is extremely stressed, has become common in recent years (Wesseloo and Stacey, 2000). Under these adverse conditions, fracturing of the rock takes place around the excavation and ahead of the face, resulting in surface spalling, breakouts or 'dog ears' and possible violent failure. This has proven to have significant effects on the rate of advance of the boring machine.

Understanding of the magnitudes and orientations of the in-situ and induced stresses is vital for underground excavation design. Most importantly, the behaviour mechanism must be identified, together with the appropriate criteria, to prevent incorrect predictions, which may have serious consequences on the behaviour and stability of the excavations.

2.3.2 Fracture initiation and propagation in the rock

According to Stacey (1981) fracturing is the failure process by which new surfaces, in the form of cracks, are formed, or the extension of existing cracks in a material. Ortlepp (1997) explains fracturing as the inception of a new surface of discontinuity through a previously intact portion of the rock, which excludes sliding or separation across a pre-

existing surface such as a joint or bedding plane. In this regard, extension fracturing is said to be the most likely mechanism of failure of intact rock under the conditions existing around artificial structures at all depths in the earth's crust. Figure 2.3.4 illustrates this failure mechanism. Where a). shows a borehole breakout, with evidence of extension fractures being parallel to the notch surface, b). shows the tunnel wall breakout as a result of fracture initiation by buckling and spalling of micro-slabs along the maximum stress direction, c). shows micro-slabbing deterioration of a crown pillar as a result of extension fractures extending away from the notch, and its tip progressing upwards, and d). indicates extent of the blanched polished surface showing how it delineates the progress of the micro-slabbing notch which initiates the primary extension slabbing.



Figure 2.3.4: a) Borehole break-out b) Tunnel wall break-out. c) Micro-slabbing deterioration of crown pillar d) Initiation of micro-slabbing (Ortlepp, 1997)

According to Bieniawski (1967a), there are four stages of fracture development in rocks under multiaxial compression, as illustrated in Figure 2.3.5. They are as follows:

I. Crack closure (closing of cracks);

II. Fracture initiation (linear elastic deformation);

III. Critical energy release (stable fracture propagation);

IV. Strength failure at maximum stress (unstable fracture propagation) and

V. Rupture at maximum deformation (Separating and coalescence of cracks)

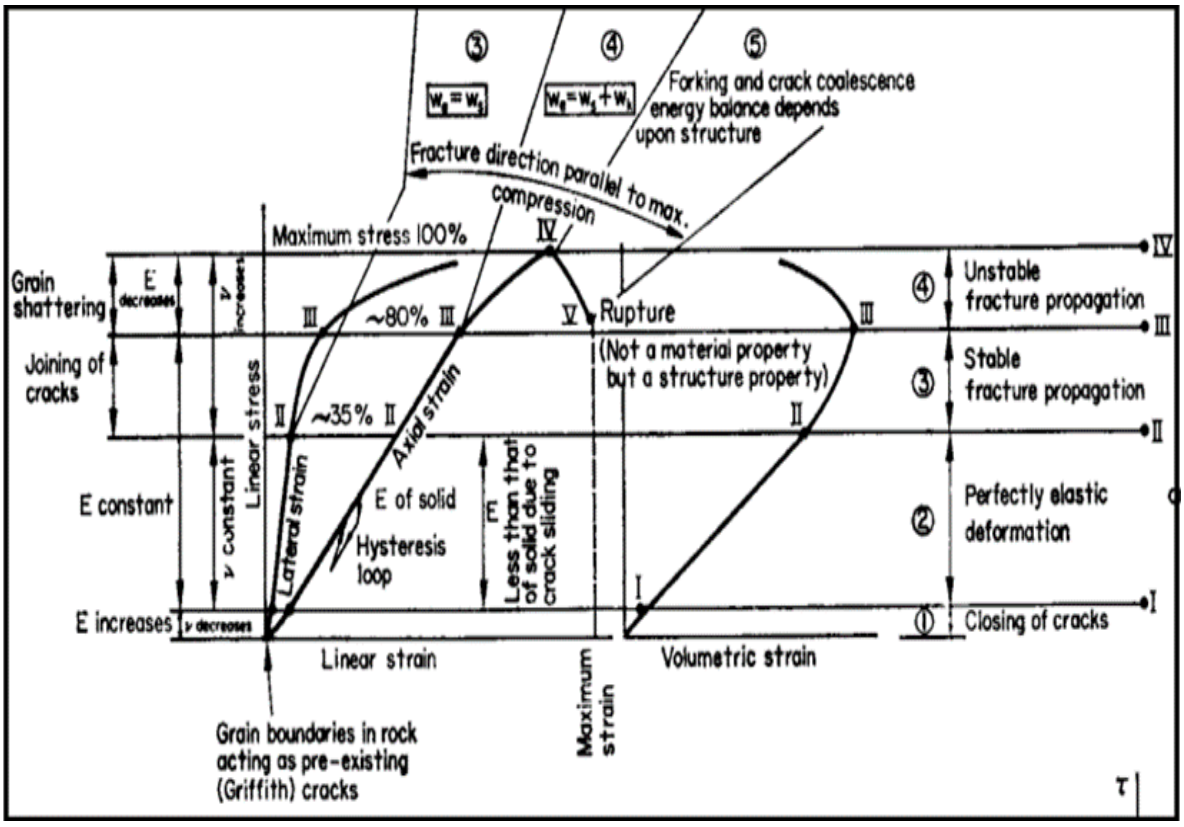


Figure 2.3.5: Mechanism of brittle fracture under multi-axial compression, (Bieniawski, 1967a)

The newly formed surfaces (cracks) undergo the following stages during their formation, (Bieniawski, 1967c):

- Fracture initiation stage, which is the failure process whereby fractures are initiated by the extension of pre-existing cracks in a material, and
- Fracture propagation stage, which is the failure process by which initiated fractures are extended in a material. The propagation process can either be stable or unstable depending on loading.

Nicksiar and Martin (2012) evaluated several methods for the determination of crack initiation by considering the stress-strain response. Similar approach to Bieniawski (1967a) was followed, as illustrated in Figure 2.3.5 in both confined and unconfined tests for less-permeable rocks.

These methods, referred to by Nicksiar and Martin (2012), have been used to establish the load related to the start of crack initiation during laboratory compression loading. They have been, to a large extent, dependent on the measured strains, i.e. the volumetric strain or lateral strain, which are as follows:

a) Volumetric strain methods

These methods were initially used by Brace et al (1966) in their studies to determine the start of dilatancy in compression tests of granite, marble and alpite. The stress-strain responses of these rock samples were observed, and the start of the dilatancy was established by using volumetric strain, which would indicate crack initiation. Due to visible shortcomings, these methods were later modified by Martin and Chandler (1994) by determining crack initiation from a graph of crack volumetric strain $(\Delta V/V)_{cr}$ versus axial strain, as illustrated in Figure 2.3.6(a). The values of crack volumetric strains are determined by subtracting elastic volumetric strain $(\Delta V/V)_{el}$ from calculated volumetric strains $(\Delta V/V)$:

$$\left(\frac{\Delta V}{V}\right)_{cr} = \frac{\Delta V}{\mathrm{V}} - \left(\frac{\Delta V}{V}\right)_{el} \quad \text{.....(1)}$$

$$\left(\frac{\Delta V}{V}\right)_{el} = \frac{2v-1}{E}(\sigma_1 + 2\sigma_3) \quad \text{.....(2)}$$

Where

V= Original volume of a specimen

ΔV= change in volume of a specimen

(E and v) = Elastic constants

(σ_1 and σ_3) = Principal stresses

b) Lateral strain methods

Lateral strain methods gained their popularity due to their responsiveness, relative to axial strain, to the growth of cracks, in determining the crack initiation stress, as shown in Figure 2.3.6 a). Moreover, lateral strain explicitly delineates the start of cracking; hence, its ratio with axial stress is plotted against axial stress, where the change indicates crack initiation as shown in Figure 2.3.6 b).

c) Acoustic emission method

Eberhardt, et al. (1998) consider this technique as an abrupt discharging of stored elastic strain energy as a result of disturbances, variation of grain boundary, or onset and growth of fractures through mineral grains, where it is perceived as an acoustic occurrence. This technique is illustrated in Figure 2.3.6 c), where a dotted tangent line represents the crack initiation stage.

d) Proposed lateral strain response (LSR) method

As already mentioned regarding the sensitivity of the lateral strain to the start of the crack initiation, it is then recommended to be used to determine the stress level, at crack initiation. Hence, the LSR method is used to explain the start of the unstable crack development from zero load to the beginning of the unstable crack development. The results are compared with a theoretical reference line drawn from the start of the unstable crack development to zero loading. Subsequently the difference is plotted against the axial stress, and the optimal difference is regarded as the of the crack initiation. This is illustrated in Figure 2.3.6 d).

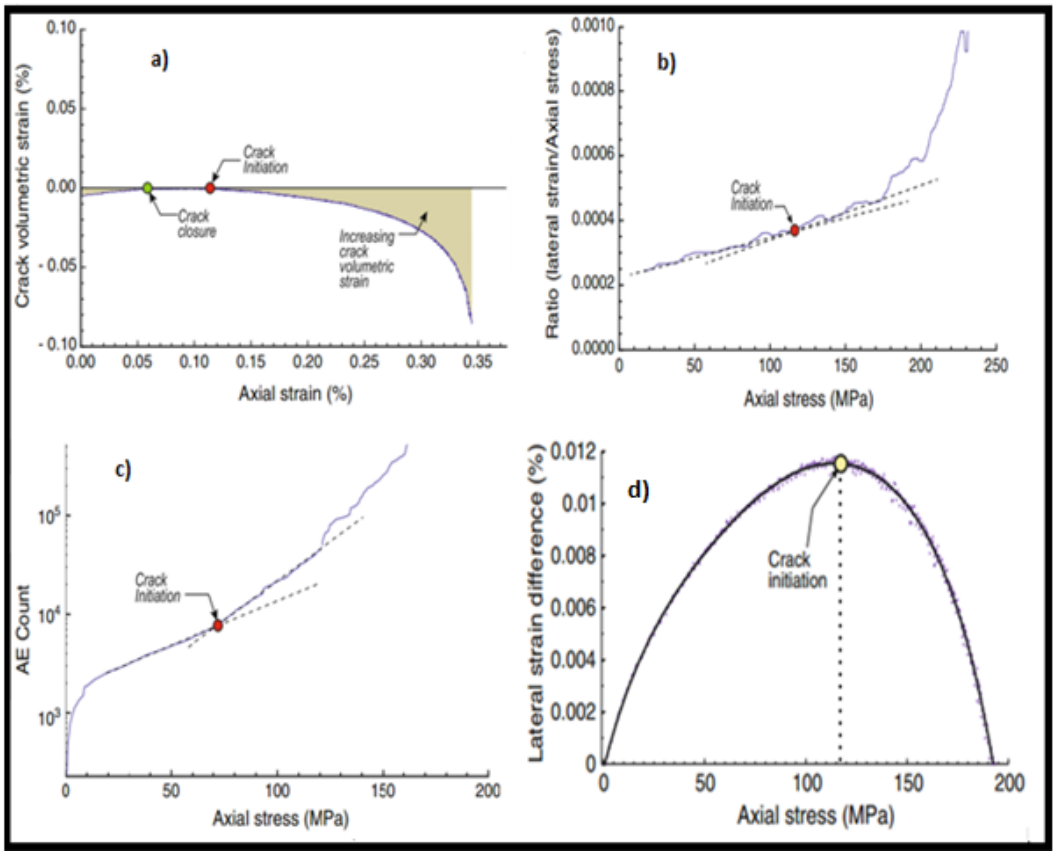


Figure 2.3.6: Stress-strain diagram showing the phases of crack formation (Nicksiar and Martin, 2012)

Lau and Gorski (1992), in their study, used strain and acoustic emission measurements, to determine the crack initiation, onset of strain localization and peak strengths for each loading pressure in a variety of triaxial tests (Hoek and Martin, 2014). These tests were carried out in a servo-controlled stiff testing machine, related to the procedure summarized in Figure 2.3.5 by Bieniawski, (1967a). The results of these tests to determine the point at which crack initiation occurs are shown in Figure 2.3.7. Martin and Chandler (1994) established that if there are no in situ results, Figure 2.3.5 could be taken as a guide to define the spalling strength of rocks, which can be expressed as a fraction of the UCS of the rock. In recent studies, Nicksiar and Martin (2013) gathered the crack initiation stresses for a range of different rock types, to illustrate the relationship between UCS and the crack initiation stress, as shown in Figure 2.3.8.

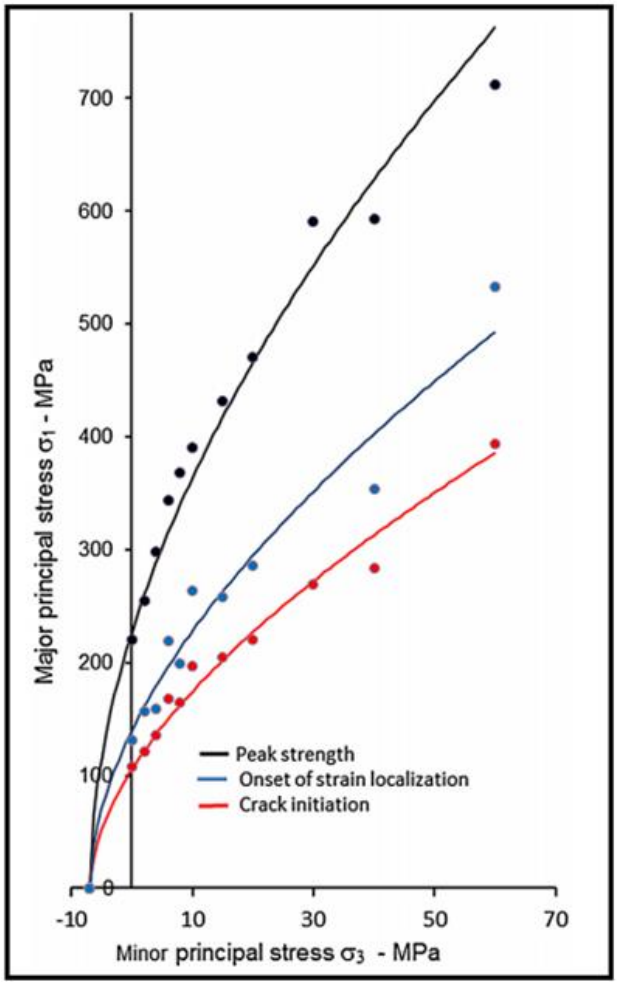


Figure 2.3.7: Tensile crack initiation, strain localization and peak strength for Lac du Bonnet granite from tests from Hoek and Martin (2014) by Lau and Gorski (1992).

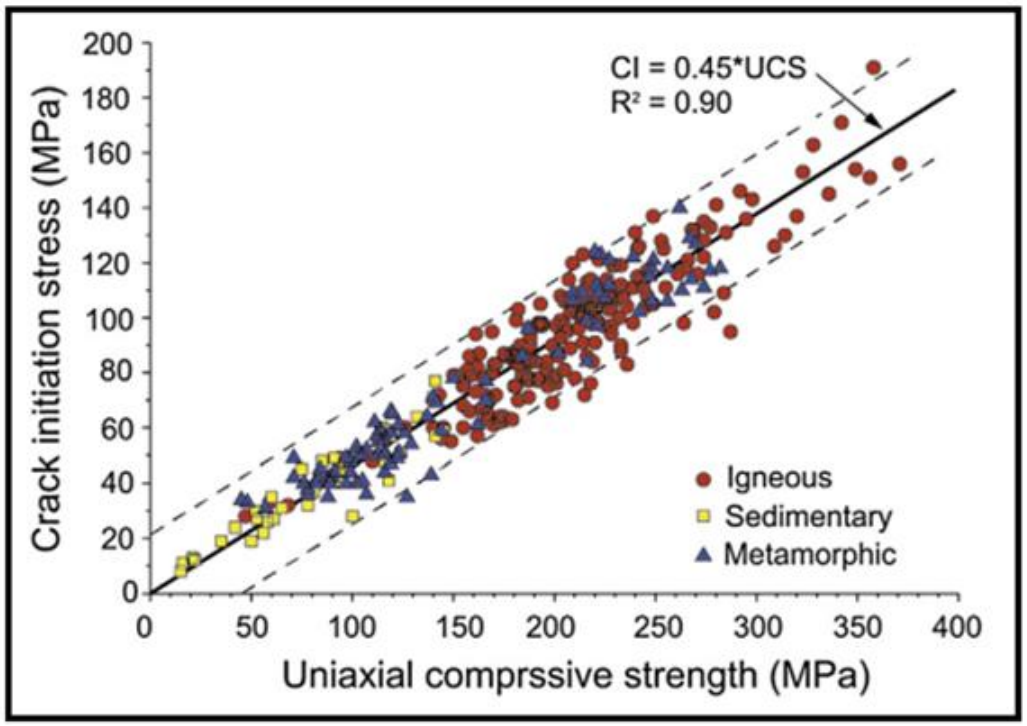


Figure 2.3.8: Tensile crack initiation in various rocks from Nicksiar and Martin (2013), modified by Hoek and Martin (2014).

According to Dyskin et al (2003) failure of brittle heterogeneous materials such as rocks, is dictated by crack development, which can result in volume increase together with acoustic emission. Moreover, it is believed that brittle rocks may contain a large number of natural internal cracks or weak micro-surfaces, which can develop into cracks when under stress. They explained the concept of opening up failure type of pre-existing cracks, oriented at an angle to compression axis, by using a two-dimension (2-D) simulation. They concluded that the increase in volume was directly proportional to uniaxial compression stress to the power three. However, in reality, natural cracks are three dimensional, which project a different mode of failure, i.e. called wing crack growth. In this instance, the volume increase is directly

proportional to cube root of the uniaxial stress to the power five. This is illustrated in Figure 2.3.9.

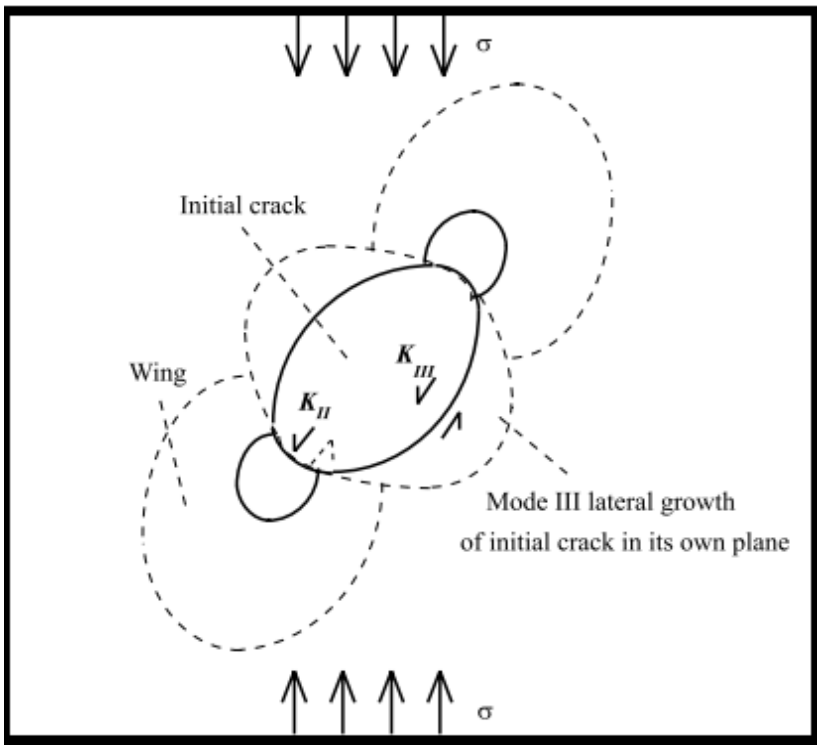


Figure 2.3.9: A 3-D representation of a wing growth as an extension of initial crack (Dyskin and Salganik, 1987)

Diederichs et al. (2004) explained the concept of stress rotation during tunnel development, which has an impact on the condition of crack propagation. Figure 2.3.10 a) and b) illustrate this concept, where minor principal (σ3) and major principal (σ1) stresses are rotated, forming crack extension and, similarly, intermediate stress (σ2) and (σ3) are rotated, forming "penny" shaped cracks. When these stresses return to their original orientations, the crack formation process repeats itself, resulting in cracks growing further.

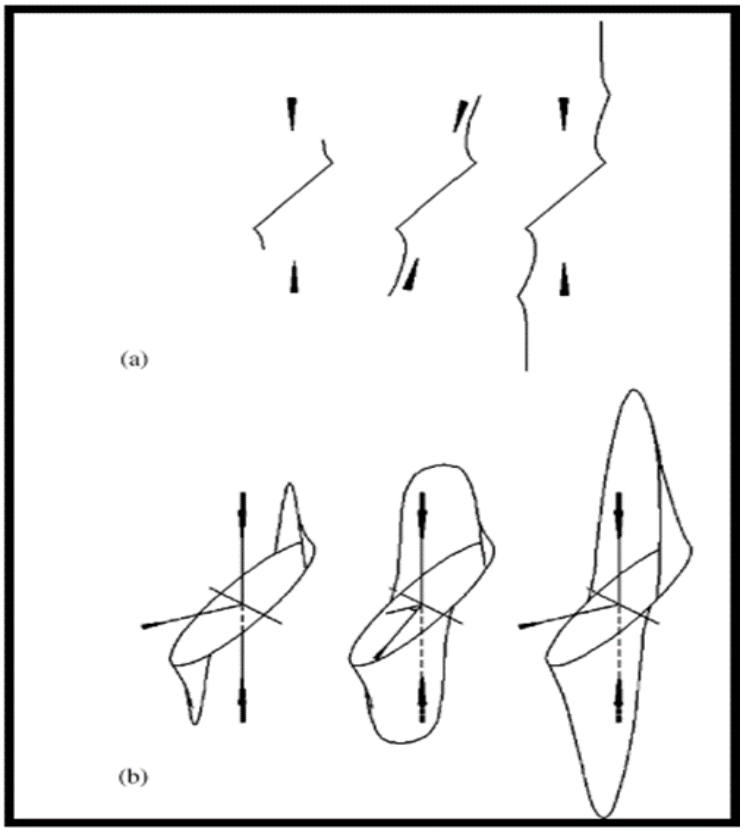


Figure 2.3.10: Crack propagation from stress rotation: (a) rotation of σ1 and σ3; (b) rotation of σ3 and σ2 (Diederichs et al, 2004)

Sahouryeh et al (2002) conducted a study on crack growth under biaxial compression, where loading is characterised by the presence of a free surface and a secondary loading perpendicular to the principal loading direction. This type of loading occurs mainly at the walls of the tunnels, where failure takes place by splitting parallel to the free face. Various researchers have investigated failure under biaxial loading. Kupfer et al (1969) studied the failure of concrete samples in both uniaxial and biaxial compression using various stress ratios in both types of loading, and several micro-cracks parallel to the applied load were observed. Tayler et al (1972) conducted a study on path dependent biaxial compressive testing of an all-lightweight aggregate

concrete. There was evidence of specimens splitting into thin slabs parallel to the loaded direction (σ_1- σ_2 plane). Brown (1974) conducted a study on fracture of rock (marble samples) under biaxial compression, whereby, vertical fracture planes were formed parallel to the direction of loading. Similarly, there was evidence of the specimens splitting into slabs parallel to the σ_1-σ_2 plane as well.

Having explained the relationship between stresses (orientations and distributions around the excavations), and the fracture genesis, it is worth exploring the criteria formulated to predict the behaviour of rocks (taking cognisance of their mechanical properties), when subjected to loading. The following sections explain these criteria.

2.4 **Prediction of Fractures**

According to Wesseloo and Stacey (2016), the complex behaviours of rocks and rock masses have presented a serious challenge to the rock engineers, for a very long time, one of which is rock fracturing. Therefore, appreciation of this mechanism of rock fracturing and failure is crucial for prediction of failure around excavations and for design of rock support to prevent instability. In addition to this, Hoek and Martin (2014) have highlighted that in order to comprehend the rock and rock mass genesis, their behaviour, such as the strength and deformation must be established. From these conditions, criteria for predicting fracturing and failure were borne, that is: Mohr and Griffith, extension strain criteria, etc.

2.4.1 Mohr and Griffith criteria

Bieniawski (1967a) explained the concept of fracture initiation from existing cracks, by making use of an hypothesis called the Griffith

criterion to predict fracture initiation. This criterion considers the stress field near the tip of pre-existing cracks and the energy balance for these cracks. This stress field is believed to cause a large tensile stress concentration at the tip of these cracks. The relationship between the applied stress field and the tensile stress at the crack tip was determined, predicting that a fracture would form when the tensile stress, near the tip of the crack, reached a particular critical value. The Griffith analysis presented shortcomings, in terms of considering only the open crack propagation, but not taking closure of cracks into account as well, when the stress field is compressive.

The Griffith criterion was modified, (Bieniawski 1967a) which then considered a compression element. A series of experiments were conducted in this regard, and another hypothesis called Mohr criterion was introduced, which was then used to determine the internal crack coefficient of friction of the material. It was concluded that this criterion was suitable to predict strength failure.

Hoek and Martin (2014) performed a study on fracture initiation and propagation in intact rock using the Griffith tensile theory and the following were their conclusions:

- The Griffith theory provides a prediction of tensile failure in brittle rocks, which is controlled by the tensile strength of intact rock or its constituent grains.
- The development of tensile cracks at or close to the tip of a Griffith crack is dictated by the orientation of the Griffith crack in relation to the applied stresses. Hence, fracture will start at or near the tip of the most unfavourably oriented crack.
- The failure process, to a large extent, is sensitive to the extent of confinement and failure diminishes rapidly as the minor principal stress increases.

- Under confinement of rock material, the equations below encompass the closed Griffith crack model, where the initiation and propagation of the tensile failure is governed by shear strength of the grain boundaries.

$$\tau = \tau_0 + \sigma \tan \phi \quad \text{.....(3)}$$

$$\sigma_1 = \sigma_3 + \sqrt{\frac{\mu}{k}\frac{\sigma_c}{\sigma_t}\sigma_c\sigma_3 + \sigma_c^2} \quad \text{.....(4)}$$

Where

ϕ = the angle of friction

τ_0 = the shear strength at zero normal stress

μ= the coefficient of friction

k= coefficient for mixed mode fracture.

Stacey (1981) stated that, two rock failure hypotheses were commonly used, which are Griffith and Mohr criteria, as indicated above. These criteria gained popularity, and several modifications have been developed to explain existing inconsistencies. These criteria are concerned with the concept of stress, but according to Handin et al (1967), there is no acceptable criterion in terms of stress only for microscopic fracture in a brittle state, hence they are regarded inadequate. As far as the study of fracture in tunnel boring of brittle rock is concerned, it was found (Stacey and De Jongh, 1977) that both Mohr and Griffith criteria suggested that the stress levels were too low to initiate fracturing. In fact, fractures did occur in the sidewall and ahead of the face, with orientations different from those predicted by the Mohr criterion (Stacey, 1981).

2.4.2 Extension strain criterion

An extension strain criterion was introduced to predict the extent of fracturing, which states that fracture of the rock will take place in indirect tension when the properties of the rock are such that the tensile strain exceeds the limiting value (Stacey, 1981). This criterion has yielded similar results with other theories, such as Brown and Trollope (1967), and the level of confidence, in terms of its application, increased as a result of the work of Kirsten and Klokow (1979) and Waldeck (1979). As far as prediction of fracturing is concerned, laboratory tests were conducted to validate the outcomes, i.e. unconfined and confined triaxial compressive tests, on a variety of rock samples to detect the point at which extension fractures would initiate in the rock. The results of these experiments were concluded as follows: *"Fracture of brittle rock will initiate when the total extension strain in the rock exceeds a critical value which is characteristic of that rock type"* (Stacey, 1981).

The extension strain criterion is very straightforward to use for prediction of fracture initiation, particularly for brittle rock with linear deformation behaviour, since theoretical elastic stress analyses can be employed. The equations 5-7 summarize the application of this criterion (Stacey, 1981):

$\varepsilon_3 \geq \varepsilon_c$,.....(5)

Where ε_c is the critical value of extension strain and

ε_3 is a minor principal strain.

$\varepsilon_3 = \frac{1}{E}[\sigma_3 - \nu(\sigma_1 + \sigma_2)]$.....(6)

Where σ_1, σ_2 and σ_3 are the principal stresses, E is the elastic modulus and ν is Poisson's ratio.

The critical value of extension strain can be obtained from the tests signifying the strain at which extension fractures are initiated. Stacey (1981) determined the critical values of extension strain for various rock types based on laboratory tests as summarized in Table 2.4.1. According to Wesseloo (2000), the critical extension strain can be estimated by making use of the following equation:

$$e_c = \frac{f*UCS*\nu}{E} \quad \text{.....(7)}$$

Where:

e_c = critical extension strain;

UCS = uniaxial compression strength of intact rock sample of the rock;

ν = Poisson's ratio;

E = Young's modulus

f = factor that varies between 0.25 to 0.3 for crack initiation strain and 0.7 to 0.8 for failure strain or crack damage.

Table 2.4.1: Critical values of extension strain (Stacey, 1981)

Rock Type	Specimen lentgh/ diameter	Critical extension strain
Quartzite A	2	0.000120
Quartzite B	2	0.000109
Quartzite C	2	0.000081
Quartzite D	2	0.000107
Quartzite E	2	0.000130
Lava A	2	0.000152
Lava B	2	0.000138
Diabase	2	0.000175
Norite	2.5	0.000173
Conglomerate A	2	0.000086
Conglomerate B	2	0.000073
Conglomerate C	2	0.000083
Sandstone	2	0.000090
Shale A	2	0.000116
Shale B	2	0.000150
Shale C	2	0.000095

2.5 Conclusion

From the literature reviewed, it is clear that, from a planning perspective, in situ stress is an important parameter in modelling of excavations. If invalid assumptions are made, this could compromise the excavation stability and its safety. Creation of excavations causes a substantial redistribution of the stress field, which could potentially exceed the host rock strength, leading to fractures forming in the surrounding rock. The extent of fracturing depends on the ratio and magnitudes of principal stresses. If these ratios and magnitudes are sufficient, rock mass failure occurs in the form of spalling, buckling, and strain bursting.

The extent of fracturing is successfully predicted by using an extension strain criterion. The following chapter illustrates application of this criterion, in terms of its successful use in predicting extension fractures.

CHAPTER 3

APPLICATION OF EXTENSION STRAIN CRITERION

3.1 Introduction

Stacey (1982) used extension strain criterion to explain the mechanism of core discing (the breaking up of rock core spontaneously into discs), which takes place during diamond drilling practice in highly stressed areas. Various authors have investigated this phenomenon, whereby numerous field and laboratory tests were done and a conclusion was that, the failure was initiated on the exterior surface of the core. These authors proposed that discing was initiated as a result of shear stress. This disagreed with other previous authors whose observations suggested clean unsheared surfaces. In contrast, Stacey (1982) suggested that the end of the borehole in stressed rock is a location of biaxial or triaxial compressive stress; hence, extension fractures can be initiated. This mechanism of core discing can be analysed by the simple criterion of extension strain fracture.

The following sections highlight the validations of the extension strain criterion, when used to predict fracture initiation.

3.2 Uses of Extension Strain Criterion

There have been criticisms concerning the usage of extension strain criterion, mainly because of the misconception about its interpretation and application. However, Wesseloo and Stacey (2016) reported studies, which were conducted under laboratory, in situ and numerical analyses, which highlighted the successful usage of the extension

strain criterion. These studies included, work by, Pang and Goldsmith (1990), Simmons and Simpson (2007), Ndlovu (2006), Ndlovu and Stacey (2007) and Li et al. (2013).

3.2.1 Laboratory studies

As far as these studies are concerned, Wesseloo and Stacey (2016) considered the study of Pang and Goldsmith (1990) on the development of cracks during loading, of brittle rock specimens by using an indenter in place of a jackhammer bit tips. It was discovered that the extension strain criterion predicted the orientation and the degree of fracturing in the rock samples. Moreover, Li et al. (2011) commented on the results of Brazilian disc tests, noting that the slabbing fractures parallel to the loading direction initiated at a critical extension strain. The lateral strain gauges attached on the surface of the sample indicated that the critical extension strain and maximum tensile strain are almost equal, when subjected to the Brazilian test. Further studies by Li and Wong (2013) indicated that the extension strain criterion has shown to be able to describe the crack initiation and propagation in the Brazilian test.

3.2.2 In situ studies

Simmons and Simpson (2007) explained the complexity of the failure of bedded rock slopes, which encompasses the initiation of a rock mass failure mechanism through a combination of pre-existing rock discontinuities together with stress-induced fracturing of rock material. Predictions of these complex failures were almost impossible with the existing rock mass strength models, but the extension strain fracture criterion seemed to be consistent in determining failure initiation, prior to occurrence.

The inception of guttering in a coal mine was well predicted by application of the extension strain criterion in a study conducted by Ndlovu (2006). It was apparent that other traditional criteria, such as the Mohr-Coulomb criterion, were unsuccessful in predicting the onset of guttering. In validation, a numerical study applying extension strain criterion, anticipated failure primarily in the solid, just ahead of the contact area between roof and pillar.

3.2.3 Numerical studies

Steffanizzi et al (2007) indirectly validated the extension strain criterion by conducting a numerical study on strain driven fractures around in layered media. A finite element method (FEM)/discrete element method (DEM) was applied using the ELFEN code (2006), which permits the modelling of a rock mass changing from a continuum to a discontinuum. The three-layered model geometry and the outcome of the model when fracture saturation transpired are shown in Figure 3.2.1. In order to define the fracture process a stress-strain model was simulated, which indicated uniformly distributed maximum principal stress, which cannot predict the fracture initiation point (Steffanizzi et al 2007). In contrast, the extension strain, which is not uniform, could be used to predict the fracture onset, with a critical value of 150 microstrain (με). Steffanizzi et al (2007) indicated that, as the fracture opens up, the value of the extension strain decreases, whilst increasing in the surrounding area, giving rise to new fracture formation. When this increase in extension strain is inadequate to reach to the critical value, no new fracture is formed. In conclusion, Steffanizzi et al (2007) pointed out that, fracture initiation and spacing are dictated by the extension strain location, which indicates the coherence with Stacey's strain criterion.

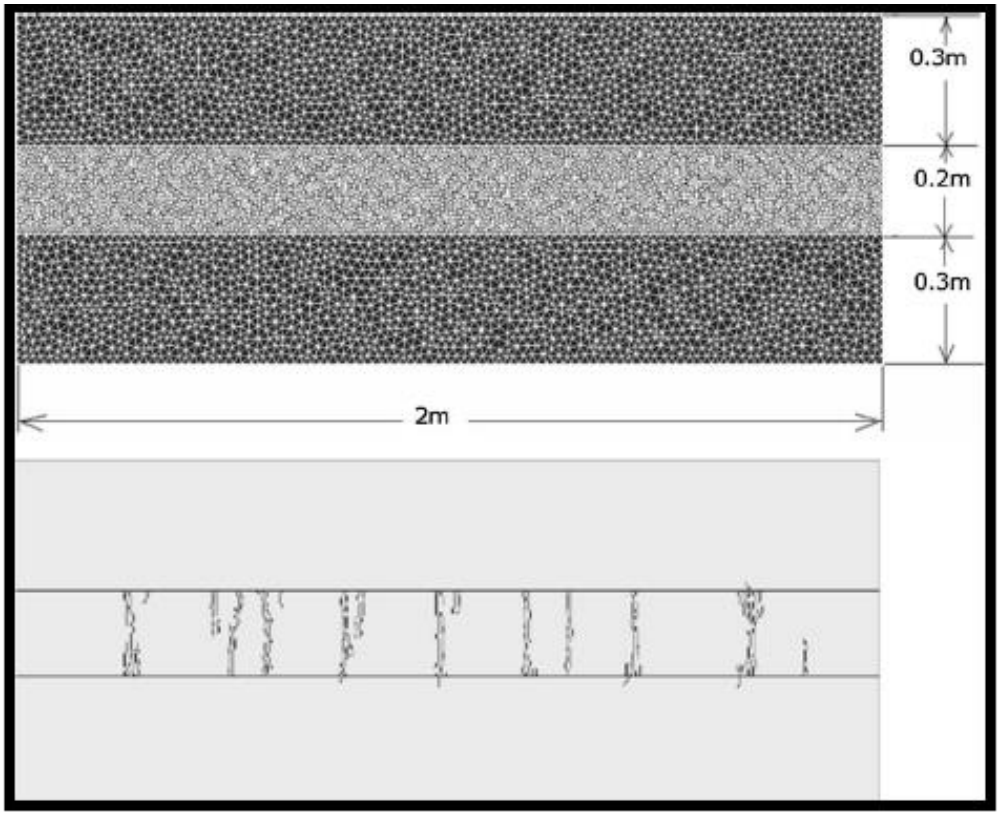


Figure 3.2.1: Prediction of fracture in layered media (Steffanizzi, et al., 2007)

A study was conducted by Barton and Shen (2017) to analyse fracturing in the Beaumont tunnel with the aid of FRACOD model. Numerical models were generated, in which two scenarios were considered. In the first scenario, the horizontal stress (σ_h) was assumed to be one third of the vertical stress (σ_v), σ_h/σ_v equal to 0.33. The results are shown in Figure 3.2.2, where failure is said to take place in both extension fracturing (shown in red) and shearing (shown in green). Similarly, in the second scenario the same failure modes were expected. In contrast, the results for σ_h/σ_v equal to 2.0 can be seen in Figure 3.2.3. It is apparent in both scenarios that fractures are propagated normal to the direction of the minor stress.

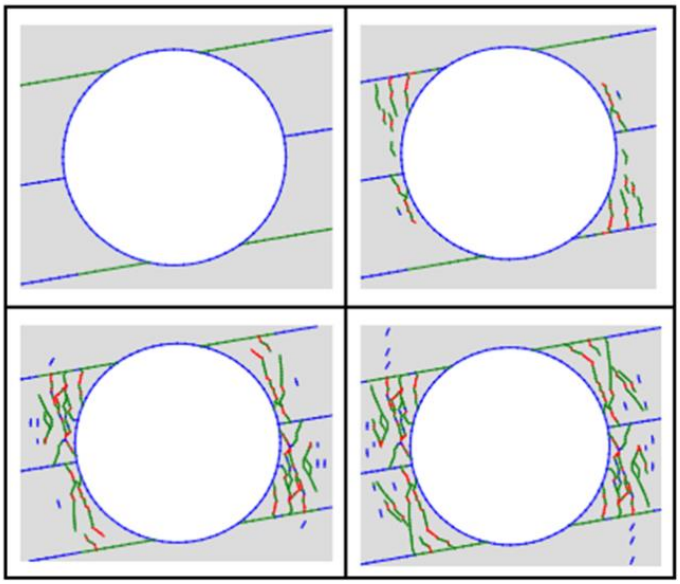


Figure 3.2.2: FRACOD models of the Beaumont tunnel fracturing for $\sigma_h/\sigma_v = 0.33$ (Barton and Shen 2017)

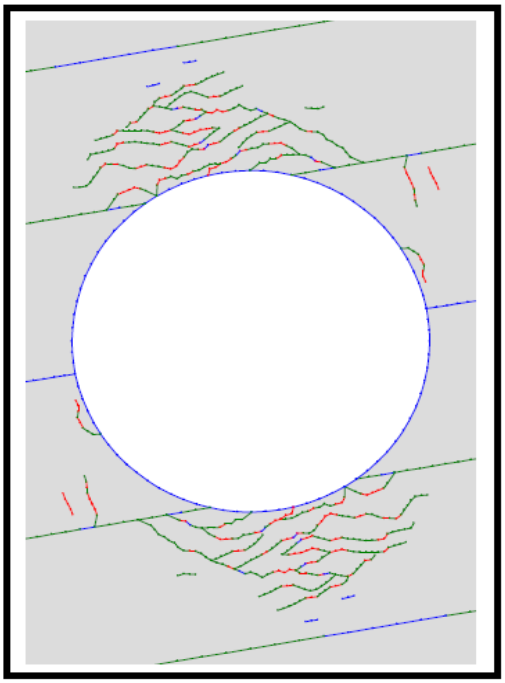


Figure 3.2.3: FRACOD models of the Beaumont tunnel fracturing for $\sigma_h/\sigma_v = 2$ (Barton and Shen 2017)

3.3 **Conclusion**

It is clear that the extension strain criterion can be used to predict fracture initiation, and failure in some instances. The laboratory studies indicated that the crack formation, when specimens are subjected to Brazilian tests, could be explained by extension strain criterion. Similarly, in situ studies indicated that extension strain criterion seemed to be consistent in determining failure initiation, beforehand. This warrants the use of this extension strain criterion, when analysing fracturing around deep level tunnel boring.

The following chapter describes the impact of extension fractures on the advancing excavations, when boring is done in fractured zones. Three case studies are discussed, to provide a practical perspective of the impact of extension fractures on excavations.

CHAPTER 4

THE IMPACT OF THE EXTENSION FRACTURES

4.1 Introduction

As already mentioned, in recent years, boring of excavations by means of machines, raise or tunnel boring, has become more popular in both mining and civil engineering. These types of bores are often undertaken under extreme conditions, e.g. high stress levels, where fracturing of the rock occurs around and ahead of the faces of excavations (Wesseloo and Stacey, 2000). The stability of these fractures depends on the magnitudes of the stresses acting and the rock mass properties. Advancing excavations in these conditions can result in major failures and low utilisation of the boring machines. The challenges presented by fracturing of the rock are dealt within the sections below.

4.2 Failure of the Excavations by Fracturing

According to Bieniawski (1967a) failure is the manner in which a material changes from one state of behaviour to another one, which defines fracture initiation concepts. Underground excavations in high stress levels or reasonably jointed brittle rock of good quality, where spalling and slabbing are the most prominent modes of failure, fail by means of cracking or fracturing (Aglawe, 1999).

Larsson (2004) indicated that when an excavation is created in rock, there is a change in energy, and the rock responds to the energy change, i.e. the following events take place; the remaining rock mass

and installed support are deformed, new fractures are created, and seismic waves are generated. According to Dyskin and Germanovich (1993), an excavated opening contains free surfaces, which present a high concentration of compressive stresses, where pre-existing cracks are propagated, parallel to these surfaces. As a result, interaction of these cracks and free surfaces increases their growth and instability. Eventually these cracks coalesce, and spall or buckle or even fail dynamically in the form of strain bursting.

Ortlepp and Stacey (1994) identified the source mechanisms, which define the nature of failure of the rock, depending on the magnitude of energy released. The two most prominent mechanisms, for the sake of this research, are given below.

a) Strain bursting

Strain bursting is a violent expulsion of rock fragments in the form of slabs with sharp edges. The nature of the surfaces of these fragments normally shows extensional fracturing. The orientation of the in-situ stresses and the shape of the excavation determine the location where this ejection would take place. There are some significant conclusions that have been drawn concerning strain bursting:

- Strain bursts are more prone to take place in massive rocks than in jointed and fractured rock masses;
- They occur commonly in machine bored excavations; and
- They are usually associated with high stress levels.

Apart from occurring in massive rocks, machine bored excavations and in high stress levels, Stacey (2016) indicated that the probability of occurrence of the strain busting also depends on:

- The rock mass strength and deformation properties, for instance rocks which are stiff, with high deformation modulus, are more susceptible to violent failure; and
- The geometry and size of the excavation.

According to Jager and Ryder (1999) strain bursts are initiated by minor deviations in the stress field, which cause the strength of the highly stressed rock mass to be exceeded, and subsequently, due to the stored strain energy in the rock mass, rock is ejected. This change in stress can be brought about by the momentary stress related to a remote seismic event, an advancing excavation face, or over time.

Larsson (2004) explained strain bursting as one of the most well-known forms of rock burst in mining and civil engineering excavations, and as a violent occurrence where slabs of rock are ejected from the surfaces of an excavation. The potential for its occurrence depends on the magnitude of the energy to be released, which is based on the law of conservation of energy. Opening an excavation in a rock causes change in potential energy (W_t), and the removed rock contains stored energy (U_m), where the sum of the two energies represents the total energy that must be released. As already mentioned, the process of removing rock results in stress redistribution, thus subsequently the stored strain energy (U_c) increases. Furthermore, if there are support units installed, some of the energy (W_s) would be absorbed. The resultant energy is called released energy (W_r), and from the law of the conservation of energy, the following formula can be written:

$$W_t + U_m = U_c + W_s + W_r \quad \text{.....(8)}$$

Larsson (2004) further indicated that if there is prompt removal of the rock, there would be oscillation in the rock mass, and damping would take place to restore equilibrium, and in the process, seismic energy or

kinetic energy (W_k) would be released. This can be represented by the following formula:

$W_r = U_m + W_k$ .....(9)

Therefore, the energy which is responsible for bursting is:

$W_k = W_t – (U_c + W_s)$ .....(10)

b) Buckling

Buckling is a failure mode that occurs as a result of the strain energy stored in the "plates" or slabs, being released. It can also be initiated by the shear and compressive elements of a seismic wave originating further away, relative to the buckling position (Ortlepp and Stacey, 1994). According to Kazakidis (2002), buckling failure is initiated as a result of a highly stressed (compressive) and jointed rock mass, where plates or slabs are formed as planes parallel to the excavation surfaces.

Having explained what buckling is, the studies below will try to bring different perspectives from various authors, on analyses of buckling mechanisms, in terms of required load, slab flexure or deflection etc.

When analysing the buckling mechanism Kazakidis (2002) used Euler's formula to determine the critical load (σ_b) that is required to initiate buckling, and hence the stress under which the plate will buckle i.e.

$$\sigma_b = \frac{Pcr}{A} = \pi^2 \frac{EI}{A\iota^2} = \pi^2 \frac{E}{12(\iota/t)^2} \quad \text{.....(11)}$$

Where:

P_{cr}: the critical load;

E: Young's Modulus;

l: the length of the slab;

t: the thickness of the slab;

w: the width of the slab;

A: the cross section under loading (A = wt)

l/t: the slenderness ratio of the slab;

I: the moment of inertia, ($I = wt^3/12$, for rectangular cross sections)

From the relationship between ratio of the length to thickness of the slab (which is called slenderness ratio) and the required stress, it is apparent that the smaller the ratio the larger the stress is required to buckle the slabs, as shown in Figure 4.2.1.

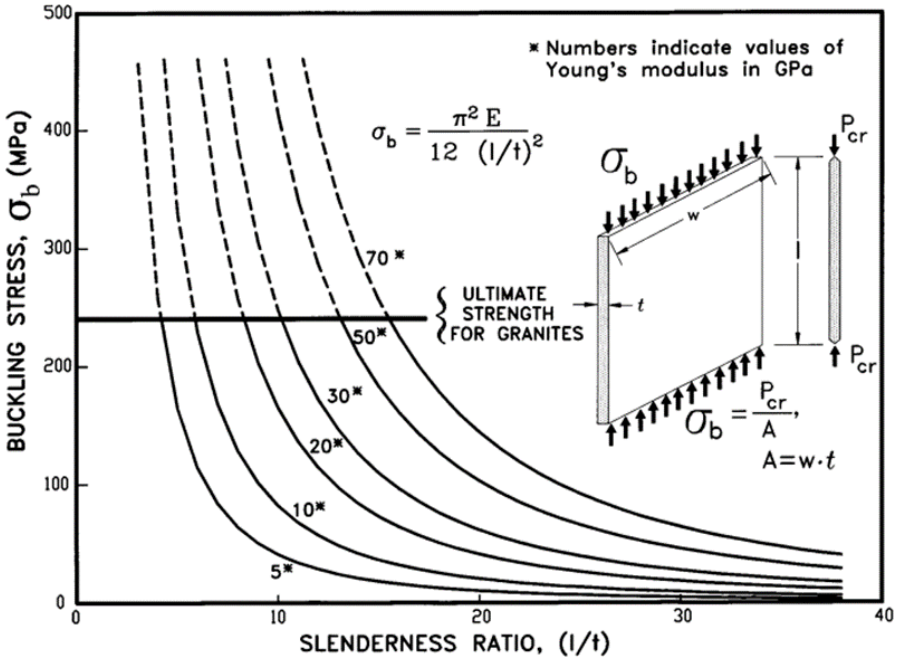


Figure 4.2.1: Buckling stress versus slenderness ratio for buckling failure using Euler's formula (Kazakidis, 2002) and (Iannacchione, et al., 1998)

Krenzke and Charles (1963) studied a theory of classical small-deflection for the elastic buckling of a complete sphere, which was analysed by Timoshenko (1936), where it was assumed that buckling would occur at the pressure, which allows an equilibrium shape, which is thoroughly removed from the perfectly spherical deflected shape. The overall expression for this classical buckling pressure (P_{CR}) was given as:

$$P_{CR} = \frac{KE\left(h/R\right)^2}{\sqrt{1-v^2}} \quad \text{.....(12)}$$

Where:

K is a buckling coefficient,

E is Elastic modulus,

h is the shell thickness,

R is the radius to the mid-surface of the shell, and

v is Poisson's ratio.

According to the outcome by Krenzke and Charles (1963) on glass spheres, the K value was almost 0.84, and that the elastic buckling strength of initial imperfect spherical shells is dependent on the local curvature and the thickness of a segment of the critical arc length (L_c). The critical length can be calculated by the formula below for v of 0.3 and is illustrated by Figure 4.2.2.

$$L_c = 2.42h(m_i)^{1/2} \quad \text{.....(13)}$$

Where:

m_i is the ratio of modified radius and thickness (R_i/h).

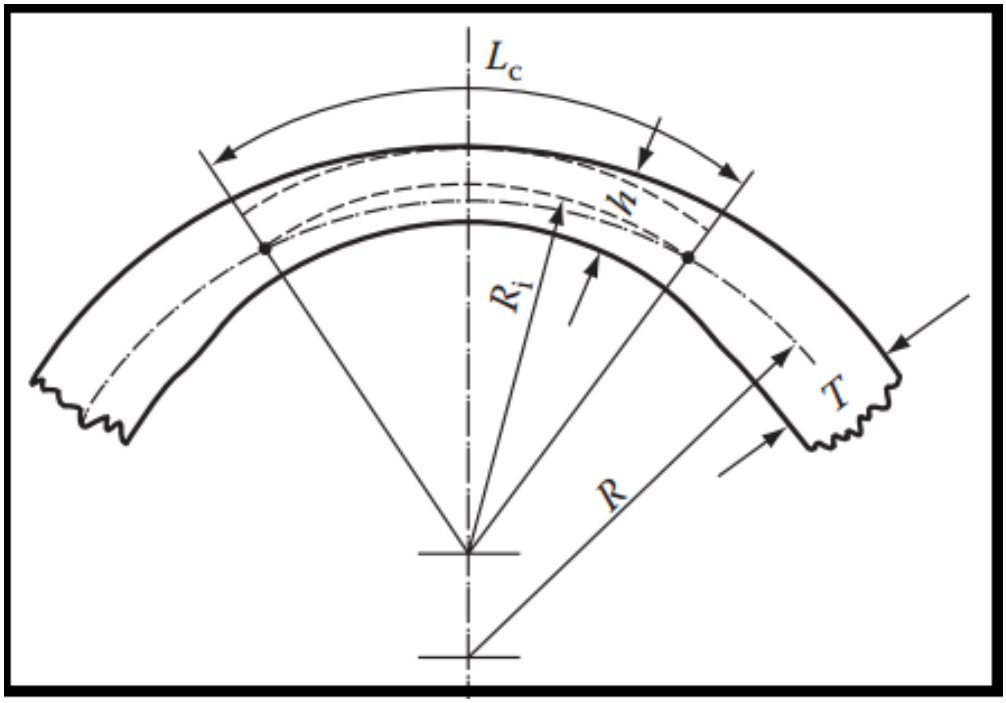


Figure 4.2.2: Notation for defining a local change in wall thickness (Krenzke and Charles, 1963).

According to Huston and Josephs (2008), a study was carried out in which the effect of clamped edges on the response of a hemispherical shell was evaluated. The relevant buckling pressure was found to be about 20% lower than that for a complete spherical shell having the same value of the parameter *m* and the elastic modulus E. These investigations could be of certain interest to designers dealing with complete spherical vessels as well as domed-end arrangements. From a practical point of view, the most acceptable method of predicting the collapse pressure would be to use a plot of experimental data as a function of experimental collapse pressure (Pe), Pressure to cause membrane yield stress (Pm), and Classical linear buckling pressure (P_{CR}).

McGarr (1997) analysed other authors' experimental results (Brace and Bombolakis, 1963 and Fairhurst and Cook, 1966), and deduced that when a rock sample is subjected to uniaxial compression and the axial stress reaches uniaxial compressing strength, axial cracks are formed. Subsequently, these cracks extend and join up, resulting in splitting failure. He further made an assumption that maximum stress (σ) in the excavation sidewall is satisfactorily close to the value of uniaxial compressive strength (S), resulting in generation of various cracks parallel to the free surface. Figure 4.2.3 was used to illustrate this concept, where these cracks link up, and forming slabs: an excavation of dimension L undergoes loading, forming slabs of thickness h as illustrated in Figure 4.2.3 and Figure 4.2.4.

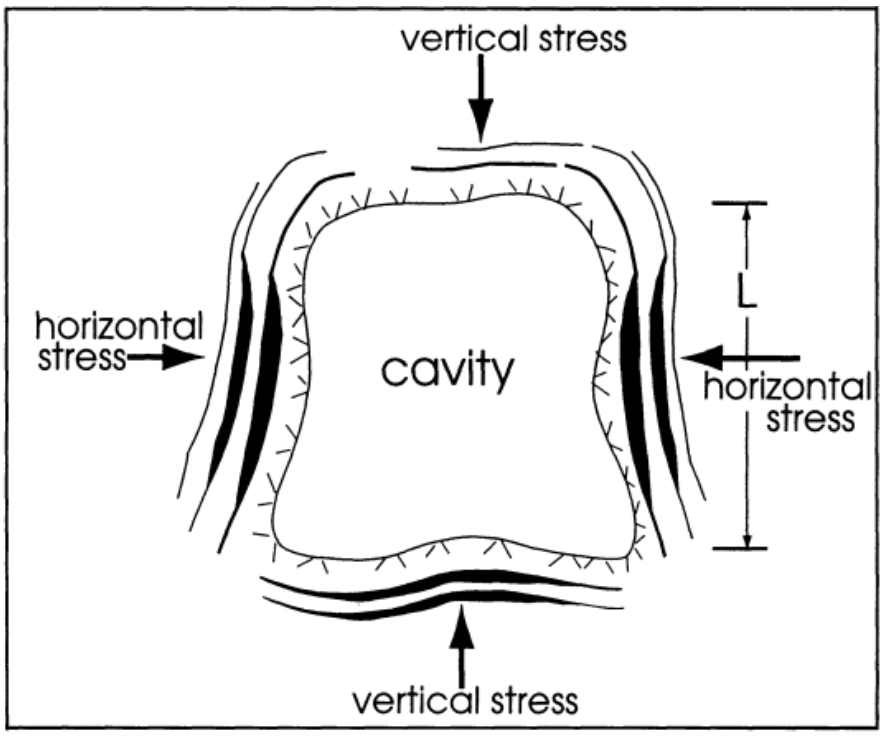


Figure 4.2.3: Development of Slabs around underground openings (McGarr, 1997)

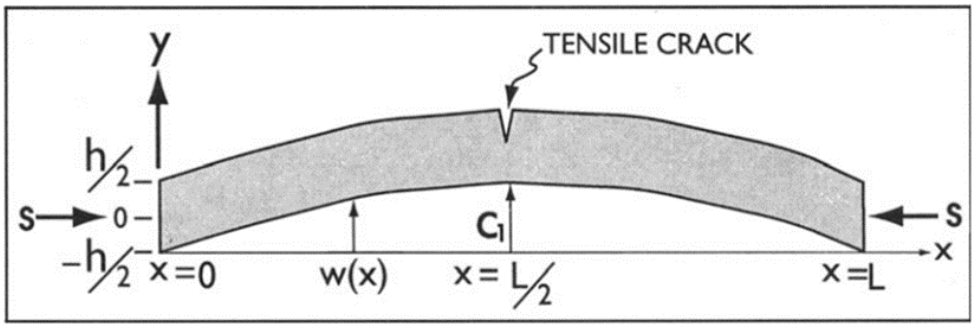


Figure 4.2.4: The outline of the slab with thickness (h) and dimension (L) and applied stress (S) (McGarr, 1997).

The slab thickness can be calculated as follows, provided the sidewall dimension or plate/slab length (L) together with the applied load σ, which is similar to S, in this case, (McGarr, 1997), are known:

$$\frac{h}{L} = \frac{2\sqrt{3}\sqrt{1-\upsilon^2}}{\pi}\sqrt{\frac{\sigma}{E}} \quad \text{.....(14)}$$

Where:

v = Poisson's ratio;

E = Young's modulus

It is worth noting, from Figure 4.2.4, that it is crucial to determine the value of the amplitude of flexure (c_1), which determines the point where an extensional strain exceeds the compressive strain associated with the applied load (σ). This serves as a point when the tensile crack would propagate, breaking the slab into two parts. Therefore:

$$c_1 = \left(2/h\right)\left(\frac{L}{\pi}\right)^2\left(\frac{1-\nu^2}{E}\right)S \quad \text{.....(15)}$$

The deflection point (w), at point of buckling, can be determined by:

$$w = c1sin\frac{\pi x}{L} \quad \text{.....(16)}$$

The ejection velocity can also be estimated, which would assist in predicting the possible violent damage to underground excavations, with the aid of equation 17.

$$v = \frac{S}{\sqrt{\rho E}}\left[3 + \frac{1-\nu^2}{2}\right]^{1/2} \quad \text{.....(17)}$$

Where: ρ = rock density.

Wall-rock velocity (peak particle velocity (PPV) or peak ground velocity, (PGV)), is regarded as one of the most significant parameters that describe the extent of ground motion due to its link with rock burst damage (Qiu, et al., 2014). Moreover, PPV has been incorporated in many support design criteria for the use in ground, which is subjected to bursting. Qiu et al (2014) devised a methodology to estimate the wall-rock velocity during rock bursting.

Six true-triaxial tests were conducted to demonstrate the formation of the extension fractures and slabs. The tests were set up in such a way that the minimum principal stress (σ3) was gradually reduced to simulate the decrease of radial stress during the excavation process. The maximum principal stress (σ1) was increased to demonstrate the intensity of the tangential stress in the excavation area. The intermediate principal stress (σ2) was kept unchanged for the period of the experiment. The results of the tests are shown Figure 4.2.5, where the extension fractures and rock slabs are indicated and their orientation is parallel to the direction of σ1 and σ2 and normal to σ3, together with testing stress path.

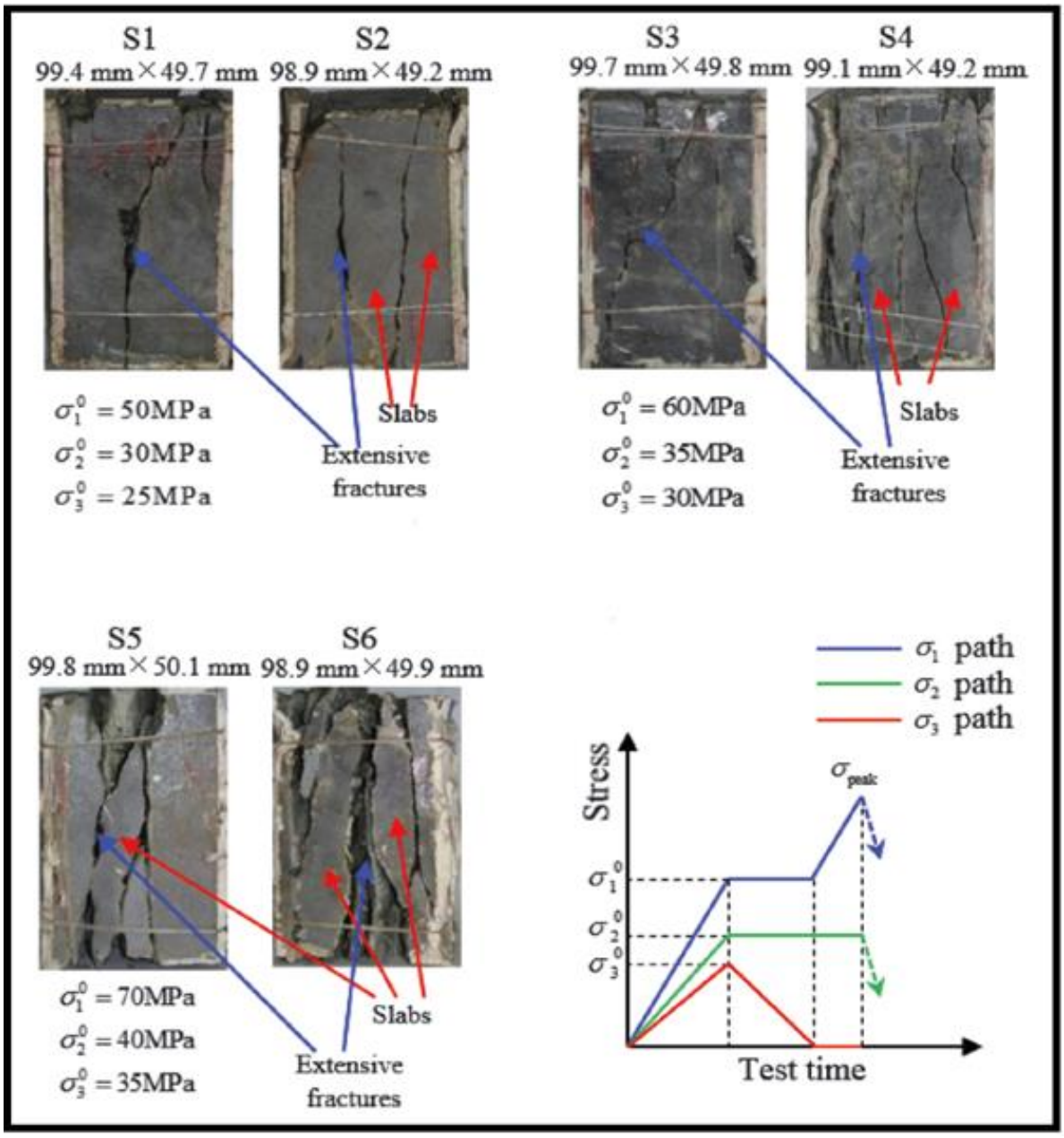


Figure 4.2.5: True triaxial loading-unloading tests showing the formation of extension fractures and slabs (Qiu, et al., 2014).

Qiu et al (2014) have summarised these mechanisms with the aid of Figure 4.2.6 to illustrate the process of rock bursting caused by slab buckling, in three stages. In (a), many extension fractures are formed in the critical zone of the excavation due to high stress concentration, reducing further away from the excavation surface. In (b), as the stress

levels increase, the extension fractures link up, forming long fractures, eventually forming large slabs or plates adjacent to the excavation surface. And in (c), a further increase in loading causes bending of the slabs, in the process storing large amounts energy. Subsequently, the stored energy is converted into kinetic energy, which results in failure by buckling and rock bursting.

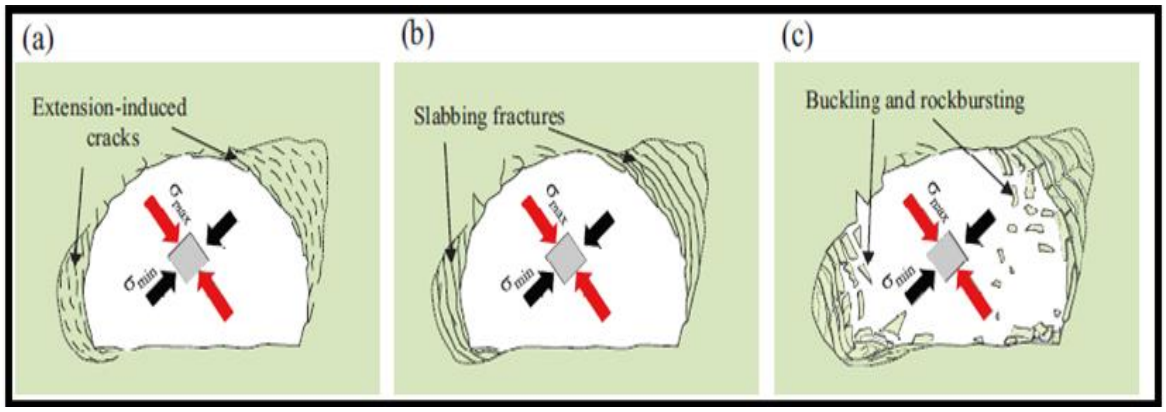


Figure 4.2.6: The development of slabbing, buckling and rock bursting (Qiu et al, 2014)

When assessing the buckling mechanism, Qiu et al (2014), used a method suggested by Bazant et al. (1993), based on the strain energy release, to investigate the size effects in a borehole breakout, in assessing the slab thickness. A basic tunnel fracturing model is proposed, as shown in Figure 4.2.7; which shows a tunnel being excavated, leading to the formation of several cracks (which are parallel to the tunnel surface), eventually forming rock slabs, with the average thickness (t) in the cracking zone of the excavations.

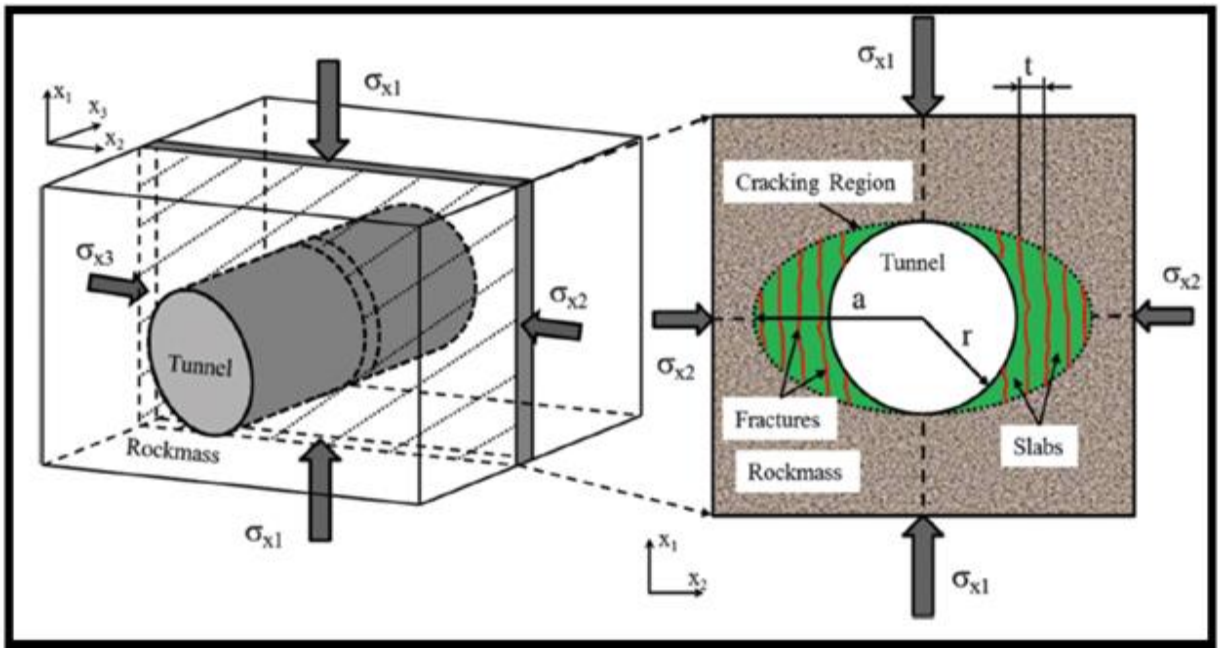


Figure 4.2.7: An elliptical model showing fracturing zone and rock slabs that occurred near the deep level tunnels (Qiu, et al., 2014)

.

From Figure 4.2.7, in a circular cylindrical tunnel of radius (r), under loading conditions of compressive stresses σ_{x1} and σ_{x2} in the x1 and x2 planes, the slab thickness can be estimated by equation 19:

$$\sigma_{cr} = -\frac{\pi^2 E' t^2}{12L^2} + \frac{t}{\lambda} G \quad \text{.....(18)}$$

Where:

$E' = E/(1-v^2)$

E = Young's modulus of the rock

v = Poisson's ratio

t = Slab thickness

L= effective half length of the slabbing fractures at the moment of failure

G = elastic shear modulus of the rock mass

λ = the material property representing the thickness of an intact rock layer

σ_{cr}= Limit load therefore is calculated by equation 18:

$$t = \left(\frac{0.1453\text{UTS}}{\sqrt{5k_s}}\right)^{2/3} \quad \text{.....(19)}$$

Where:

UTS= Uniaxial tensile strength of the rock

k_s = shear stiffness of the tensile fracture and

$k_s = \tau_{peak}/\delta_{peak}$

Where:

τ_{peak} = peak shear strength

δ_{peak} = peak shear displacement

$$\delta_{peak} = 0.0077\left[L^{0.45}\left(\frac{\sigma_n}{JCS}\right)^{0.34}\right]\cos\left[JRC\log_{10}\frac{JCS}{\sigma_n}\right] \quad \text{.....(20)}$$

$$\tau_{peak} = \sigma_n\left[JRC\log_{10}\left(\frac{JCS}{\sigma_n}\right) + \phi_r\right] \quad \text{.....(21)}$$

Where:

σ_n = the normal stress across the fracture

ϕ_r = the residual friction angle

JRC = the joint roughness coefficient

JCS = the joint wall compressive strength

L = is the length of the joint sample (in metres)

Qiu et al (2014) provided the parameters in Table 4.2.1 for tunnels at depths of 3250 m in a South Africa context, which were used to calculate the possible slab thicknesses:

Table 4.2.1: Rock material parameters Qiu et al (2014)

Parameter	
UTS (MPa)	27
JRC	6
JCS (MPa)	325 (UCS)
L (m)	3
σ_n (MPa)	0.1
ϕ_r (°)	35

Barton and Choubey (1976) conducted a study on the shear strength of rock joints, and developed an empirical law for predicting their shear strength. Three index parameters; the joint roughness coefficient (JRC), the joint wall compressive strength (JCS), and the residual friction angle ϕr (ϕ_r is equal to the base friction angle ϕ_b, for unweathered fracture surfaces) were included in the empirical equation, i.e.

$$\tau = \sigma_n \tan\left(JRC \log 10\left(\frac{JCS}{\sigma_n}\right) + \phi_b\right) \quad \text{.....(22)}$$

According to Gumede (2006), for a fresh unweathered joint, the JCS value is equal to the unconfined compression strength (σc) of the rock. Furthermore, the value of JCS decreases with increase in state of weathering and values for the friction angle were determined from the Tilt Test, which are: JRC = 20; JCS = (σc); for a fresh unweathered joint surface (ϕb) = (ϕr) for a fresh unweathered joint surface with basic angle between 28.5° and 31.5°.

- Wall-rock velocity analysis

Wall-rock velocity is calculated by assuming that immediately after the slab has buckled, forming a fracture at the middle of the slab, then the two halves of the slab can move freely, and in the process, the stored elastic energy is converted into kinetic energy **(**Qiu et al 2014**).**

Therefore: $v = \sqrt{\frac{3}{\rho E}}\sigma_{cr}$.....(23)

Where:

ρ= Rock density

v = Peak velocity

σ_{cr}= Limit load

E = Young's modulus of the rock

4.3 **Effects of Fracturing on Boring Machines**

TBM tunnelling is a distinct excavation method, which is dependent on the interaction between machine and the rock mass (Gong et al., 2012). The mechanism of boring involves little disturbance of the surrounding rock mass. As a result, there may be a higher probability of rock bursting due to lower release of strain energy during TBM tunnelling.

It is clear that, in high stress conditions, TBM tunnelling is prone to rock slabbing and bursting, which warrants a comprehensive study, in order to avoid unnecessary delays or additional boring costs. This is apparent in the studies done by Gong et al (2012), which involved the influences of slabbing and rock bursts on TBM's, based on the rock behaviour in the Jinping-II headrace tunnel. It was discovered that rock bursts influence the TBM penetration and advance rates, and have effects on:

- The Rock fracturing process by TBM cutters;
- The tunnel support;
- The cutter wear and cutter head failure;
- Broken rock removal; and
- Grippers

Stacey (1989) conducted a study on boring of tunnels and shafts in massive rock to investigate the frequent rock fracture problems. It was apparent that, regardless of several tunnels being bored successfully in the past, there were still challenges in boring operations. A number of failures in both tunnel and shaft boring operations, as a result of fracturing of the rock induced by the high stress level, were recorded. Similar issues of fracturing, which resulted in failure, were discussed by Graham (1976), Sperry and Heuer (1972), Stacey and De Jongh (1977), Taylor et al., (1978), Burgess and Taylor (1980) and Grimstad (1986). These issues include:

a) Spalling/slabbing of the rock from the sidewalls leading to machine grippers not reaching the sidewall, resulting in an unusual cutter wear;
b) Rock fracturing on the tunnel face, releasing relatively large chunks of rock which result in TBM head jamming, damaging the front transfer chute and the conveyor belt;

c) Dog earing in deep level raise boring, causing high machine vibration and irregular high torque demand. This has resulted in failures that have caused the cutter head to fall to the bottom of the bore; and
d) Rock bursting from the surface of the tunnel, resulting in boring operations being suspended, which translated into high tunnelling costs.

Stacey and Thompson (1991) examined a case of a "large stress induced borehole breakout" in a diamond mine tunnel driven by a road-header. It was done to indicate the breakout formation, close to the excavation face, which was promoted by the presence of extension fractures. It was discovered that, in spite of relatively low field stresses and rock strength, and the non-brittle nature of the kimberlite rock, there was still evidence of strain bursting due to machine utilisation in excavating the tunnels. Furthermore, the surfaces delineating the breakout fragments appeared to be extensional surfaces, that is, the surfaces were clean and did not indicate any crushed material that would indicate shear failure. The effect of these failures has a negative impact on the cutting or boring process, which means that it has to be undertaken on a stop-start basis, to allow support installation to take place to contain the rock failure.

Diederichs (2007) pointed out that spalling and strain bursting have, for a long time, been regarded as mechanisms of failure in deep underground mines in hard rock and infrastructure tunnels, driven mostly by TBM's. He is of the opinion that slabbing and spalling of tunnel walls are tension failure processes under high stress. The sequence of events, which ultimately leads to failure by means of strain bursting, involves spalling (the development of noticeable extension fractures), under compression loading. This leads to instability as parallel and thin slabs/plates (formed as a result of coalescing of

extension fractures) buckle. Subsequently, the buckling mechanism provides a sudden release of energy, causing strain bursting. The utilisation of TBMs is affected, due to substantial wall spalling in front of the grippers, causing delays to the boring operation. Figure 4.3.1 demonstrates these spalling mechanisms.

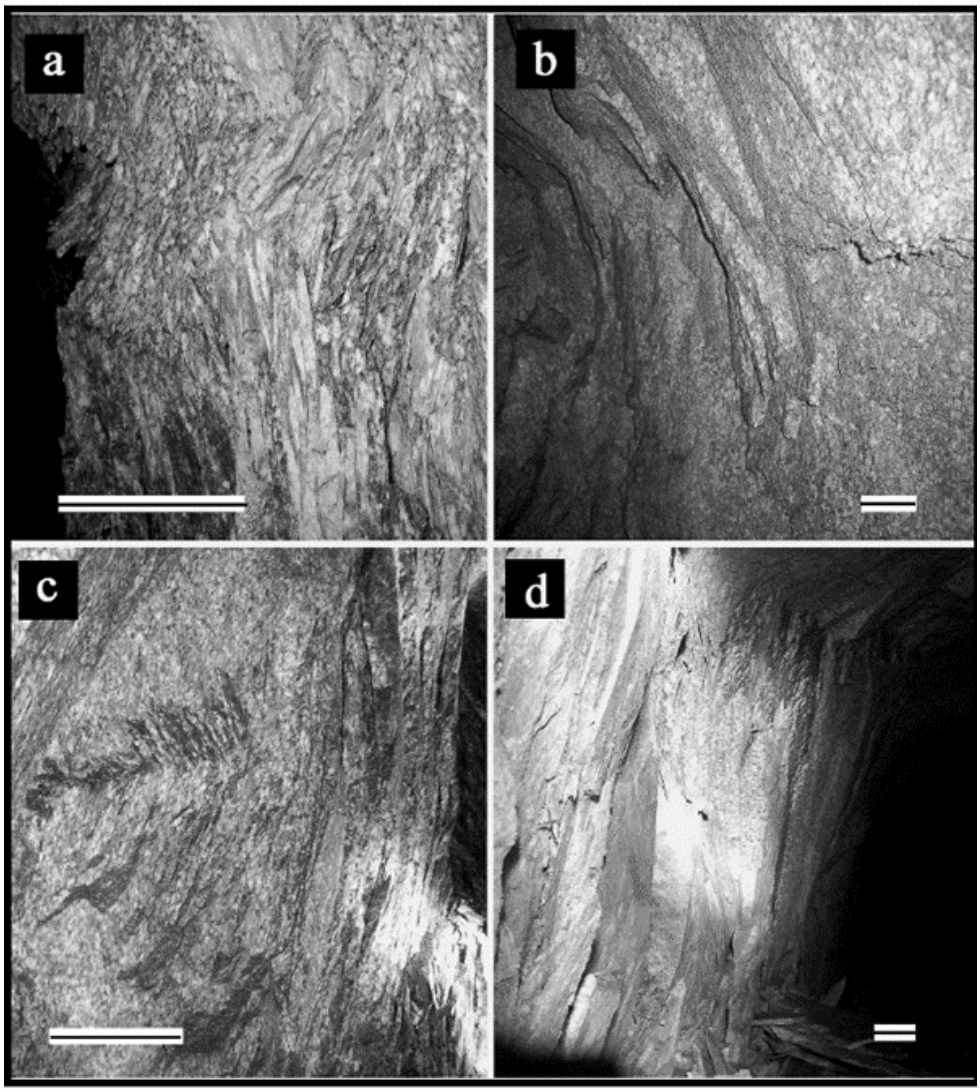


Figure 4.3.1: Examples of spalling resulting from crack growth (Diederichs, 2007).

4.4 **Case Studies**

4.4.1. Introduction

The case studies were chosen, based on the relevance of the topics related to this research, such as impact of the in situ stress field and stress redistribution on boring operations, and the rock fracture network that leads to failure of tunnels (spalling, buckling, strain bursting):

- In situ monitoring of rock-burst nucleation and evolution in the deeply buried tunnels of Jinping II hydropower station (Li et al, 2012);
- Rock burst and slabbing failure and its influence on TBM excavation at headrace tunnels in Jinping II hydropower station (Gong et al, 2012); and
- Engineering Geology of Alpine Tunnels: Past, Present and Future (Loew et al, 2010)

4.4.2. In situ monitoring of rock-burst nucleation and evolution in the deeply buried tunnels of Jinping II hydropower station (Li et al, 2012)

This section contains a brief description of the case study described by Li et al (2012).

The Jinping II hydropower station is located at the eastern hills of the Qinghai–Tibet Plateau in an area influenced by the collision of the Eurasian plate and the Indian Ocean plate. The principal strata cropping out at the construction site are carbonate rocks. Small amounts of green sandstone, chlorite and sandy slate are found near the entrance of each tunnel. The uniaxial compressive strength (UCS)

of this marble ranges from 80 to 120 MPa and its Young's modulus (E) is about 25–40 GPa. There are seven parallel high pressure tunnels with maximum overburden up to 2525 m, mostly excavated in marble (Wu et al, 2010, Zhang et al, 2011a). The two auxiliary tunnels were completed, while one water drainage tunnel and the other four headrace tunnels with diameters of 12.4 to 13.0 m were still being excavated. Rock-bursts have occurred frequently during tunnel excavation under high geostress conditions. There has been a lot of research into initiation and development of rock-bursts, including laboratory tests, micro seismic monitoring and numerical analysis. In this study complete monitoring facilities were implemented to study the initiation and development of rock-burst during tunnel excavation, such as digital borehole camera, cross-hole acoustic apparatus etc.

Monitoring apparatus was installed prior to tunnelling, to obtain effective preliminary data, and numerical simulations were carried out to determine the potential rock-burst zones, locating fractured zones and the changes in stress and energy in the surrounding rock mass, as shown in Figure 4.4.1. The results of numerical modelling showed that the northern sidewalls of the test tunnels, as indicated in Figure 4.4.2, demonstrated a greater rock-burst risk potential. Therefore, more attention was focused on the northern sidewall and most of the boreholes were drilled from auxiliary tunnel A (M1 and M2) to test tunnels B and F, as shown in Figure 4.4.3 (Li et al, 2012).

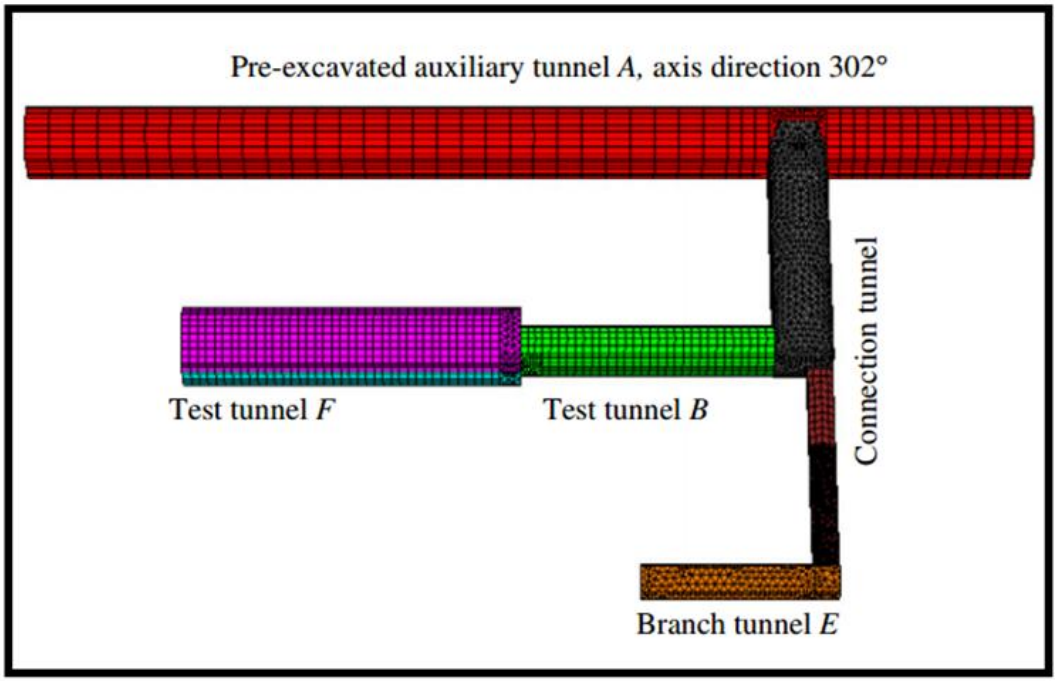


Figure 4.4.1: Three-dimensional numerical model of tunnels in the rock-burst test zone (Li et al, 2012).

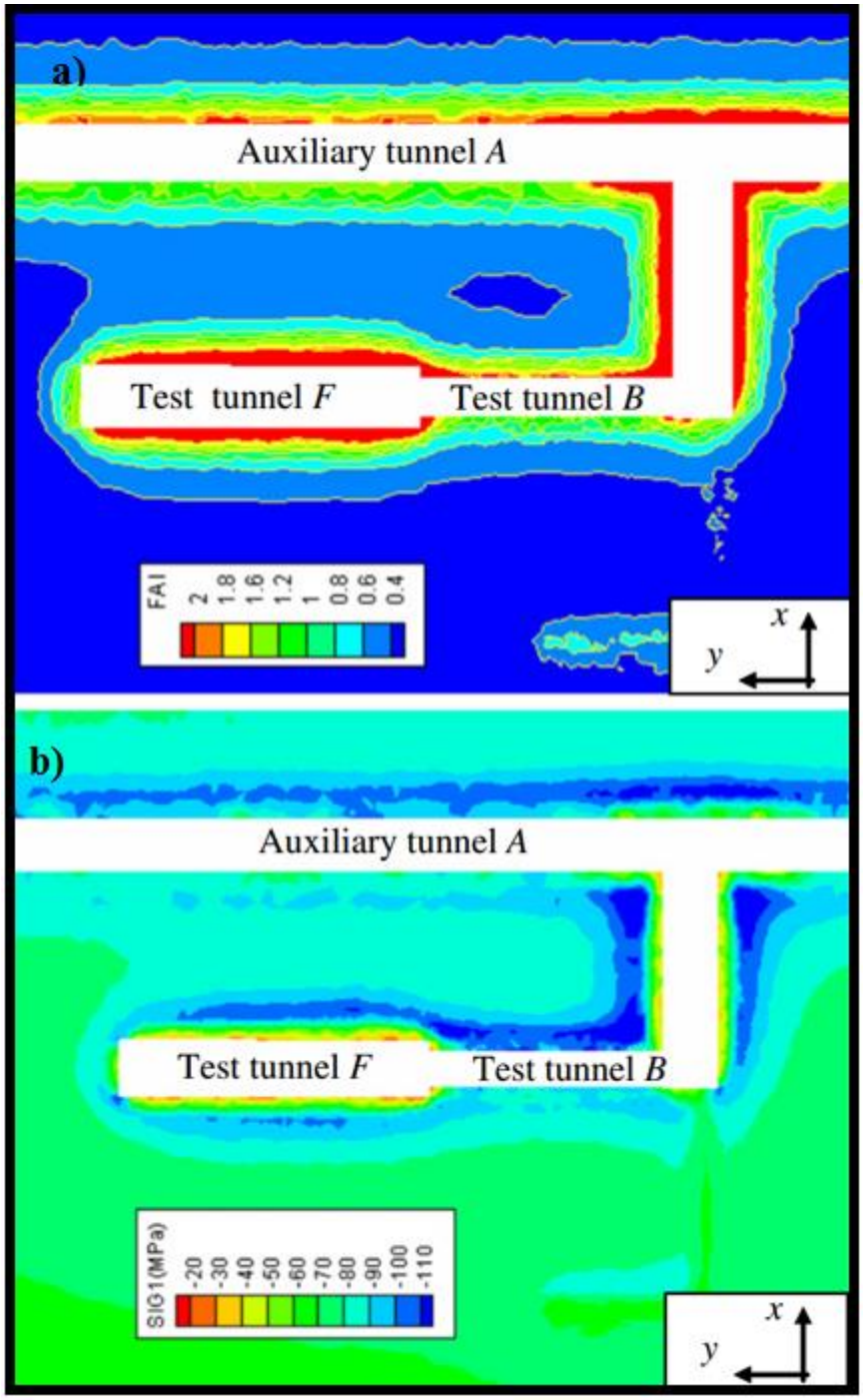


Figure 4.4.2: Numerical simulation of tunnel excavation at the horizontal a) Distribution of failure approach index (FAI—Failure Approach Index), b) Distribution of the maximum principal stress (σ1) (Li et al, 2012).

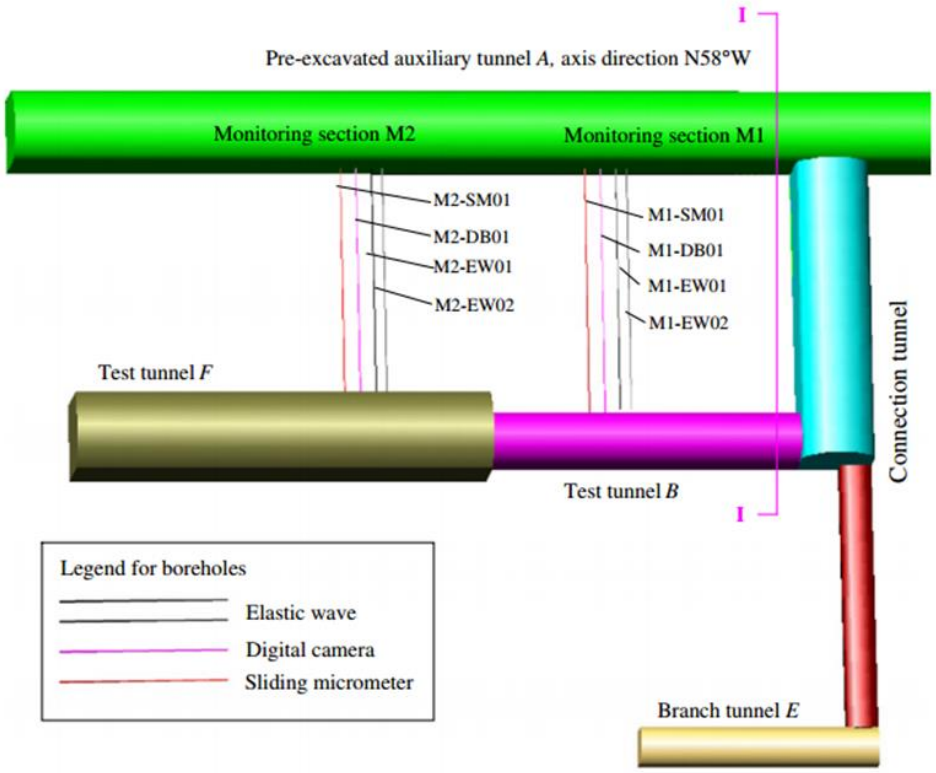


Figure 4.4.3: Layout of monitoring facilities around test tunnels B and F in Jinping II hydropower station (Li et al, 2012).

As the working face passes the monitoring section, the rock- burst was captured. Prior to this, cracks propagated and new cracks continued to appear as the tunnel advanced, as a result of high stress level and redistribution of stress, i.e. pre-existing crack width was 5.0 mm and subsequently, changing to 7.0 mm after excavation took place, as shown in Figure 4.4.4. The red lines indicate expansion of cracks and changes in their widths due to the stress readjustment and concentration (shown as a brightened colour on a digital borehole camera).

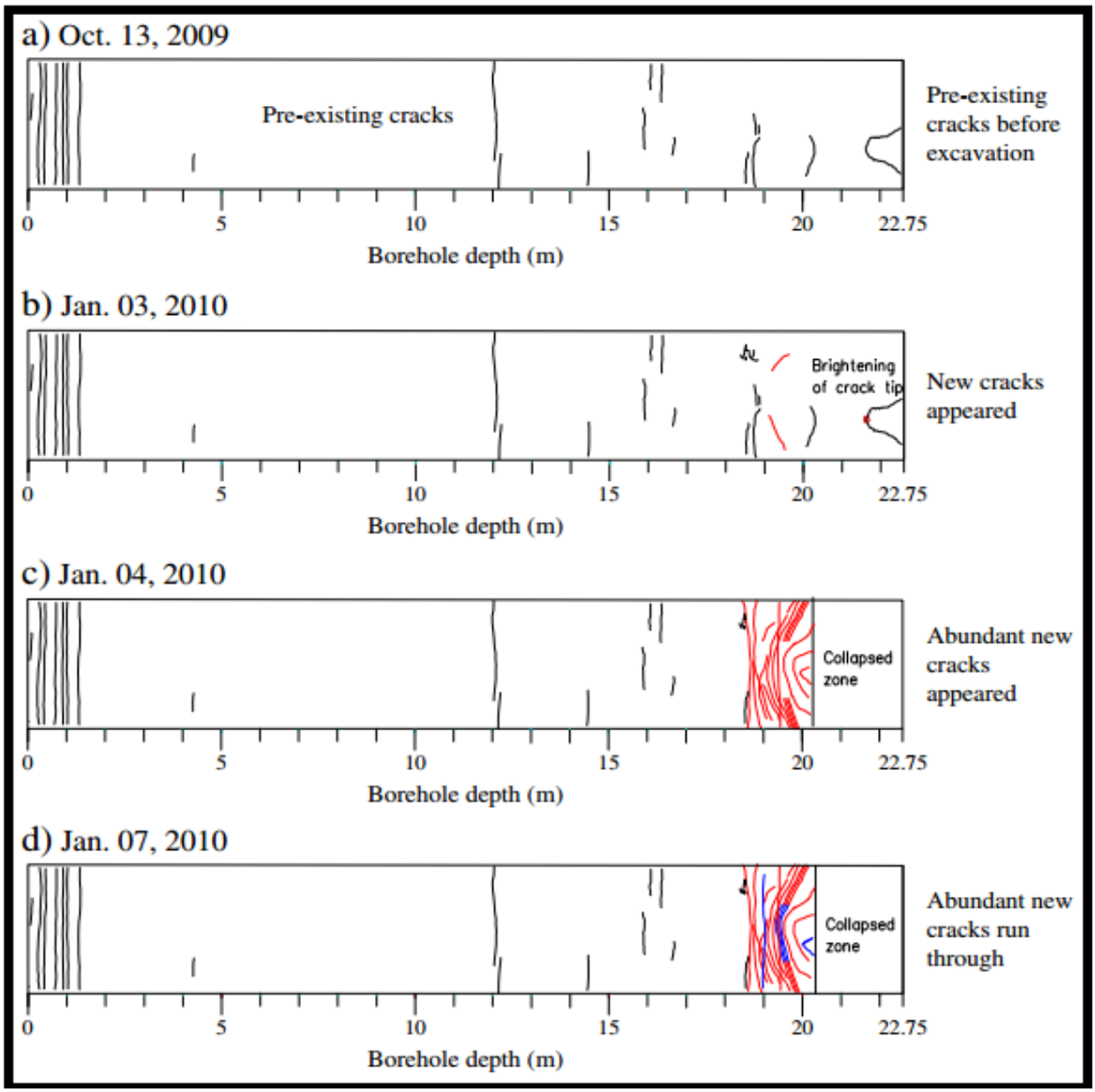


Figure 4.4.4: Sketch plan of crack development measured at different times: a) before excavation; b) excavation of top heading of test tunnel F complete; c) 10.0 m of bench excavated, before rock-burst; (d) 21.0 m of bench excavated, before rock-burst (Li et al, 2012).

The following observations were drawn up, in terms of the stages that took place prior to rock-burst occurrences:

a) Stress redistribution

Before tunnel excavation, the immediate rock mass was subjected to the in situ stress and at equilibrium. As the tunnel excavation took place, the in situ stress was disturbed in such a way that there was a decrease in radial stress and an increase in tangential stress. Subsequently, the fracturing process in the rock mass took place. There are similar observations by Zhang et al (2011b) and Martin (1997).

b) Energy accumulation.

As the stress redistribution took place after or during tunnelling, the increase of tangential principal stress caused high elastic energy to be generated further in the rock mass. As a result, stress concentration occurred due to the stressed surrounding rock mass, resulting in a growth in cracks.

c) Crack initiation, propagation and coalescence.

This is shown in Figure 4.4.4, where stress path (increase, decrease and rotation) caused new cracks to be formed, increase in width, and subsequently, interconnect, forming critical zones. Haimson and Chang (2000), Cai et al (2004) and Li et al (2011) recorded similar studies.

d) Spalling and buckling of fractured rocks.

The process of crack initiation, propagation and coalescence took place prior to rock bursting, resulting in accumulation of energy in the unloading zone, as the number of cracks increases. As the energy accumulates above a critical level, rock-burst took place, part of the energy being consumed by rock fracturing, while the remaining elastic strain energy was converted into kinetic energy, causing the fractured rock around tunnel to spall, buckle and eject from original rock mass.

4.4.3. Rock burst and slabbing failure and its influence on TBM excavation at headrace tunnels in Jinping II hydropower station (Gong et al, 2012)

This section contains a brief description of the case study described by Gong et al (2012).

According to Gong et al (2012), driving tunnels in brittle rock at great depth often involves problems caused by stress-driven failure process, such as slabbing and rock burst. As far as Jinping II Hydropower Station Project is concerned, the overburden depth along the headrace tunnels is very high, approximately 70% greater than 1500 m, with a maximum of 2525 m. The maximum principal stress is believed to be above 60 MPa in the rock mass along the headrace tunnel; hence, stress driven rock failures occur as a result of the overburden. Furthermore, rock bursts were experienced during excavation of the access tunnels and an adit, and therefore, minor to extreme rock bursts were expected to occur during construction of the headrace tunnels. This presented the main engineering problem during the excavation of the headrace tunnels. Figure 4.4.5 shows the mechanisms of the rock burst and spalling that were experienced during the excavation of these tunnels.

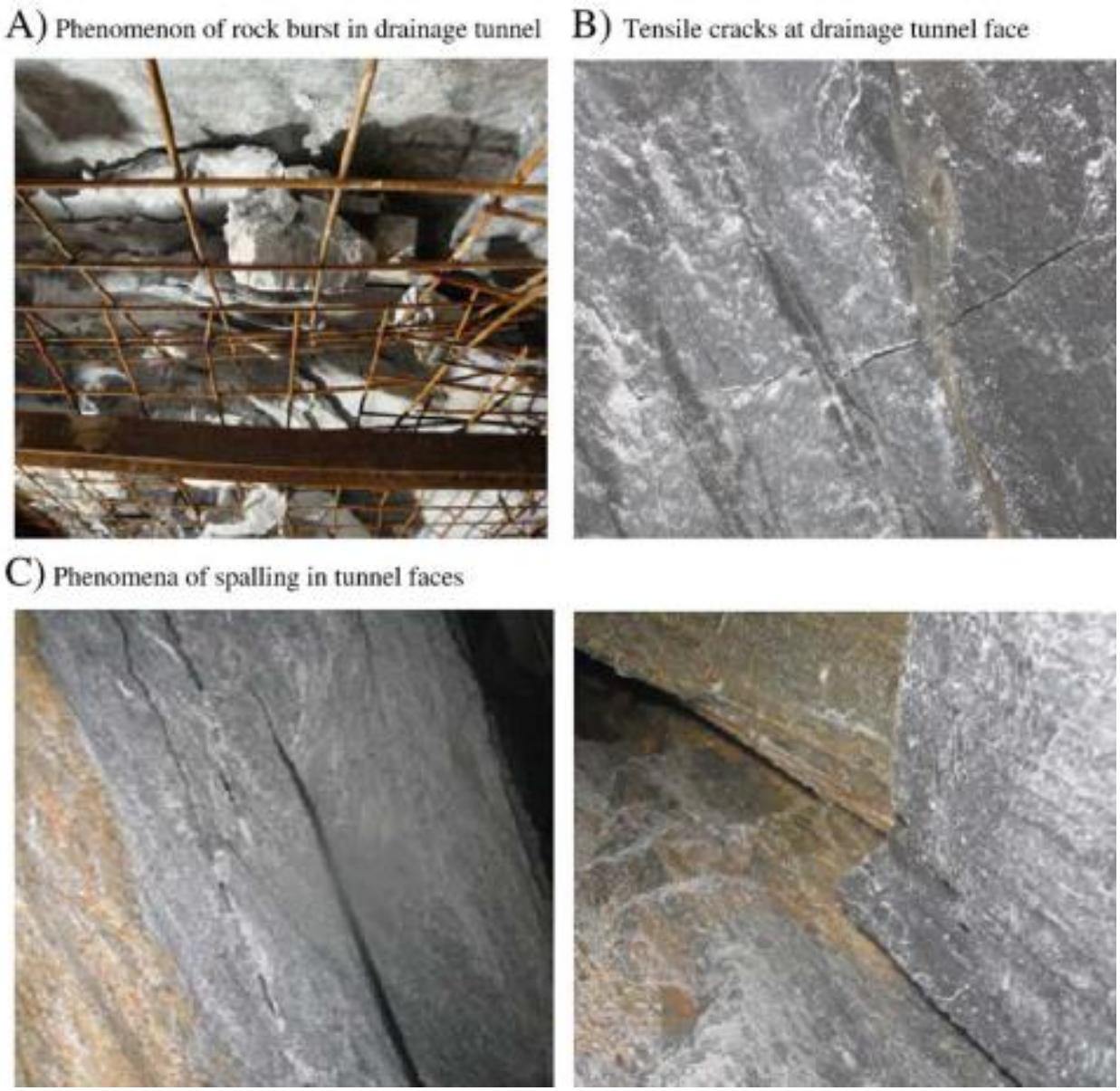


Figure 4.4.5: Phenomena of rock burst and spalling in the field (Gong, et al., 2012).

In order to contextualise the process of slabbing and rock burst formation in the surrounding rock along the tunnel arrangement, four rock samples were tested. The magnitudes of stresses applied in these experiments were determined with the assistance of numerical methods. Largely, this was to attain the stress distribution in the surrounding rock after tunnel excavation, considering the initial

geostress along the tunnel and through back analysis. Loading and unloading of the samples were based on the determined initial geostresses, in order to simulate the stress concentration process taking place at the excavation boundaries. The sequence of events, prior to rock bursting, involved: unloading of horizontal stresses from the test samples, while increasing the vertical stresses, which resulted in vertical cracks being initiated. The failure mode of the samples, exhibited that of slabbing failure, i.e. vertical spalling cracks were the prominent fracture type. Figure 4.4.6 indicates the failed rock samples, where the slabbing delineation and fracture faces are virtually parallel to the direction of the maximum principal stress. This failure mode was a clear representation of the failure mechanism of the rock mass at the excavation site.

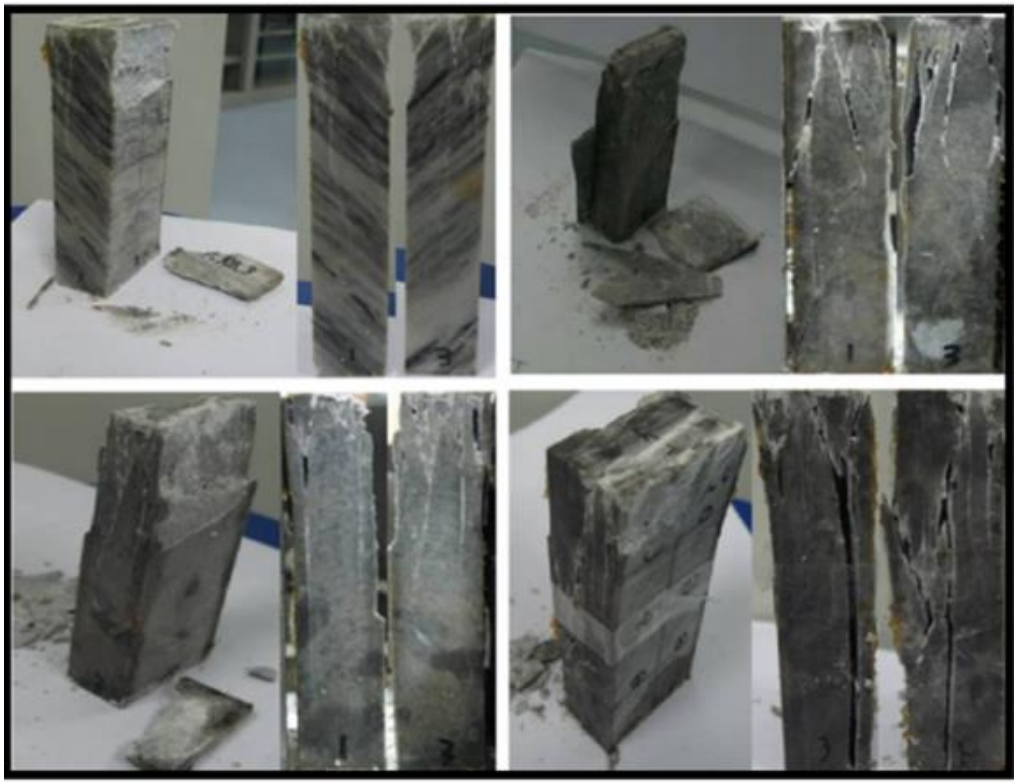


Figure 4.4.6: Slabbing characteristics of rock samples (Gong et al., 2012).

4.4.4. Engineering geology of Alpine tunnels: past, present and future (Loew et al, 2010)

This case study concerns an evaluation of engineering geological contributions to the design and construction of deep Alpine tunnels by Loew et al (2010). As far as this research is concerned, the rock mechanics lessons learnt from completed Lötschberg and Gotthard Base tunnels are emphasized. These include occurrences such as spalling and rock bursting.

a) The Lötschberg Base Tunnel (Loew et al, 2010)

Lötschberg base tunnel is a 34.6 kilometre long, single-track single-tube railway tunnel crossing the northern part of the Swiss Alps at an elevation between 655 and 828 metres above sea level. The tunnel was constructed with three intermediate adits. The maximum overburden was about 2000 m. The tunnel excavations were completed in April 2005 and the tunnel went into viable operation mid-2007. The method of excavation was by means of TBM, during which spalling and bursting were experienced, mainly in front of the machine. In some instances the ejection of blocks was so violent that the TBM cutter head vibrated for a period of several minutes.

b) Gotthard Base Tunnel

The Gotthard base tunnel is the longest tunnel of the AlpTransit corridor in central Switzerland, which is 57 kilometres in length, and connects Erstfeld in northern Switzerland to Bodio in southern Switzerland (Loew et al, 2010). The highest overburden is 2500 m and the tunnel was constructed using three intermediate adits. The construction work of the adits started in 1996 and of the primary tunnel sections in 2000. The method of excavation was by means of TBM.

c) Spalling and Rock Bursting (Loew et al, 2010)

The concepts of spalling and rock bursts were adopted from South African mines, documented by Stacey and De Jongh (1977) and Fairhurst, and Cook (1966). These failure modes, which became common as mines around the world developed deeper in search of minerals, were also challenges in the deep Alpine tunnels, as shown in Figure 4.4.7. These failure modes presented a substantial safety hazard for workers directly behind the shield of the TBM. In some cases, as the tunnel advanced, it would interact with subtle structures in the rock mass. This led to delayed release of spall damaged ground, which was associated with substantial energy release in the form of a strain burst (Kaiser et al. 1996) as shown in Figure 4.4.7.d. Substantial spalling and bulking within the TBM shield presented challenges, in terms of safety and jamming of the shield.

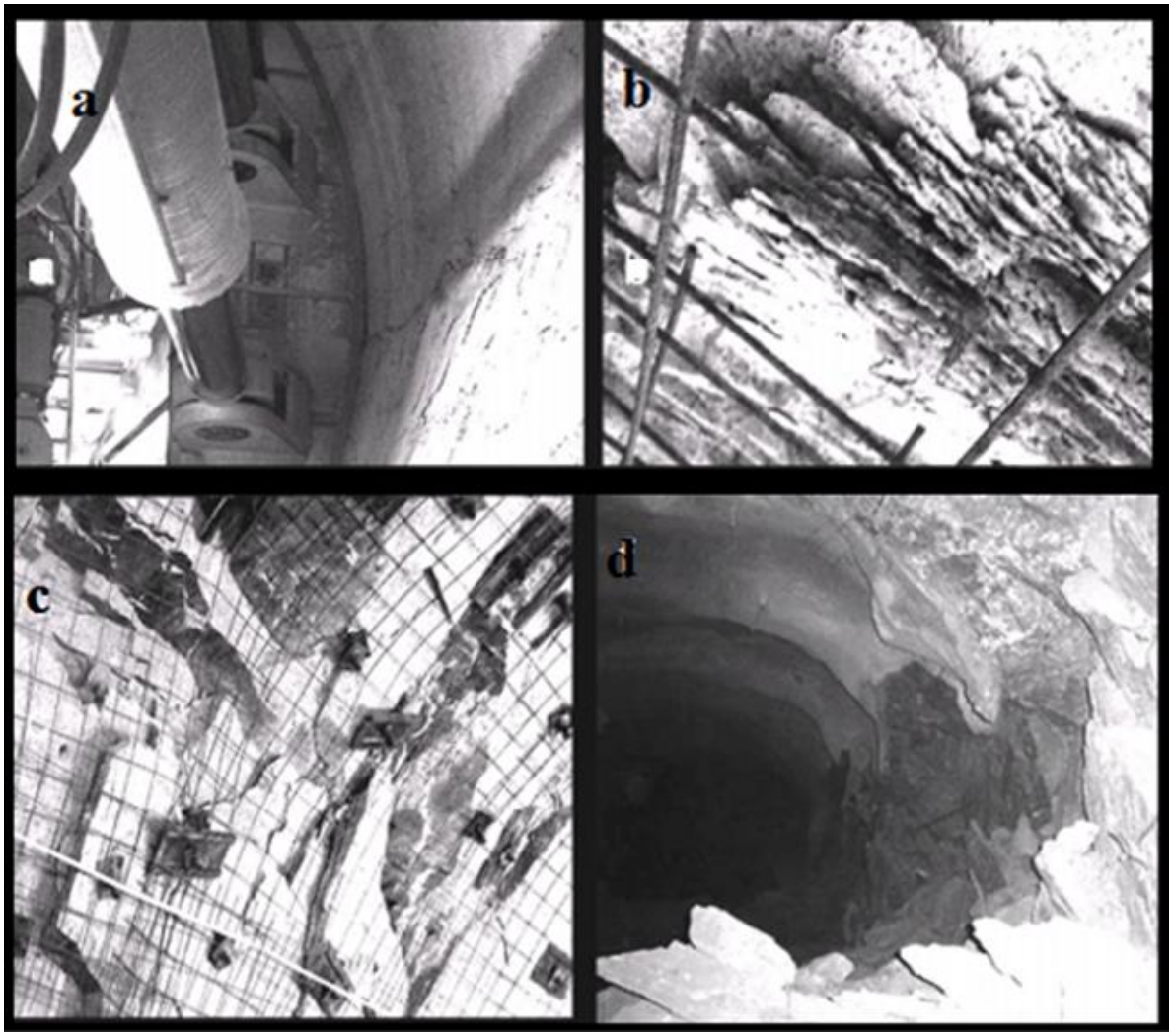


Figure 4.4.7: Increasing levels of brittle spalling and operational challenges: a) spalling initiation (small scales on the wall); b) spalling pieces of grain thickness penetrating into wall; c) parallel wall slabs; d) strain bursting of spall damaged ground due to high stresses (Loew et al, 2010).

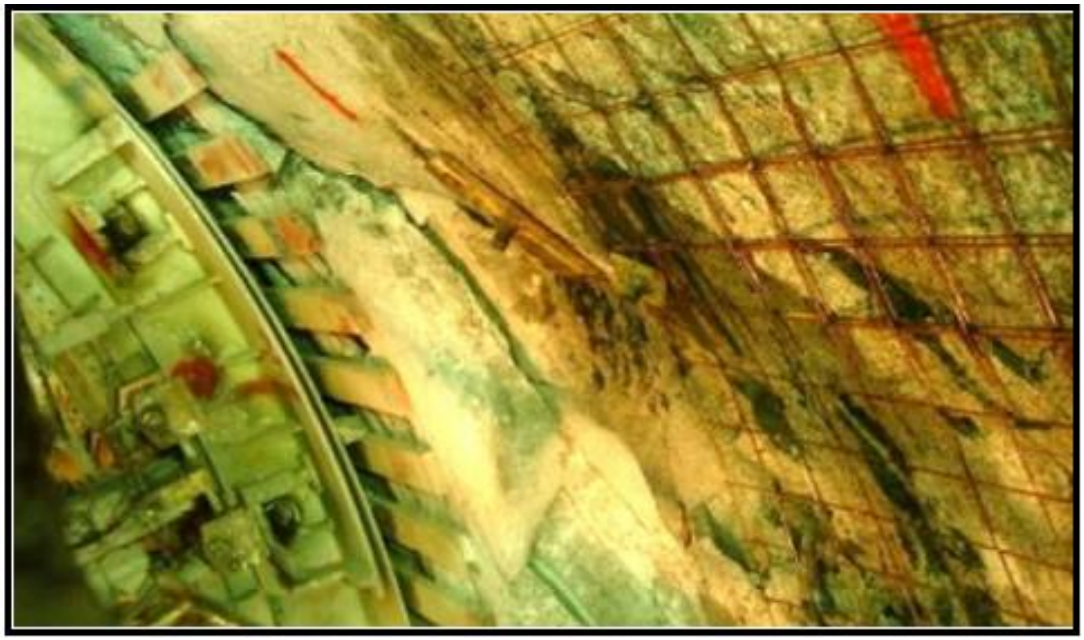


Figure 4.4.8: Spalling and energetic slab generation behind TBM shield (Loew, et al. 2010).

In some areas, as shown in Figure 4.4.8, not all spalling was violent or led to rock bursting, i.e. there was relatively minimal energy involved in the extension cracking process that led to spalling, which involved the creation of boundary parallel extension fractures. Depending on the stress level, these fractures may subsequently buckle violently or non-violently.

4.5 Conclusion

It is apparent that rock fracturing is critical for prediction of failure around excavations. Hence the rock mass behaviour, such as the strength and deformation, must be established. The extension strain criterion for predicting fracturing and failure appears to be beneficial in this regard. The criterion predicts failure, even in areas of low stress magnitudes, which occurs when total extension strain in the rock exceeds a critical value characterising the rock type.

Knowledge of the extent of fracturing is beneficial to the boring projects, in particular, when using TBM methods, which are more susceptible to rock bursting.

These case studies give a clear indication of the impact of extension fractures on the boring operations, ranging from spalling to buckling and even strain busting, depending on the amount of energy ejected. Prediction of these fractures can be beneficial to a boring project. This is apparent in the case studies presented, where numerical analyses were done and appropriate monitoring devices were installed. The following chapter presents the numerical methods and methodologies applicable to rock engineering concepts. Steps that have been followed in modelling are given.

CHAPTER 5

NUMERICAL MODELLING AND MODELLING METHODOLOGY

5.1 Introduction

Numerical methods provide solutions for problems that contain multifaceted scenarios and behaviours (Thamer, 1998). Numerical modelling can help the geotechnical engineer in designing underground openings and support structures. In some instances, if substantial geological and geotechnical data are obtainable, then extensive predictions of deformations, stability and support loads can be determined by numerical stress analyses. In cases where there are not enough data, the numerical model can still be adopted to perform sensitivity analyses, giving an indication of the probability of the possible responses of a system, under various scenarios. This can help in formulating mechanisms for further acquisition of relevant data. (Coulthard, 1999)

According to Hudson (2003), the main aim of modelling is to enable predictions of the future from the past. For instance, in rock mechanics problems, a prediction of the behaviour of a specific tunnel excavated in a rock mass at different orientations can be made, and the solutions are incorporated in the designs. In this research report, a numerical model is used to predict the extension fractures ahead of and around faces and walls of mechanically driven excavations, and their effect on stability.

5.2 Numerical Modelling Methods

Numerical methods in rock engineering can be divided into either differential (domain) or boundary element (integral) methods and the detailed information and associated mathematics are well documented in Jager and Ryder (1999) and Brady and Brown (2004):

1. Differential methods

These methods involve modelling a specific volume (three dimensional) or area (two dimensional) of the rock mass, that is, the problem domain is divided into a set of discrete elements. The rock mass is infinite in lateral extent, but the model must be restricted at some simulated boundaries, which are sufficiently far away, so that they do not affect the area of interest. There are three types of differential methods; these are the Finite Difference Method (FDM), the Distinct Element Method (DEM) and Finite Element Method (FEM).

2. Boundary element (BE) or Integral methods

These methods only consider the boundary of the excavations, i.e. boundaries are divided into distinct elements, and the stresses and displacements in the area outside the boundary are continuous. There is no need for artificial boundary conditions since the discrete elements are positioned and solved at the boundaries, hence the dimension of the problem to be solved is reduced. This results in an increase in computation efficiency. There are three types of boundary element methods, which are the Fictitious Stress (FS) method, the Displacement Discontinuity (DD) method and the Direct Boundary Integral method.

5.3 Modelling Methodology

The application of modelling in rock engineering involves a thought process, that describes the methodology of modelling rock engineering problems. The following are the suggested steps that outline the methodology that can be applied to problem-solving in rock engineering (Jager and Ryder, 1999):

1. Determine the problem area and the extent of the problem;

In the case of this research, the problem area is based on the prediction of the possible initiation and orientations of extension fractures ahead of and around faces and walls of mechanically driven excavations. The extent of the problem is the stability issue, which could potentially result in possible failure.

2. Design a number of potential mining strategies to alleviate the problems.
3. Define relevant design criteria.

Based on the above descriptions the most relevant criterion is the extension strain criterion.

4. Develop a model that encompasses the detail to assess the mining strategies in terms of the design criteria;

This describes the constitutive models and parameter selection, which describe the stress strain relations of the rock mass that defines the precision of the results. Furthermore, there is no constitutive model available that encompasses all the features of rock behaviour outlined by parameters that can be acquired from laboratory results. There is a variety of commercially offered models but, in the case of this research, it was only necessary to make use of a linear elastic model.

5. Choose the relevant numerical software;

This research involves an analysis of the stress distribution around the face of a bore, where different depths were considered, and stresses corresponding to these depths were determined. A boundary element program was chosen since this simplified the analysis of the three dimensional problem. The analyses provided the following results:

- Principal strains and stresses at different points ahead of the face, indicating zones of tensile stress, were calculated;
- The average thicknesses of potential rock slabs were predicted, which were related to the critical extension strain magnitude (this signifies the macrostrain level at which major fracturing will take place).

In the case of this research, the Examine 3D boundary element package was selected.

6. Perform simulations on each strategy using the model and the specified design criteria. In the case of this research, the following steps were followed in Examine3D:
    - Polylines were built to define three dimensional geometries representing tunnels of different sizes.
    - Boundary element meshes were generated from the built polylines.
    - Subsequently, data files, with specified field points and analysis parameters, were written as EX3 files in order to be computed in the boundary element stress analysis program (COMPUTE$^{3D\text{-}BEM}$).

7. Analyse the results of the simulations in terms of the specified design criteria.
8. Select a mining strategy based on the analyses.

5.4 Conclusion

This chapter emphasises the significance of numerical modelling as applicable to rock engineering. Factors such as its application, limitation due to availability of data, and available numerical methods, are discussed. Numerical methods, and steps involved in generating the numerical model for this research, are outlined. The next chapter discusses the numerical modelling results obtained using Examine3D, including stress distributions, predicted fractured zones (as function of tunnel diameter), using an extension strain criterion, and orientations of the potential fractures.

CHAPTER 6

RESULTS OF NUMERICAL MODELLING AND DISCUSSION

6.1 Introduction

This chapter discusses the results obtained from Examine 3D modelling program. Principal stress distributions around bored excavations in quartzite rock, relative to the in situ stresses, are analysed. Furthermore, extension strain distributions ahead of the excavations, indicating possible fractured zones, are assessed assuming the critical strain ranging from 180 to 270 microstrain for crack initiation and from 504 to 864 microstrain for the crack damage (failure), for the quartzite. In order to evaluate the stability of predicted fractures, their orientations are determined. Lastly, potential slabs or plates created are evaluated for possible buckling, assuming the critical extension strain of 200 microstrain.

6.2 Stress Distributions around Excavations

Stress distributions around tunnels of various diameters, for different in situ stresses, have been analysed using Examine 3D. The generated plots indicated similar principal stress distributions, under the same in situ stress conditions, around tunnels of different diameters. However, it is worth noting that the extent of failure varies for different tunnel sizes; this is discussed in subsections 6.3 and 6.5. Only eight-metre diameter tunnel results are presented in this subsection.

The input parameters used for the analyses are summarised in Table 6.2.1 and Table 6.2.2. Three dimensional geometrical structures were generated using these parameters, which have modelling features as indicated in Table 6.2.3. The plots are taken from cross sections at two places in the geometry, as shown in Figure 6.2.1 ad Figure 6.2.2. Each description of the plots is analysed based on σ1 and σ3, as shown in Figure 6.2.3 to Figure 6.2.22.

Table 6.2.1: Input parameters of material properties obtained from literature

Parameters	
Elastic modulus	50 GPa
Poisson's Ratio	0.2 and 0.3
Uniaxial Compressive strength	180MPa

Table 6.2.2: Alternative in-situ stress fields obtained from Wesseloo and Stacey (2006).

Stress (MPa)		
σ x	σ y	σ z
70	35	70
35	35	70
52.5	25	70
35	17.5	52.5
52.5	70	25

Table 6.2.3: Modelling parameters used in Examine3D.

Tunnel Diameter (m)	Elements	Nodes
2	488	246
4	1136	570
6	1384	694
8	8118	4061
8	10754	5394

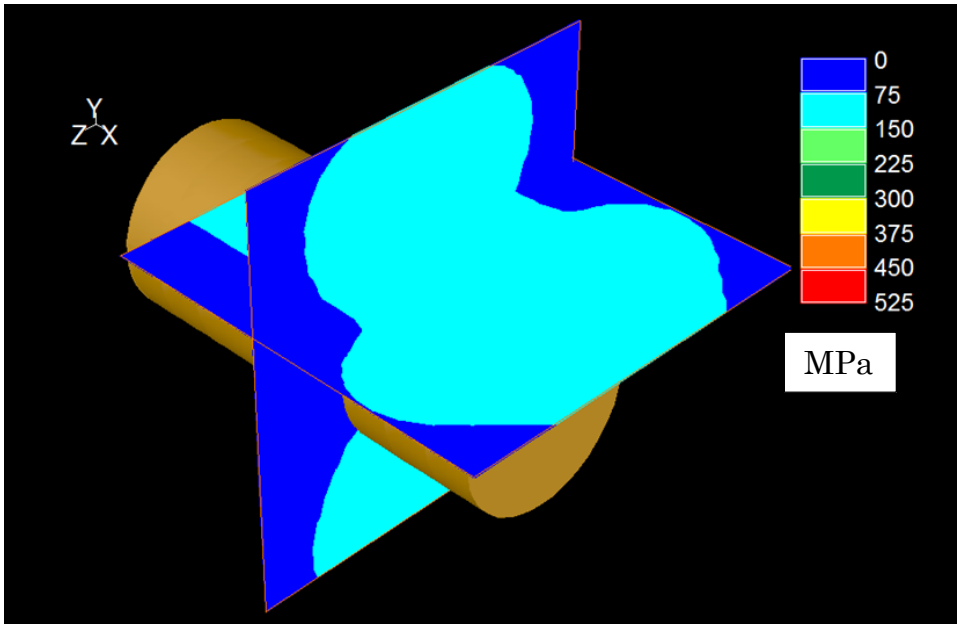


Figure 6.2.1: The perspective view depicting the cutting planes of σ1 distribution plots on an eight-metre diameter tunnel.

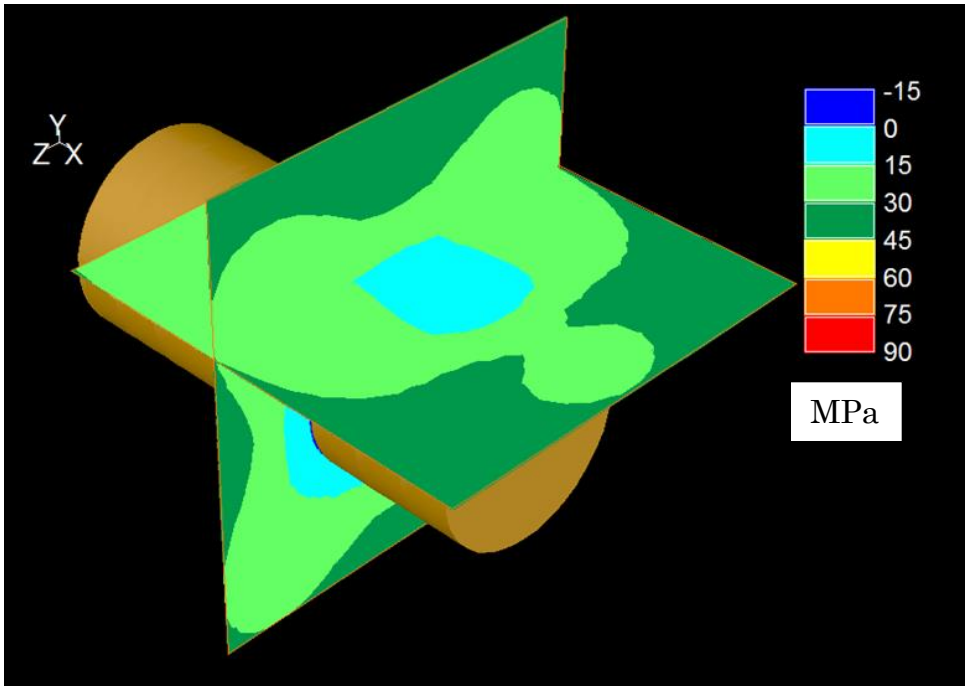


Figure 6.2.2: The perspective view depicting the cutting planes of σ3 distribution plots on an eight-metre diameter tunnel.

6.2.1 Analyses results for an eight-metre diameter tunnel (σx= 70 MPa, σy= 35 MPa, σz= 70 MPa)

Figure 6.2.3 and Figure 6.2.4 show major principal stress (σ1) distribution contour plots. It can be noted in Figure 6.2.3 that the high stress levels exist ahead of the tunnel face, ranging from 75 to 150 MPa, which are higher than the in situ stresses. The further away from the tunnel, the stress levels tend to the virgin stress state. Figure 6.2.4 shows the cross section across the length (x-axis) of the tunnel, where high stress concentrations are visible at the hangingwall and footwall, with sidewalls showing a sign of de-stressing. Figure 6.2.5 and Figure 6.2.6 show the minor principal stress (σ3) distribution contour plots. It can be seen in Figure 6.2.5 that σ3 values show a slight tension on the sidewalls, with the maximum value of 15 MPa. Figure 6.2.6 shows σ3 values ranging from 15 MPa to 30 MPa ahead of the tunnel face, which are below in situ stress levels.

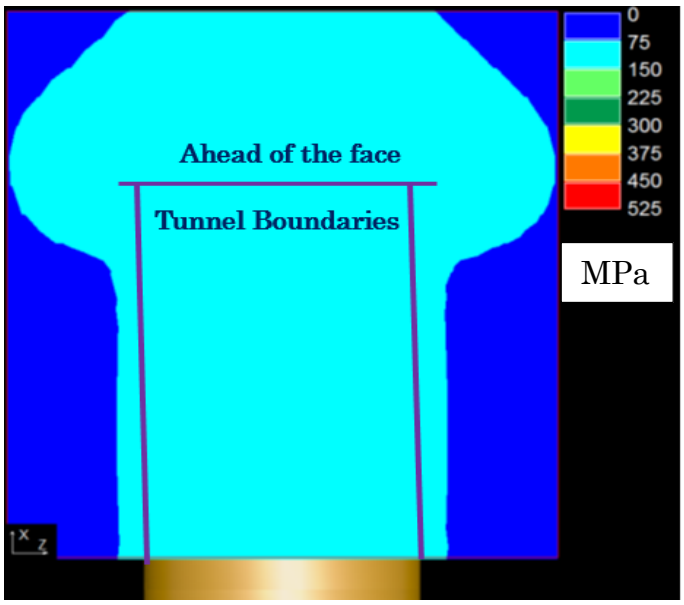


Figure 6.2.3: Top view of cutting plane depicting σ1 distribution through the roof of an eight-metre diameter tunnel (σx= 70 MPa, σy= 35 MPa, σz= 70 MPa).

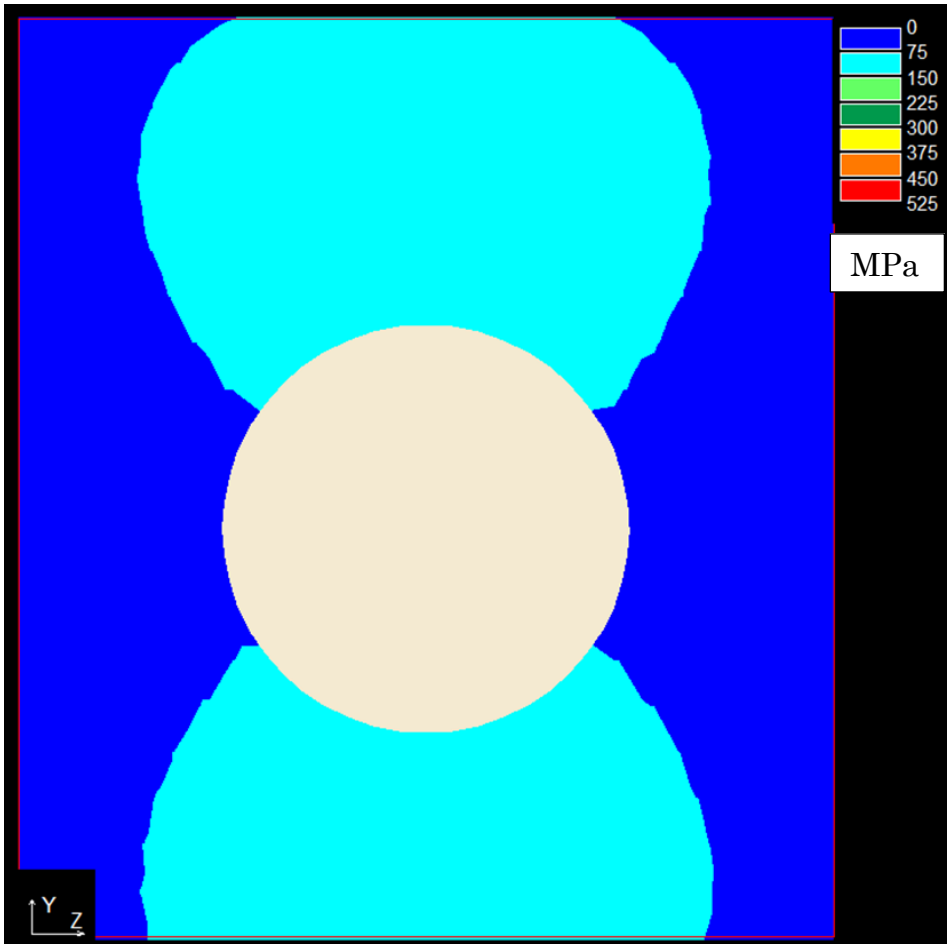


Figure 6.2.4: Front view of the cutting plane depicting σ1 distribution through a section of an eight-metre tunnel (σx= 70 MPa, σy= 35 MPa, σz= 70 MPa)

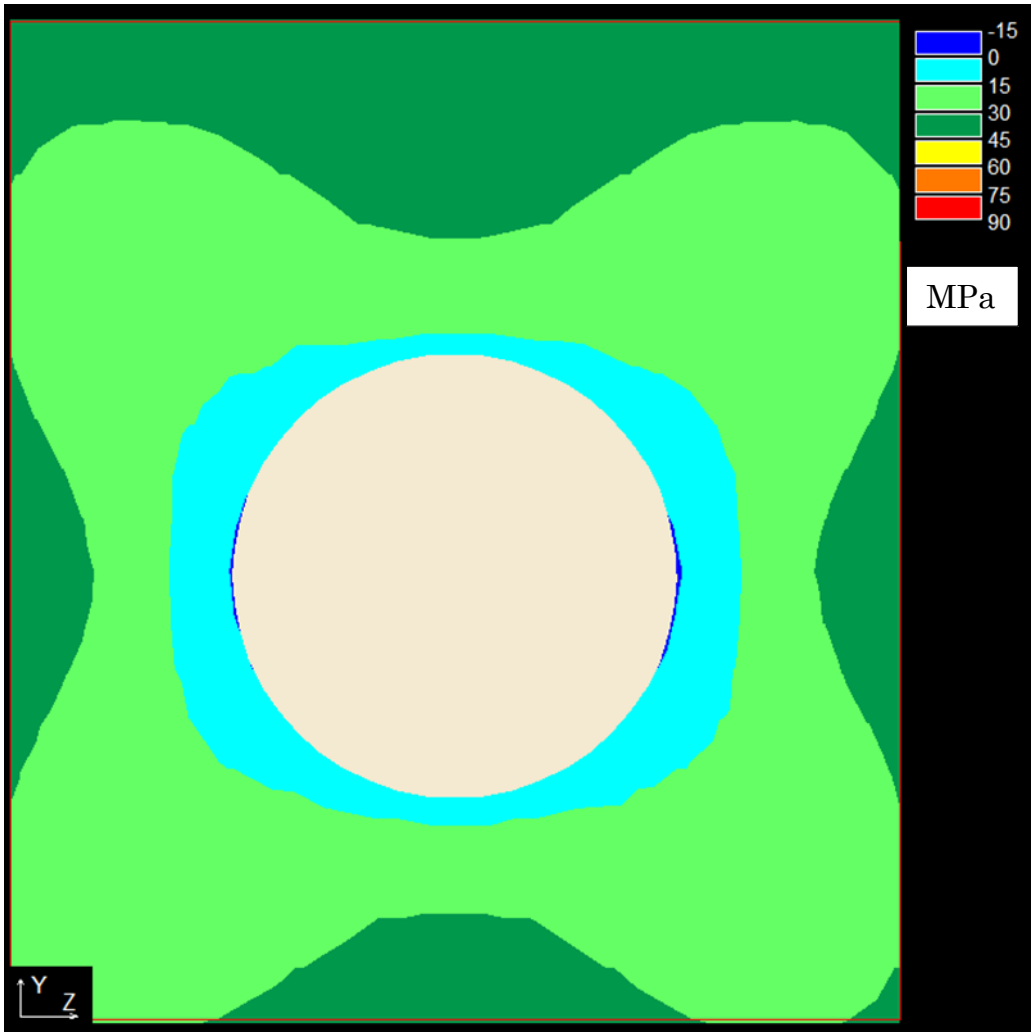


Figure 6.2.5: Front view of cutting plane depicting σ3 distribution through a section of an eight-metre tunnel (σx= 70 MPa, σy= 35 MPa, σz= 70 MPa).



Figure 6.2.6: Top view of cutting plane depicting σ3 distribution through the roof of an eight-metre diameter tunnel (σx= 70 MPa, σy= 35 MPa, σz= 70 MPa).

6.2.2 Analyses results for an eight-metre diameter tunnel (σx= 35 MPa, σy= 35 MPa, σz= 70 MPa)

Figure 6.2.7 and Figure 6.2.8 show major principal stress (σ1) distribution contour plots. It can be noted in Figure 6.2.7 that the high stress concentrations are exhibited at tunnel hangingwall and footwall, ranging from 110 MPa to 165 MPa, with sidewalls showing a sign of de-stressing. Figure 6.2.9 and Figure 6.2.10 show the minor principal

stress (σ3) distribution contour plots. It can be seen in Figure 6.2.9 that σ3 values show a slight tension on the sidewalls, with the maximum value of 9 MPa. Figure 6.2.10 shows σ3 values ranging from 18 MPa to 27 MPa ahead of the tunnel face, which are below in situ stress levels.

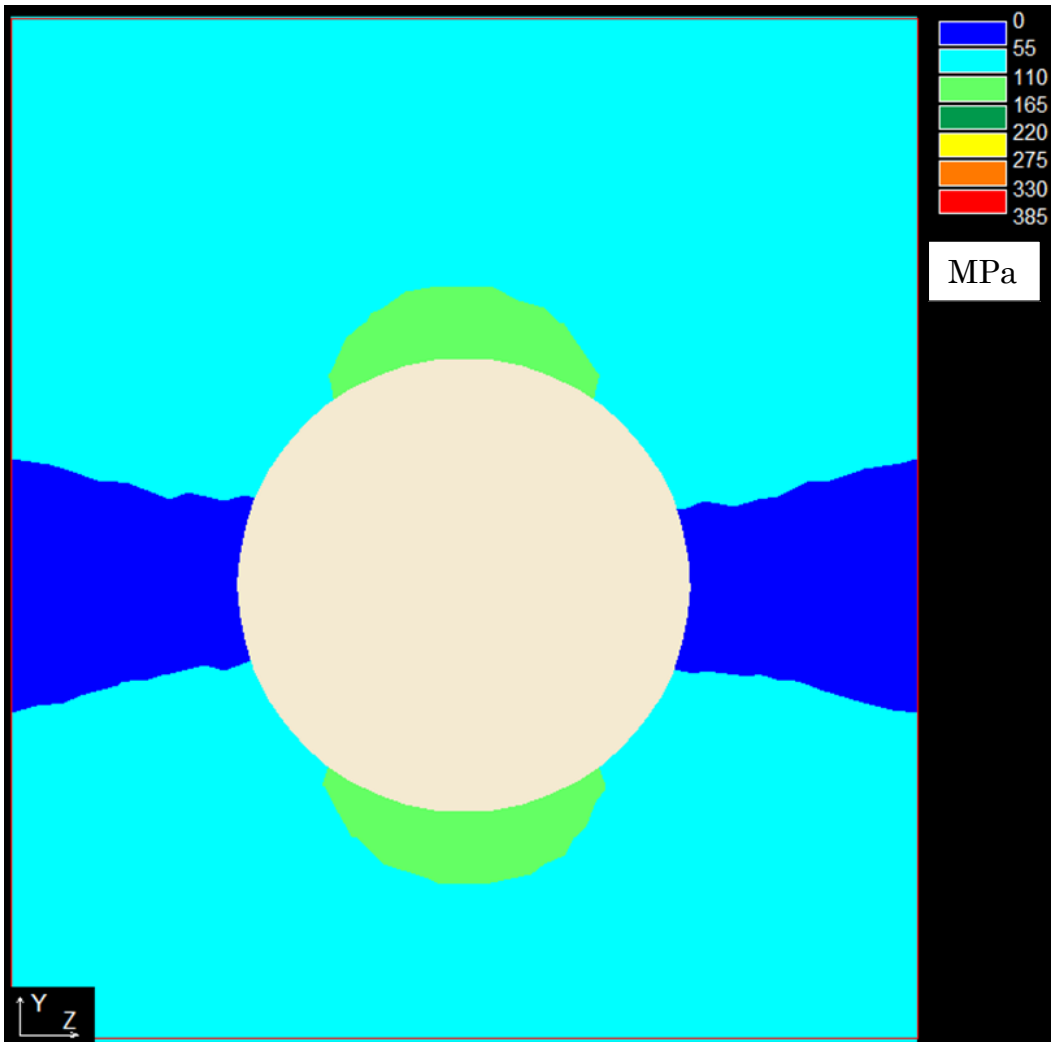


Figure 6.2.7: Front view of cutting plane depicting σ1 distribution through a section of an eight-metre diameter tunnel (σx= 35MPa, σy= 35 MPa, σz= 70 MPa).

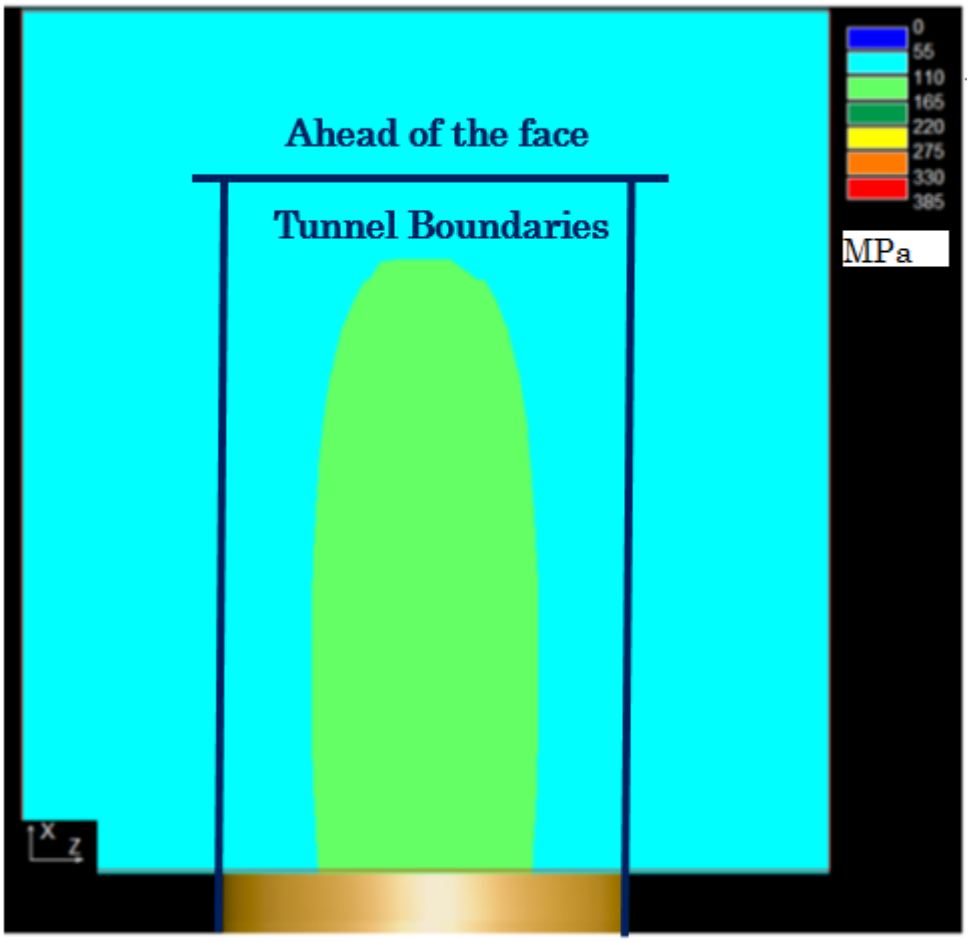


Figure 6.2.8: Top view of cutting plane depicting σ1 distribution through the roof of an eight-metre diameter tunnel (σx= 35 MPa, σy= 35 MPa, σz= 70 MPa).

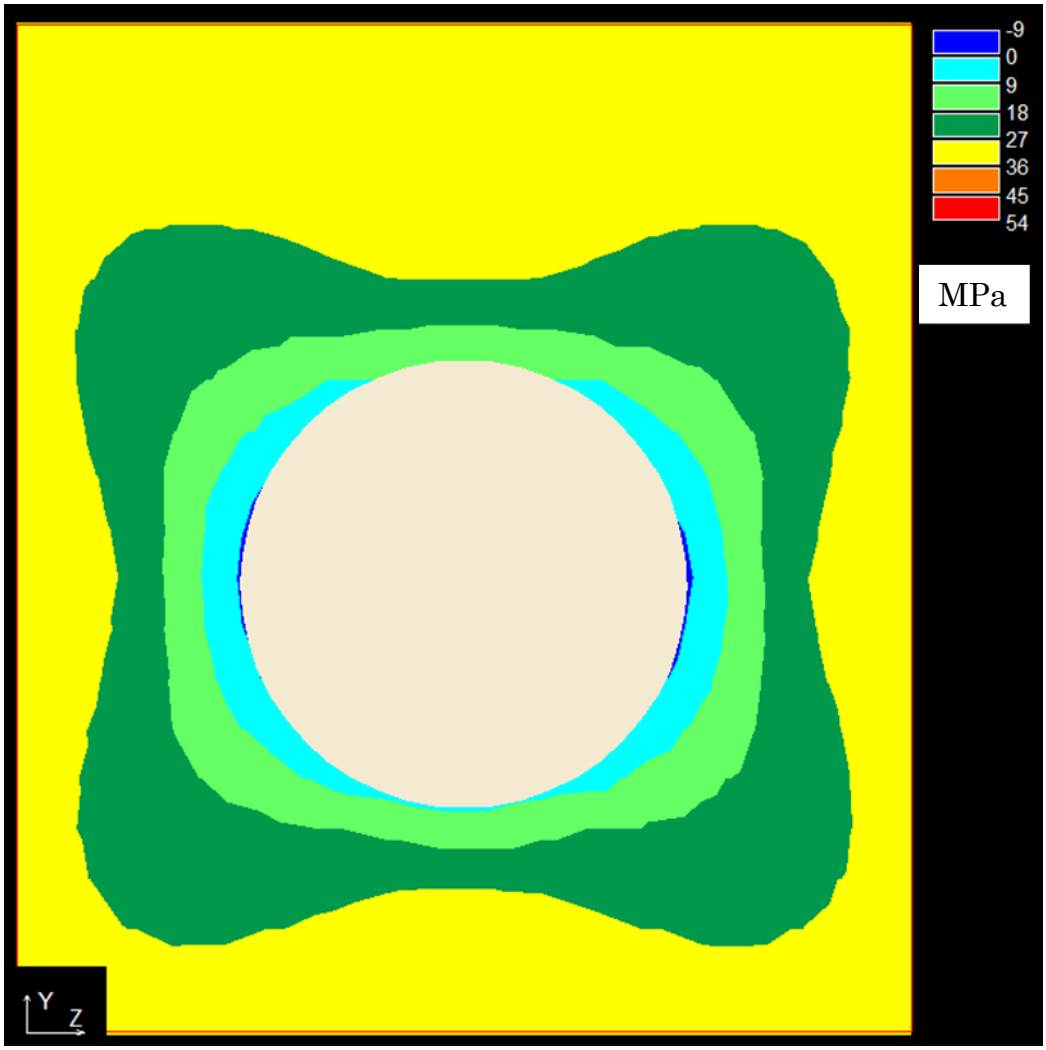


Figure 6.2.9: Front view of cutting plane depicting σ3 distribution through a section of an eight-metre diameter tunnel (σx= 35 MPa, σy= 35 MPa, σz= 70 MPa).

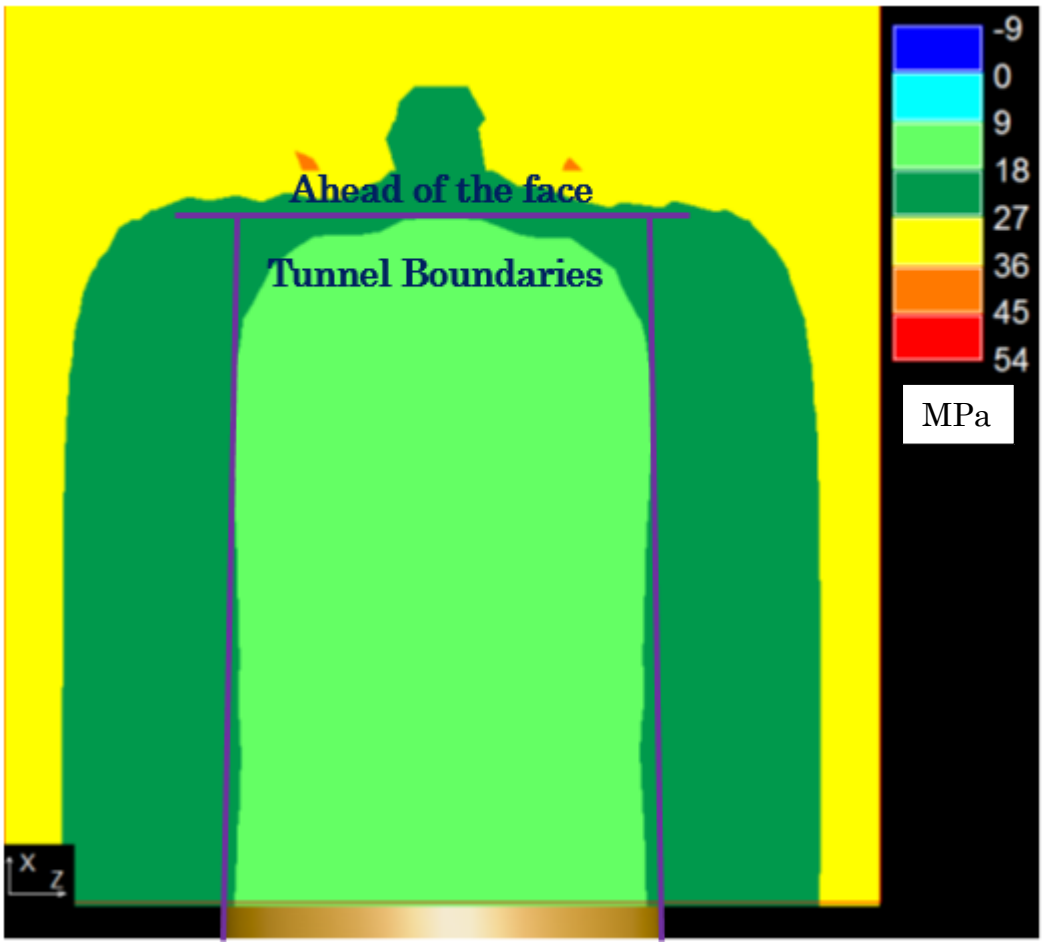


Figure 6.2.10: Top view of cutting plane depicting σ3 distribution through the roof of an eight-metre diameter tunnel (σx= 35 MPa, σy= 35 MPa, σz= 70 MPa).

6.2.3 Analyses results for an eight-metre diameter tunnel (σx= 52.5 MPa, σy= 25 MPa, σz= 70 MPa)

Figure 6.2.11 and Figure 6.2.12 show major principal stress (σ1) distribution contour plots. It can be seen in Figure 6.2.11 and Figure 6.2.12 that the high stress concentrations are exhibited at tunnel hangingwall and footwall, ranging from 130 MPa to 195 MPa, with sidewalls showing a sign of de-stressing. Figure 6.2.13 and Figure 6.2.14 show the minor principal stress (σ3) distribution contour plots. It can be noted in Figure 6.2.13 that σ3 values show a slight tension on

the sidewalls, with the maximum value of 9 MPa. Figure 6.2.10 shows σ3 values ranging from 9 MPa to 18 MPa ahead of the tunnel face, which are below in situ stress levels.

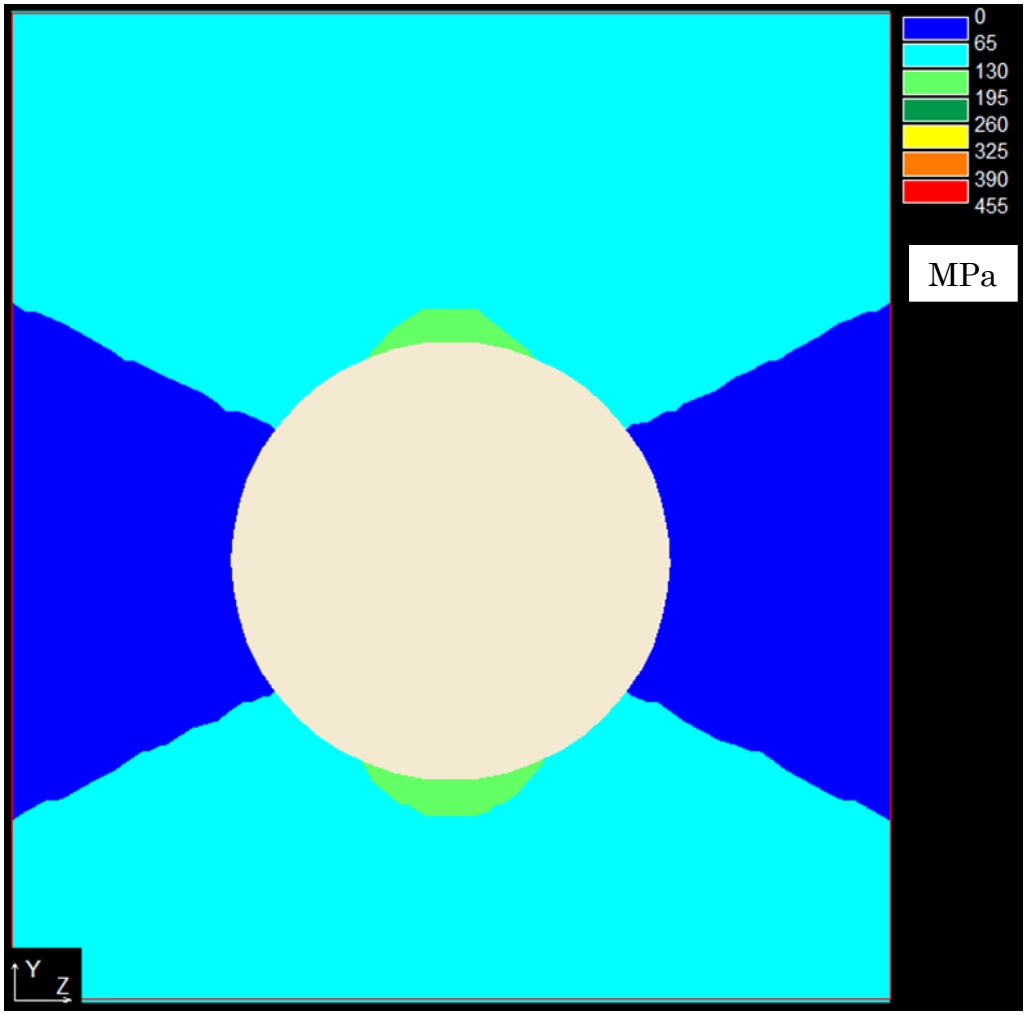


Figure 6.2.11: Front view of cutting plane depicting σ1 distribution through a section of an eight-metre diameter tunnel (σx= 52.5 MPa, σy= 25 MPa, σz= 70 MPa).

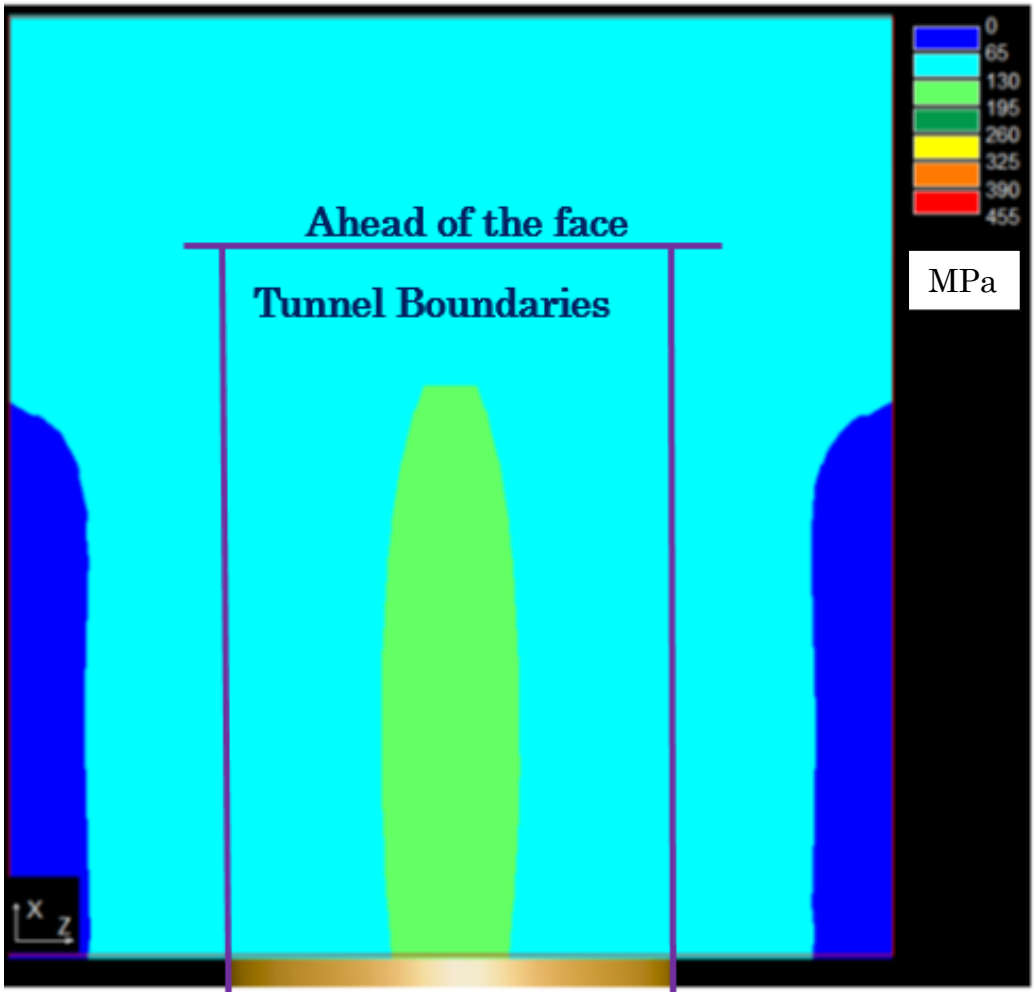


Figure 6.2.12: Top view of cutting plane depicting σ1 distribution through the roof of an eight-metre diameter tunnel (σx= 52.5 MPa, σy= 25 MPa, σz= 70 MPa).

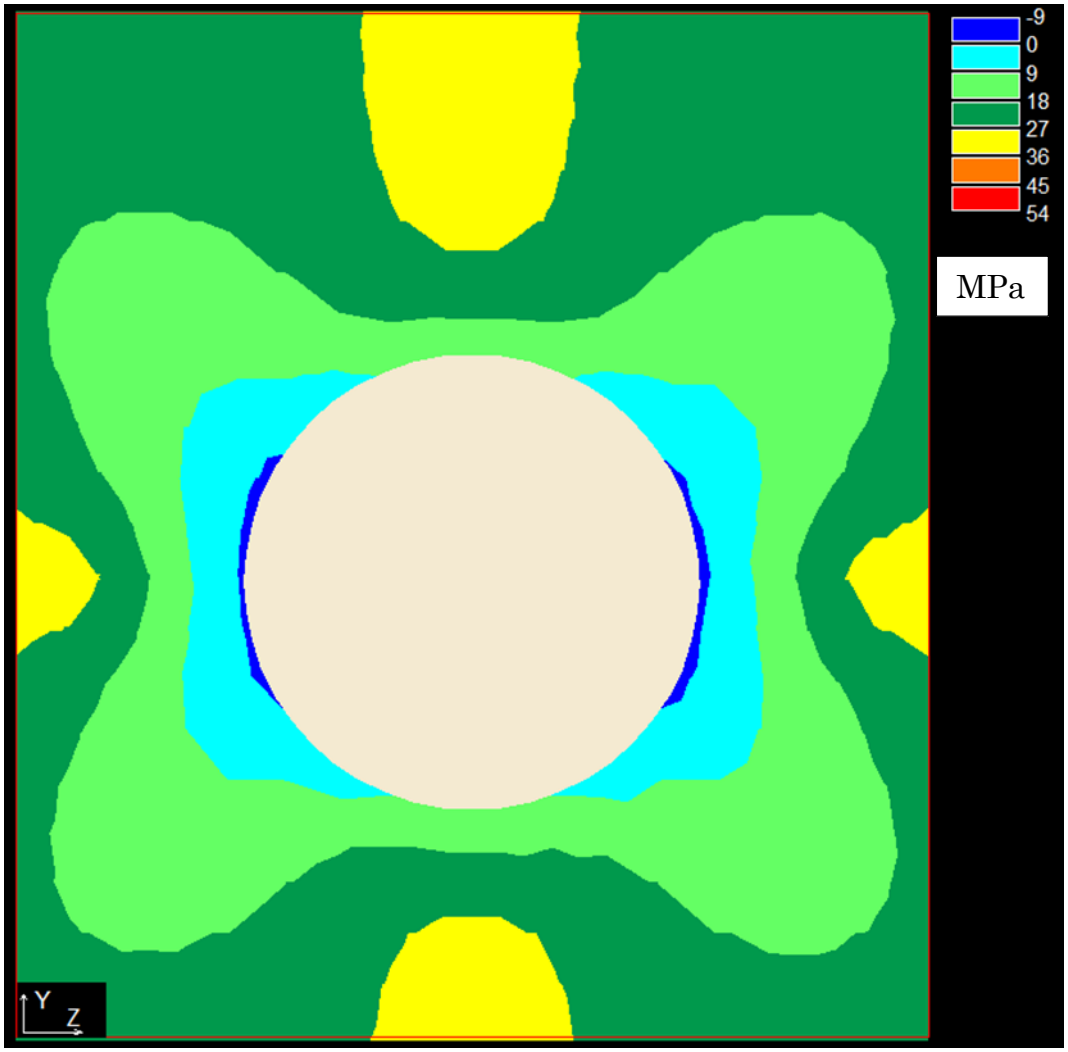


Figure 6.2.13: Front view of cutting plane depicting σ3 distribution through a section of an eight-metre diameter tunnel (σx= 52.5 MPa, σy= 25 MPa, σz= 70 MPa).

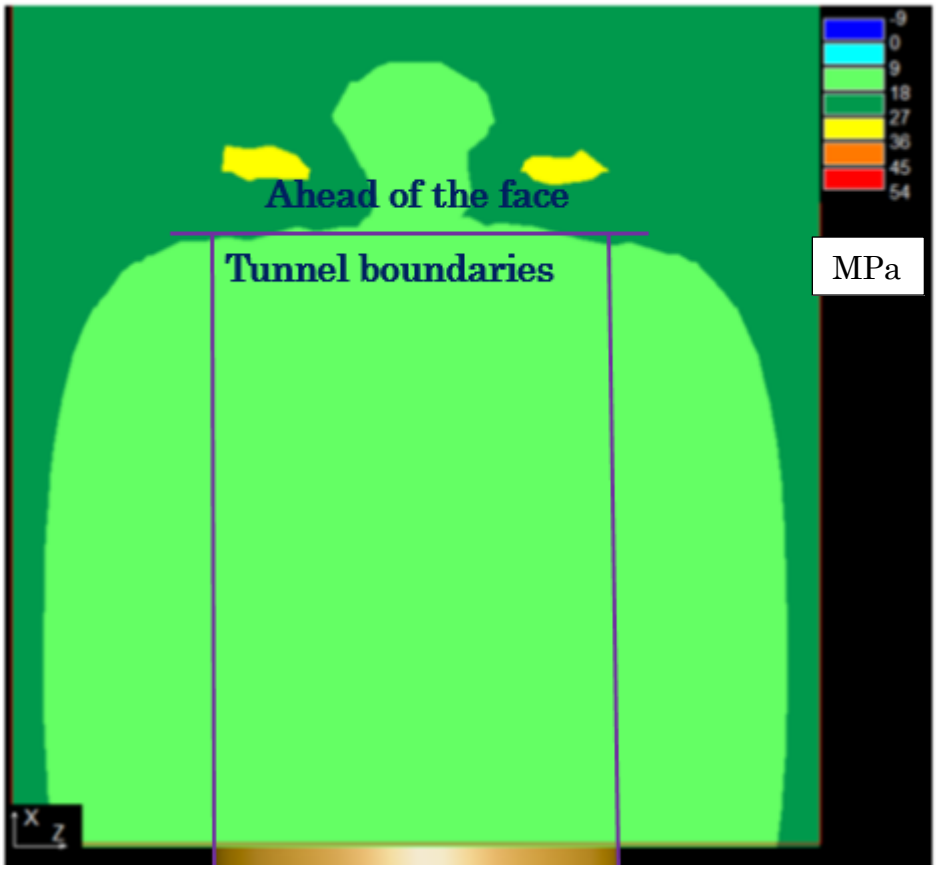


Figure 6.2.14: Top view of cutting plane depicting σ3 distribution through the roof of an eight-metre diameter tunnel (σx= 52.5 MPa, σy= 25 MPa, σz= 70 MPa).

6.2.4 Analyses results for an eight-metre diameter tunnel (σx= 35 MPa, σy= 17.5 MPa, σz= 52.5 MPa)

Figure 6.2.15 and Figure 6.2.16 show major principal stress (σ1) distribution contour plots. It can be seen in Figure 6.2.15 that the high stress concentrations are exhibited at tunnel hangingwall and footwall, ranging from 100 MPa to 150 MPa, with sidewalls showing a sign of de-stressing. Figure 6.2.17 and Figure 6.2.18 show the minor principal stress (σ3) distribution contour plots. It can be noted in Figure 6.2.18 that σ3 values show a slight tension on the sidewalls, with the maximum value of 6 MPa.

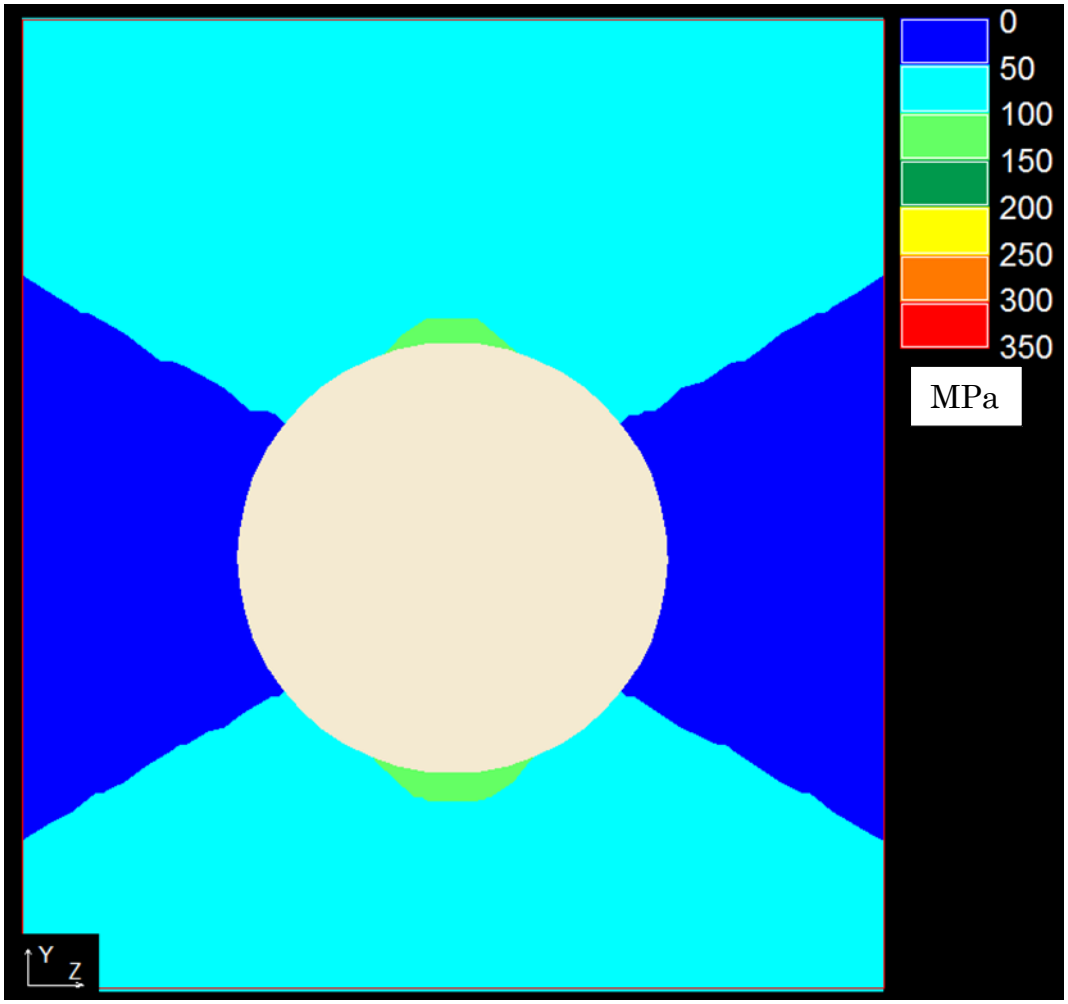


Figure 6.2.15: Front view of cutting plane depicting σ1 distribution through a section of an eight-metre diameter tunnel (σx= 35 MPa, σy= 17.5 MPa, σz= 52.5 MPa).

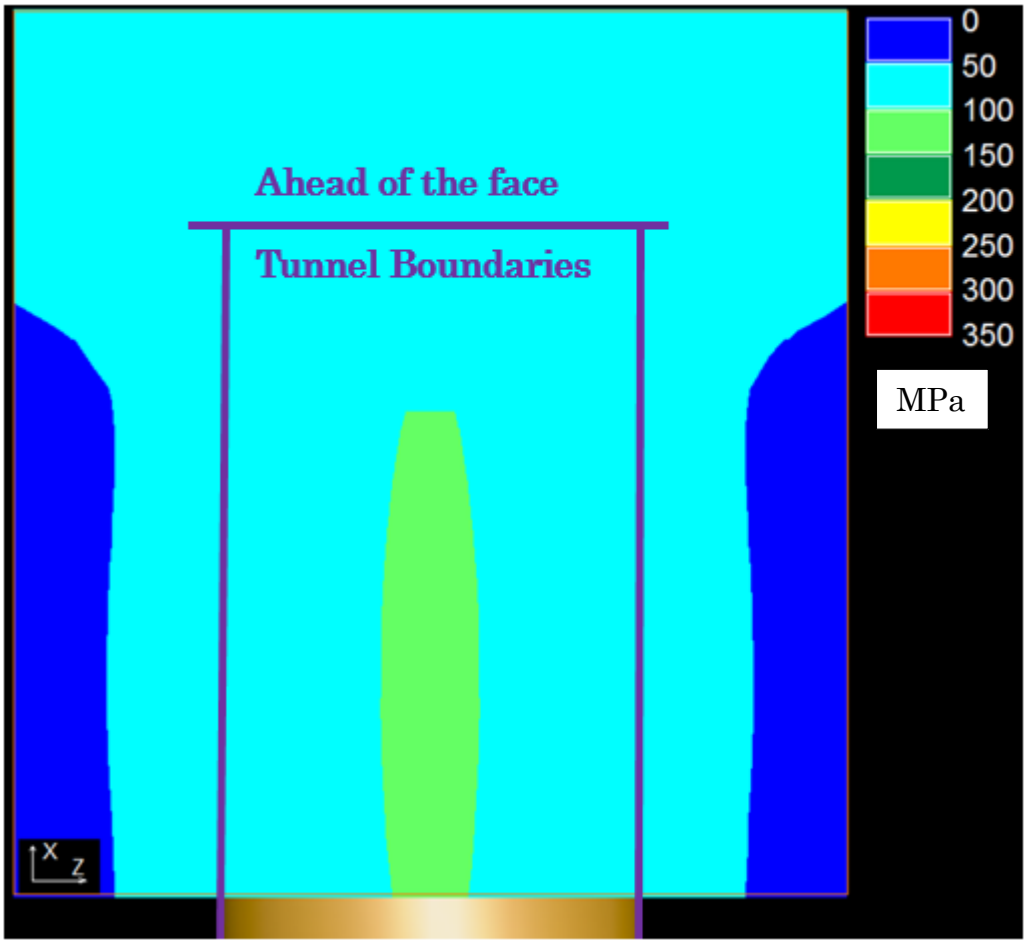


Figure 6.2.16: Top view of cutting plane depicting σ1 distribution through the roof of an eight-metre diameter tunnel (σx= 35 MPa, σy= 17.5 MPa, σz= 52.5 MPa).

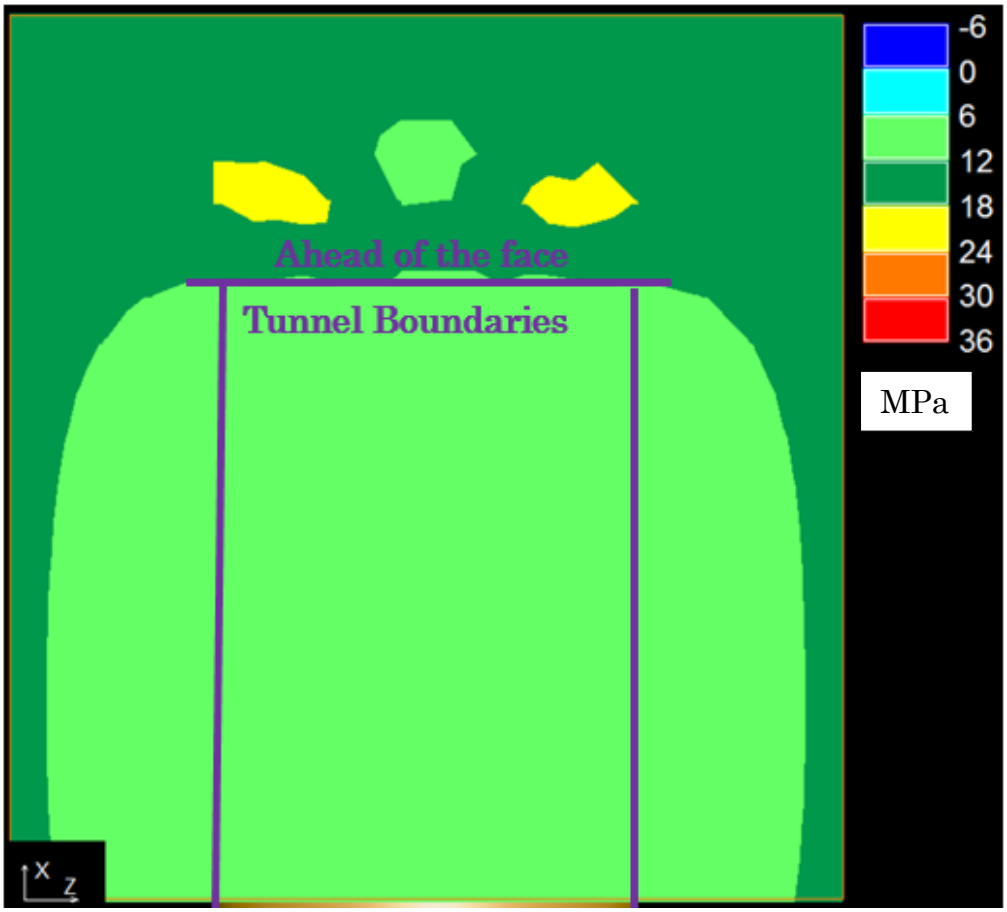


Figure 6.2.17: Top view of cutting plane depicting σ3 distribution through the roof of an eight-metre diameter tunnel (σx= 35 MPa, σy= 17.5 MPa, σz= 52.5 MPa).

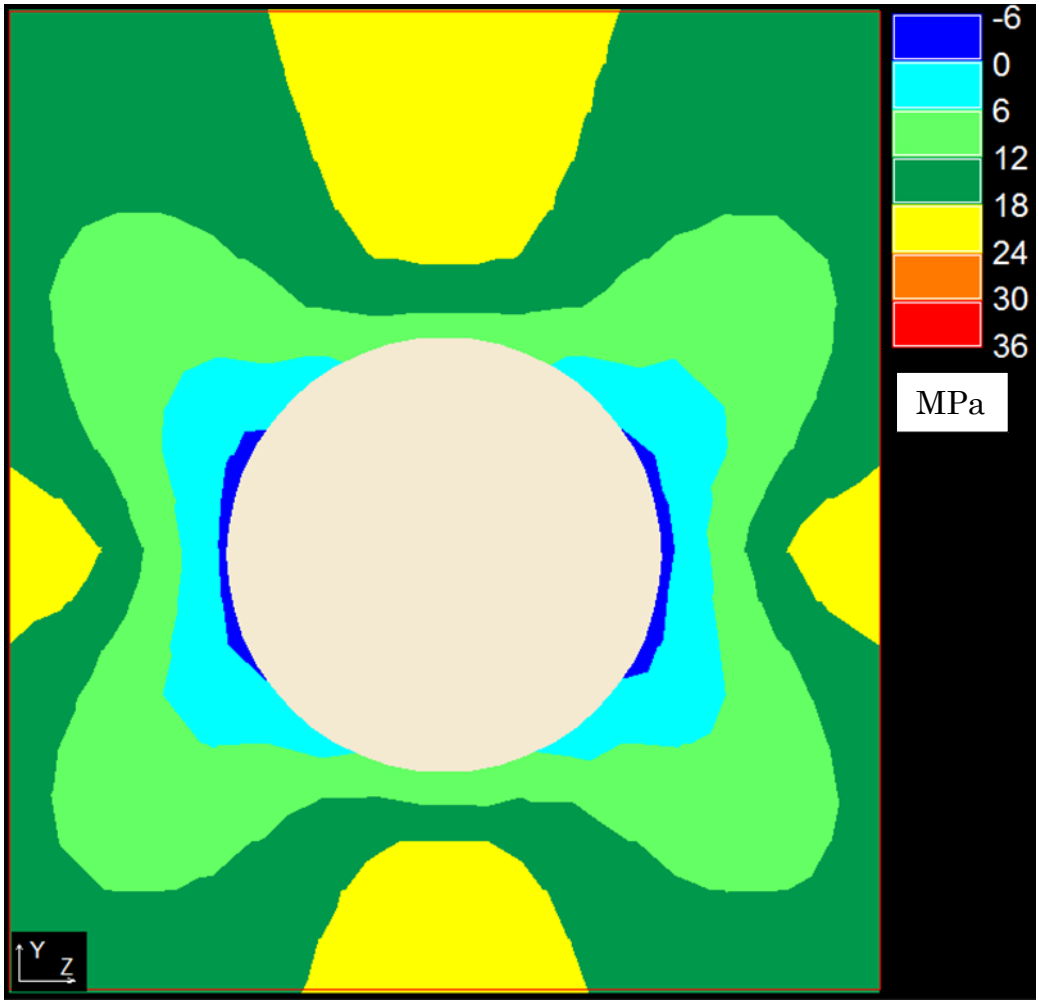


Figure 6.2.18: Front view of cutting plane depicting σ3 distribution through a section of an eight-metre diameter tunnel (σx= 35 MPa, σy= 17.5 MPa, σz= 52.5 MPa).

6.2.5 Analyses results for an eight-meter diameter tunnel (σx= 52.5 MPa, σy= 70 MPa, σz= 25 MPa)

Figure 6.2.19 and Figure 6.2.20 show major principal stress (σ1) distribution contour plots. It can be noted in Figure 6.2.20 that the high stress concentrations are exhibited at tunnel sidewalls, ranging from 100 MPa to 150 MPa, with hangingwall and footwall showing a sign of de-stressing. Figure 6.2.21 and Figure 6.2.22 show the minor principal stress (σ3) distribution contour plots. It can be seen in Figure

6.2.22 that σ3 values turn to tension on the hangingwall and footwall due to high values of the vertical stresses.

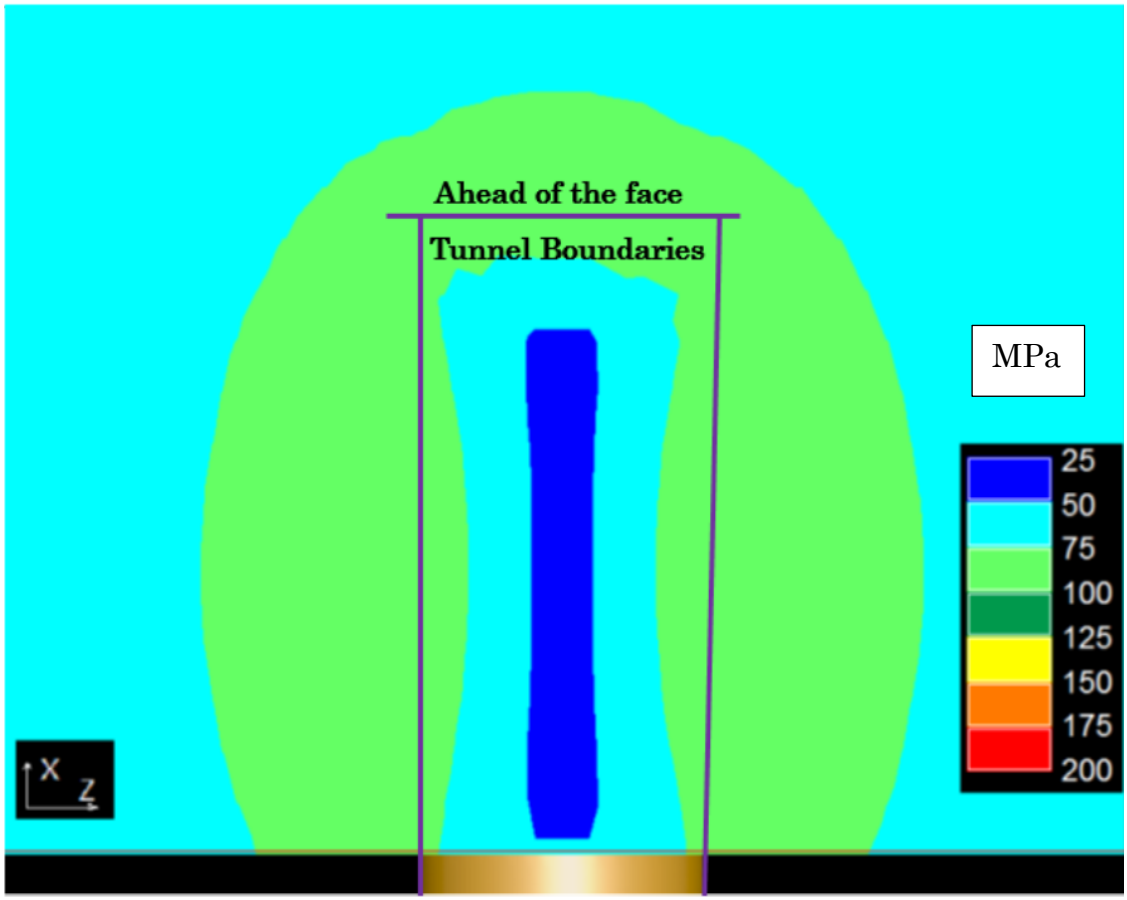


Figure 6.2.19: Top view of cutting plane depicting σ1 distribution through a section of an eight-metre diameter tunnel (σx= 52.5 MPa, σy= 70 MPa, σz= 25 MPa).

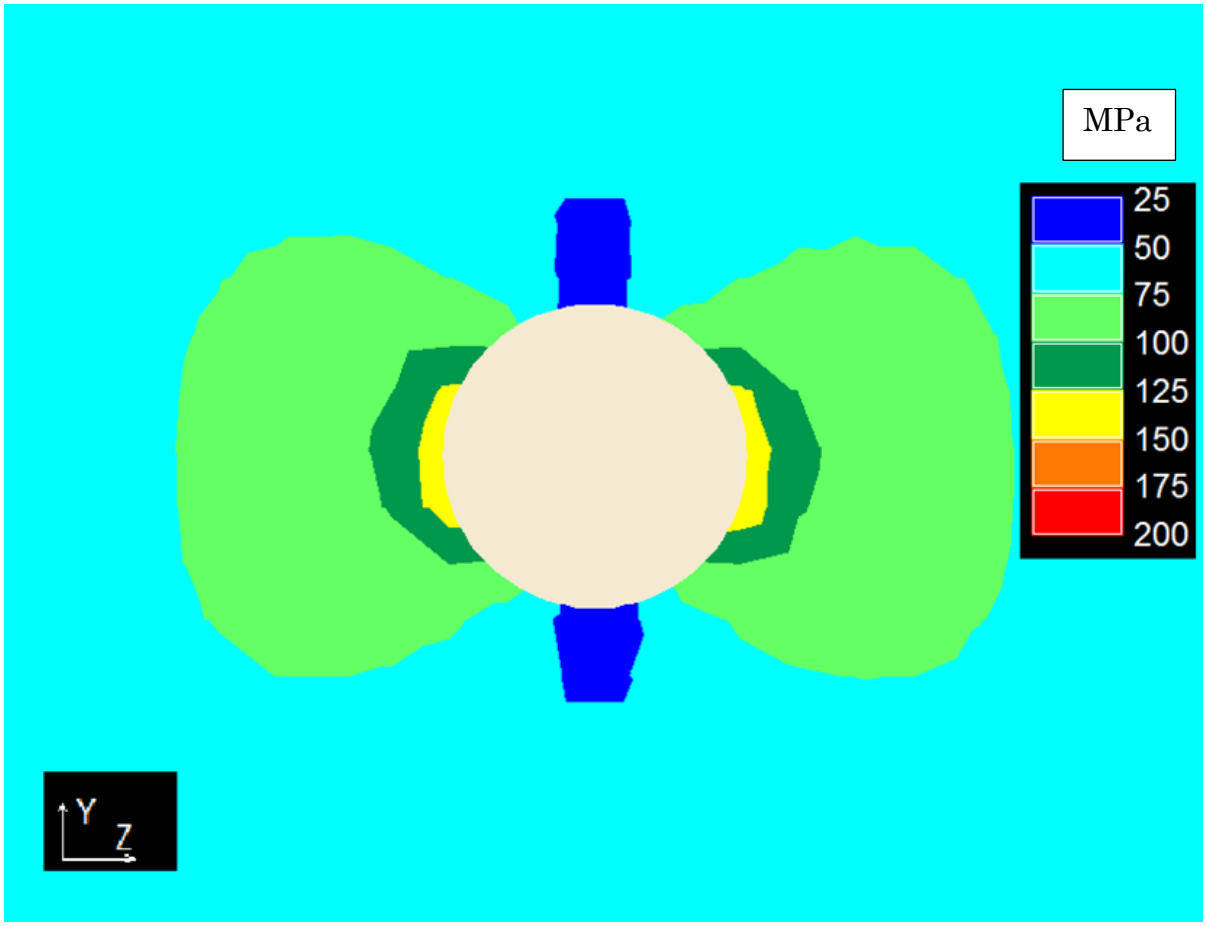


Figure 6.2.20: Front view of cutting plane depicting σ1 distribution through a section of an eight-metre diameter tunnel (σx= 52.5 MPa, σy= 70 MPa, σz= 25 MPa).

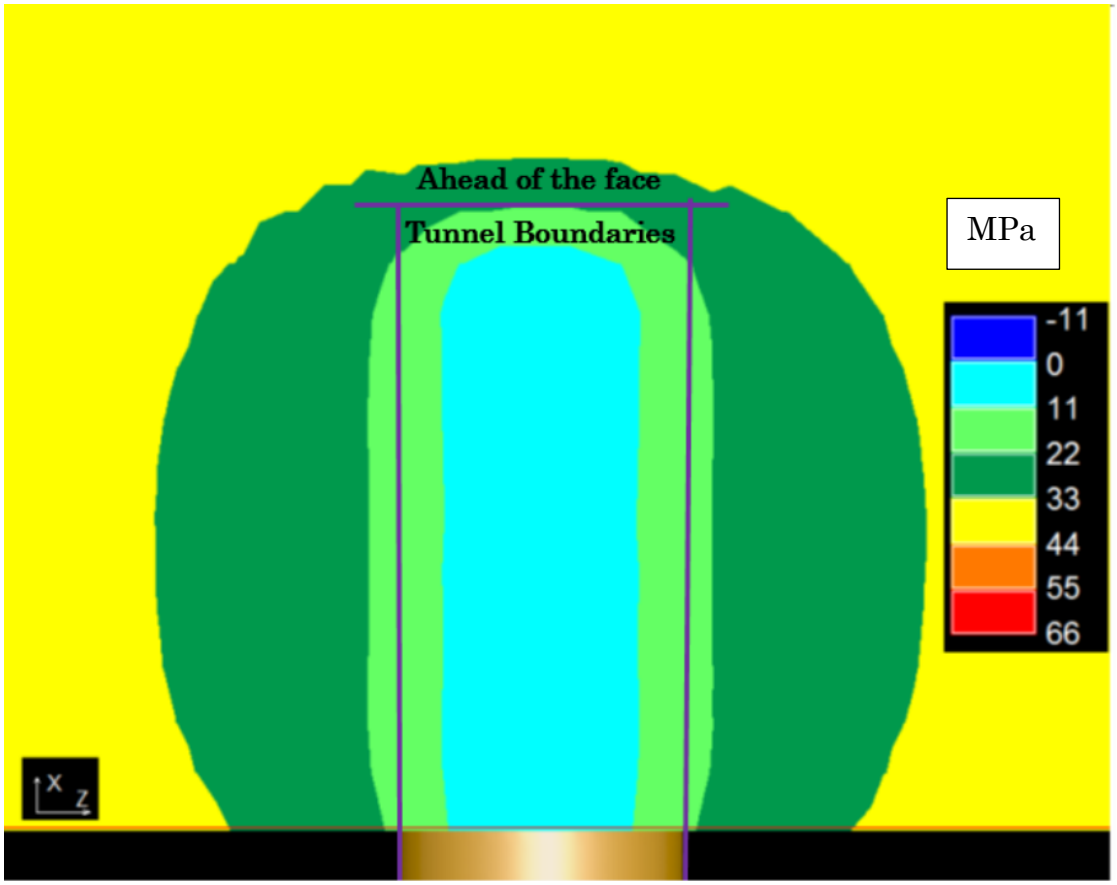


Figure 6.2.21: Top view of cutting plane depicting σ3 distribution through a section of an eight-metre diameter tunnel (σx= 52.5, MPa, σy= 70 MPa, σz= 25 MPa).

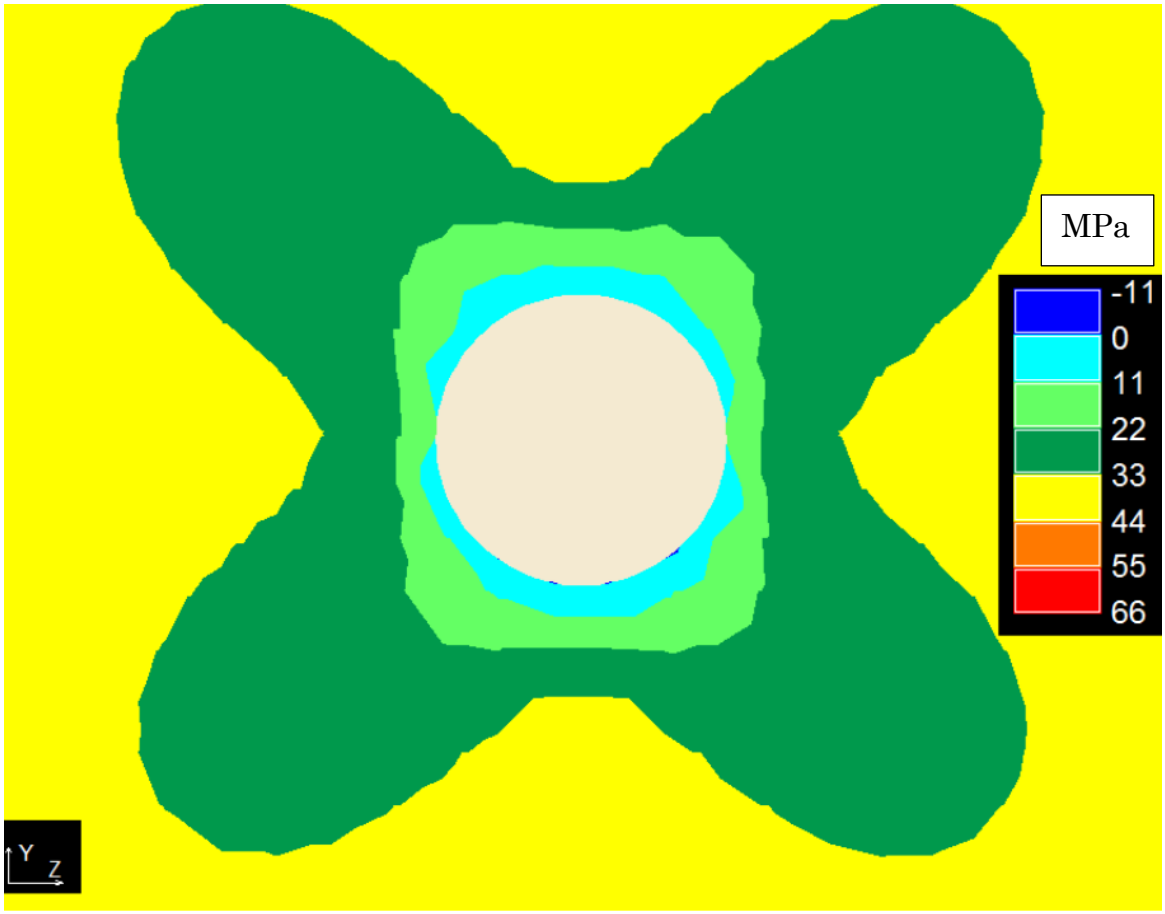


Figure 6.2.22: Front view of cutting plane depicting σ3 distribution through a section of an eight-metre diameter tunnel (σx= 52.5 MPa, σy= 70 MPa, σz= 25 MPa).

6.2.6 Summary of the results

For ratio of the average horizontal stress to the vertical stress (k ratio) greater than or equal to one, the stress concentration tends to be high at the tunnel hangingwalls and footwalls, with the sidewalls undergoing tensile stress. Whereas, k ratios less than one, stress is concentrated mainly on the sidewalls of the tunnels. The principal stress distribution depends on the in situ stress ratios, which determine the extent of fracturing that develops ahead and on the walls of the tunnels. This can be seen in Figure 6.4.6 to Figure 6.4.11.

The similar results can be observed for two metre, four-metre and six-metre diameter-tunnels.

6.3 **Predicted Zone of Extension**

The results of the potential zone of fracture were generated by using extension strain criterion. The critical extension strains ranging from 180 to 270 microstrain for crack initiation and from 504 to 864 microstrain for the crack damage (failure), for the quartzite, were assumed (Wesseloo, 2000). A summary of results are shown in **Table** 6.3.1, depicting the failure depths of various tunnel sizes in relation to critical extension strains, Poisson's ratios and in situ stress ratios.

In an attempt to evaluate the relationship between the failure depths and the critical extension strains Figure 6.3.1 to Figure 6.3.4 were drawn. These are graphs depicting the sensitivity of the in situ stress ratios and the critical extension strains. It is worth noting that, for tunnels presented in these figures, fracture initiation does take place, whereas, the extent of failure is dependent on the tunnel size. Both crack initiation and crack failure points are indicated on the graphs. It can be noted that, the fractured zone is directly proportional to the tunnel diameter. For instance, in Figure 6.3.1, a fractured zone of 1.4 m is predicted for a six-metre tunnel at critical extension strain of 180 microstrain, under a stress condition $\sigma x/\sigma z = 0.7$, $\sigma y/\sigma z = 0.3$. Whereas, a fractured zone of about 1.6 m is predicted for an eight-metre diameter tunnel, as shown in Figure 6.3.2. It is worth noting that, at a critical extension strain of 504 microstrain, the fractured zones that will have an impact on boring are 150 mm and 400 mm for a six-metre diameter and eight-metre diameter tunnels, respectively. This implies that a six-metre diameter tunnel is less likely to cause boring problems than an eight-metre diameter tunnel.

Various isosurfaces, indicating potential extent of fracture locations ahead of the faces of the tunnels, are shown in Figure 6.3.5 to Figure 6.3.10. The isosurfaces were generated in such a way that, the surfaces

with similar values of critical strains were chosen, to define the extension surface. This was done for two different Poisson's ratios. Although the analyses were based on the material properties for quartzite, for other rock types the results will be regarded as a guide to the potential fracturing behaviour. From the results presented in **Table** 6.3.1, Figure 6.3.1 to Figure 6.3.10, it is apparent that:

- There are substantial zones of extension ahead of the tunnel faces and in the tunnel walls. These are zones of likely fracturing which could lead to boring or tunnelling problems. For instance, these fractured zones will cause tunnel faces to be advanced into fractured rocks, causing problems with boring head or cutters, and fractures in walls leading to potential instability of the walls.
- The distance of predicted fracture development ahead of the face of the tunnel is dependent on the relative magnitude of the principal stresses, as can be seen in Figure 6.3.6 and the Appendix in Figure 8.1.3 and Figure 8.1.4.
- The extent of the extension fracture zone ahead of the face, is dependent on the values of the Poisson's ratio. It is smaller for smaller values of Poisson's ratio, as can be seen in Figure 6.3.6 and Figure 6.3.9.

More plots concerning the results from the modelling software can be seen in the Appendix.

Table 6.3.1: Summary of in situ stresses, Poisson's ratio and predicted Failure Depth

	Poisson's ratio (v) = 0,2									
σx σy σz (MPa)	**70**	**35**	**70**			**σx σy σz (MPa)**	**35**	**17,5**	**52,5**	
	Tunnel Diameter(m)						Tunnel Diameter(m)			
	2	4	6	8			2	4	6	8
Critical Strain(εc) (microstrain)	Failure depth (m)					Critical Strain(εc) (microstrain)	Failure depth (m)			
180	0	0,5	1,6	2		180	0	0,9	1,4	1,6
260	0	0,3	1,2	1,5		260	0	0,5	1	1,3
340	0	0,2	0,9	1,1		340	0	0,1	0,7	0,9
420	0	0,1	0,5	0,7		420	0	0	0,4	0,5
500	0	0,05	0,2	0,4		500	0	0	0,05	0,2
580	0	0,01	0,05	0,05		580	0	0	0,01	0,05
	Poisson's ratio (v)= 0,3							**v= 0,3**		
σx σy σz (MPa)	**70**	**35**	**70**			**σx σy σz (MPa)**	**35**	**17,5**	**52,5**	
Tunnel Diameter(m)						Tunnel Diameter(m)				
	2	4	6	8			2	4	6	8
Critical Strain(εc)(microstrain)	Failure depth (m)					Critical Strain(εc)(microstrain)	Failure depth (m)			
270	1	1,7	3,2	4,2		270	0,9	1,2	2,2	3,2
370	0,5	1,2	2,4	3,2		370	0,3	1	1,6	2,4
470	0,1	0,9	1,8	2,2		470	0	0,8	1,2	1,8
570	0	0,5	1,1	1,8		570	0	0,4	0,7	1
670	0	0,2	0,7	1,1		670	0	0	0,4	0,8
770	0	0,08	0,3	0,9		770	0	0	0,2	0,4
870	0	0,01	0,08	0,5		870	0	0	0,05	0,1
	Poisson's ratio (v)= 0,2							**v= 0,2**		
σx σy σz (MPa)		**35**	**35**	**70**		**σx σy σz (MPa)**		**52,5**	**25**	**70**
Tunnel Diameter(m)						Tunnel Diameter(m)				
	2	4	6	8			2	4	6	8
Critical Strain(εc) (microstrain)	Failure depth (m)					Critical Strain(εc) (microstrain)	Failure depth (m)			
180	0	1	1,8	2,3		180	0,5	1,3	1,7	2,4
260	0	0,6	1,4	1,9		260	0	1,1	1,3	2
340	0	0,3	1,1	1,3		340	0	0,8	1	1,6
420	0	0,1	0,8	0,9		420	0	0,4	0,6	1,2
500	0	0	0,5	0,5		500	0	0,1	0,3	0,7
580	0	0	0,2	0,2		580	0	0	0,1	0,4
	Poisson's ratio (v)= 0,3							**v= 0,3**		
σx σy σz (MPa)		**35**	**35**	**70**		**σx σy σz (MPa)**		**52,5**	**25**	**70**
Tunnel Diameter(m)						Tunnel Diameter(m)				
	2	4	6	8			2	4	6	8
Critical Strain(εc)(microstrain)	Failure depth (m)					Critical Strain(εc)(microstrain)	Failure depth (m)			
270	0,5	1,2	2,6	3,5		270	1,5	3	4,3	6
370	0	0,8	2	2,9		370	1	1,9	3,1	5,1
470	0	0,5	1,6	2		470	0,4	1	2,5	4,2
570	0	0,2	1,1	1,6		570	0	0,6	1,9	3,1
670	0	0,05	0,7	0,9		670	0	0,3	1,2	2
770	0	0	0,2	0,4		770	0	0,06	0,5	1,3
870	0	0	0,05	0,1		870		0	0,1	0,8

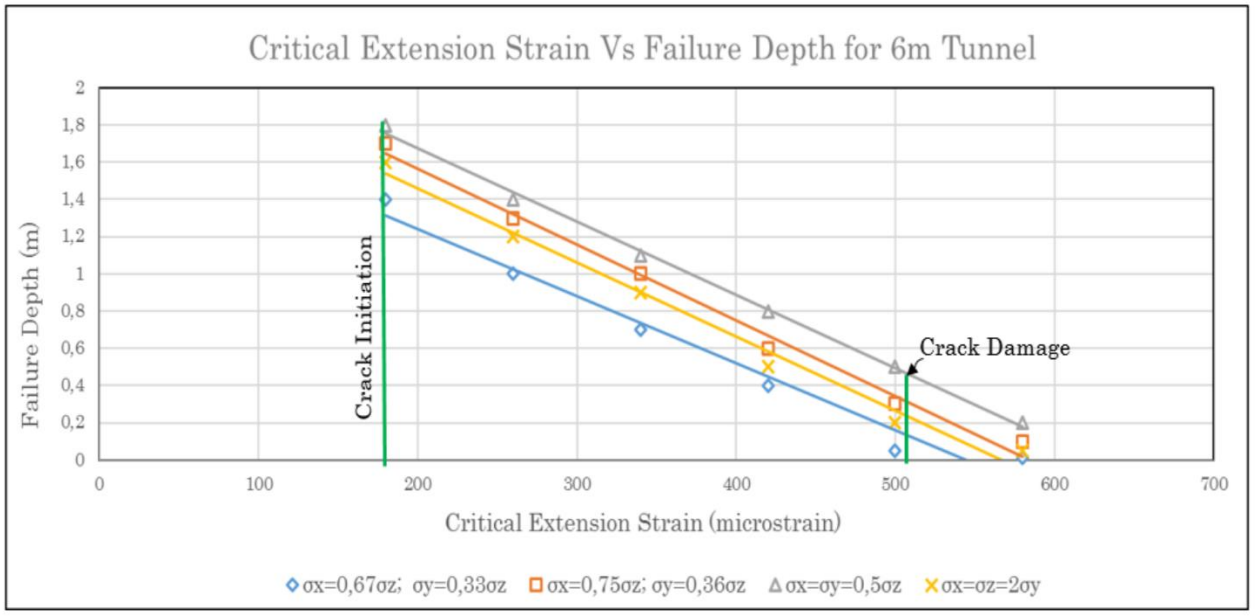


Figure 6.3.1: The predicted failure depth for different stress ratios for Poisson's ratio of 0.2.

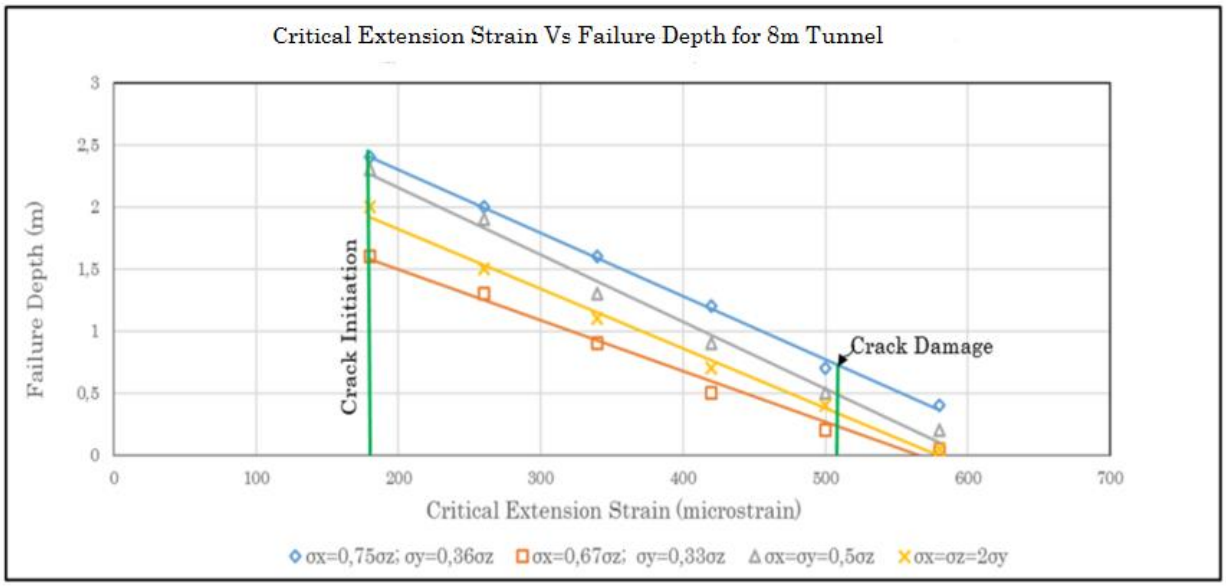


Figure 6.3.2: The predicted failure depth for different stress ratios for Poisson's ratio of 0.2.

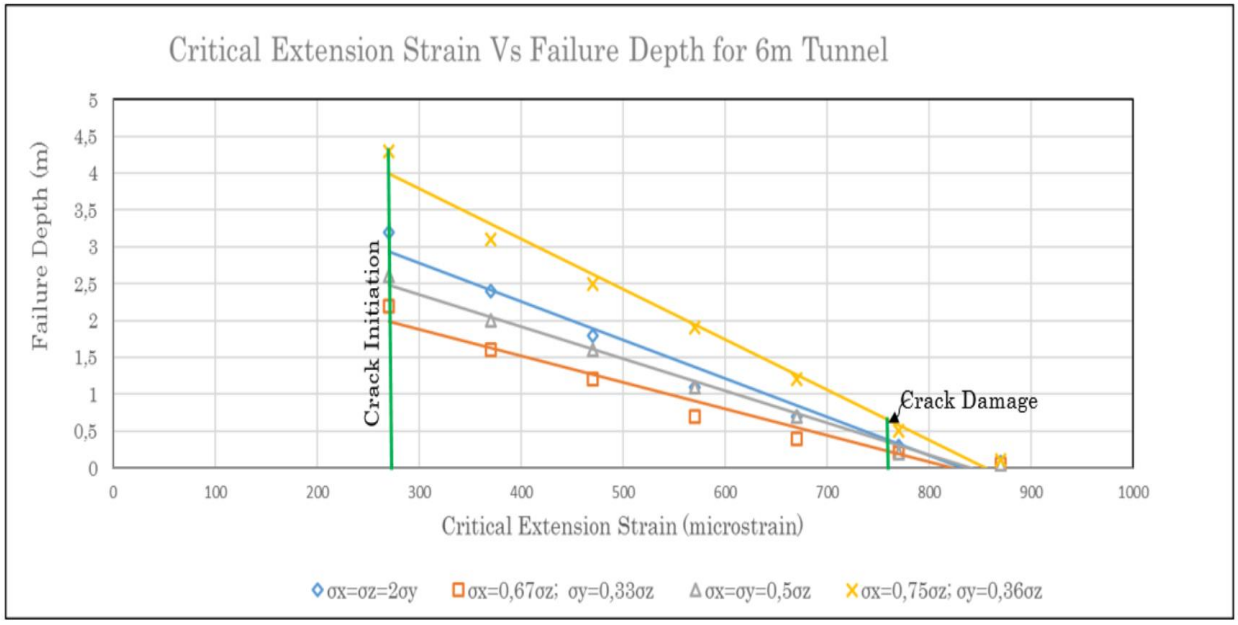


Figure 6.3.3 The predicted failure depth for different stress ratios for Poisson's ratio of 0.3.

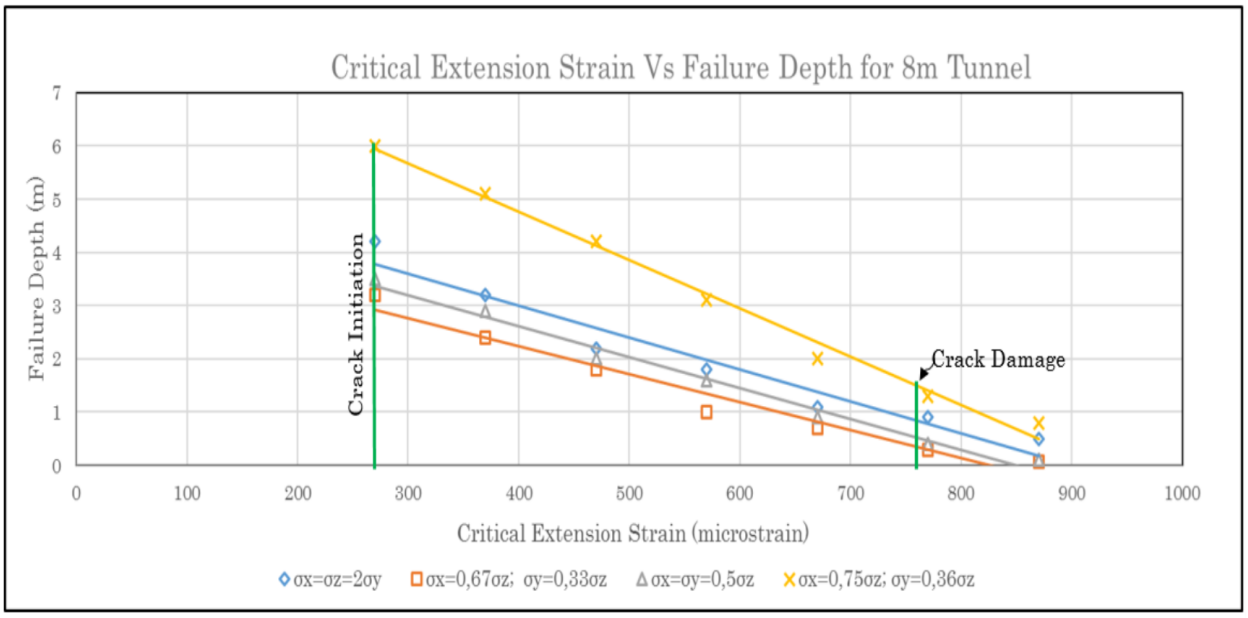


Figure 6.3.4: The predicted failure depth for different stress ratios for Poisson's ratio of 0.3.

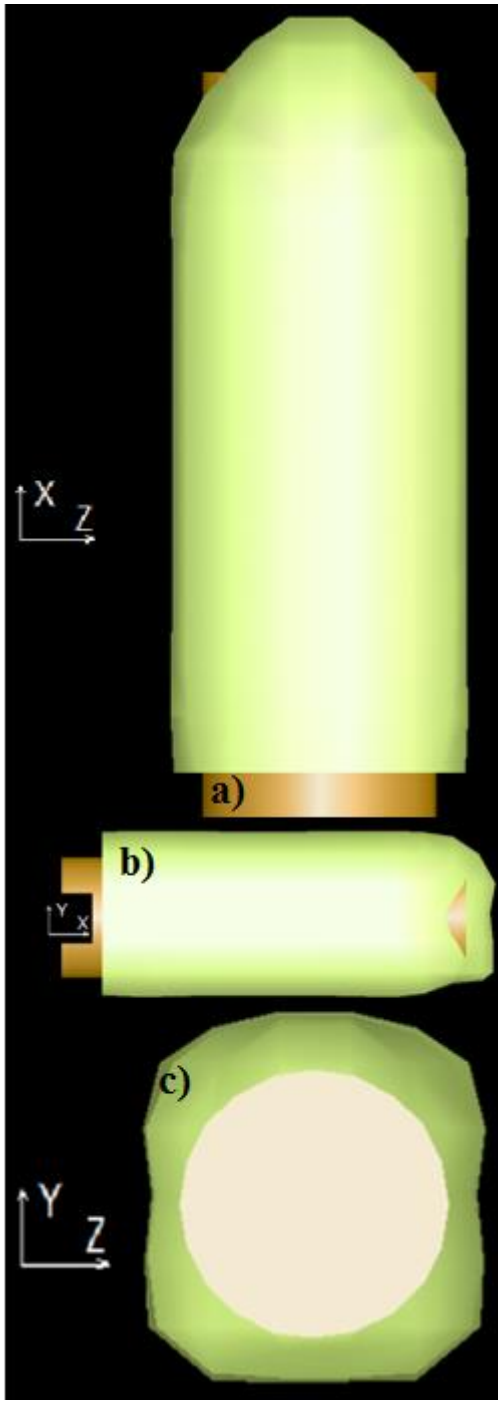


Figure 6.3.5: Isosurfaces of fracture/crack initiation for a six-metre diameter tunnel according to extension strain criterion for Poisson's ratio of 0.2 a) top view of the tunnel b) side view of the tunnel and c) frond view of the tunnel (σx= 70 σy= 35 σz= 70).

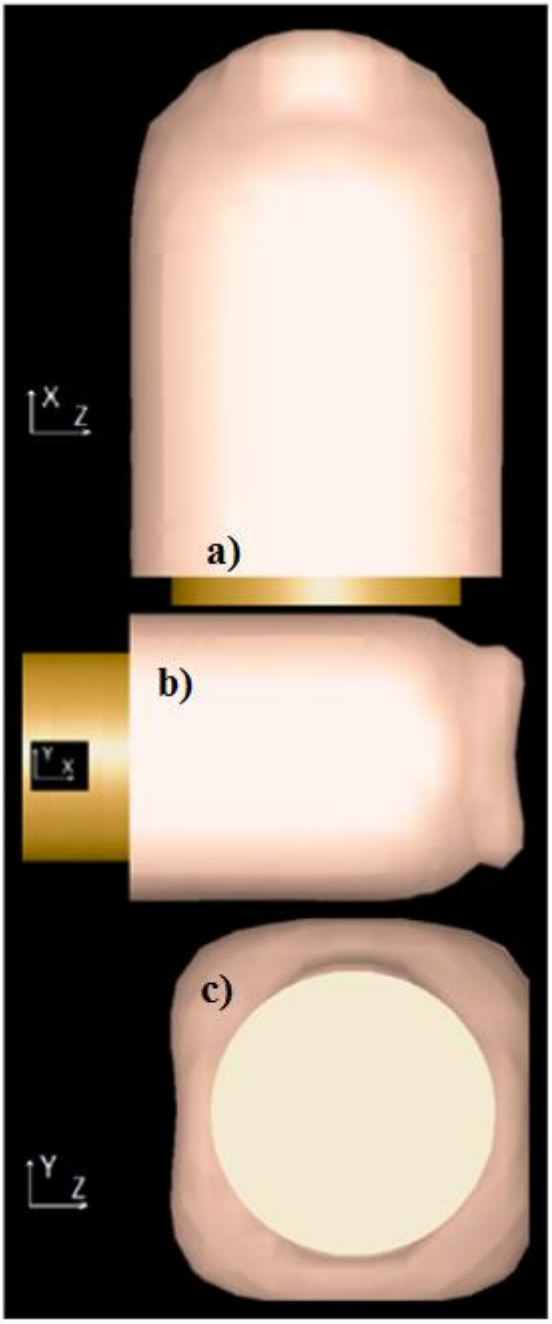


Figure 6.3.6: Isosurfaces of fracture/crack initiation for an eight-metre diameter tunnel according to extension strain criterion for Poisson's ratio of 0.2, a) top view of the tunnel b) side view of the tunnel c) front view of the tunnel (σx= 70 σy= 35 σz= 70).

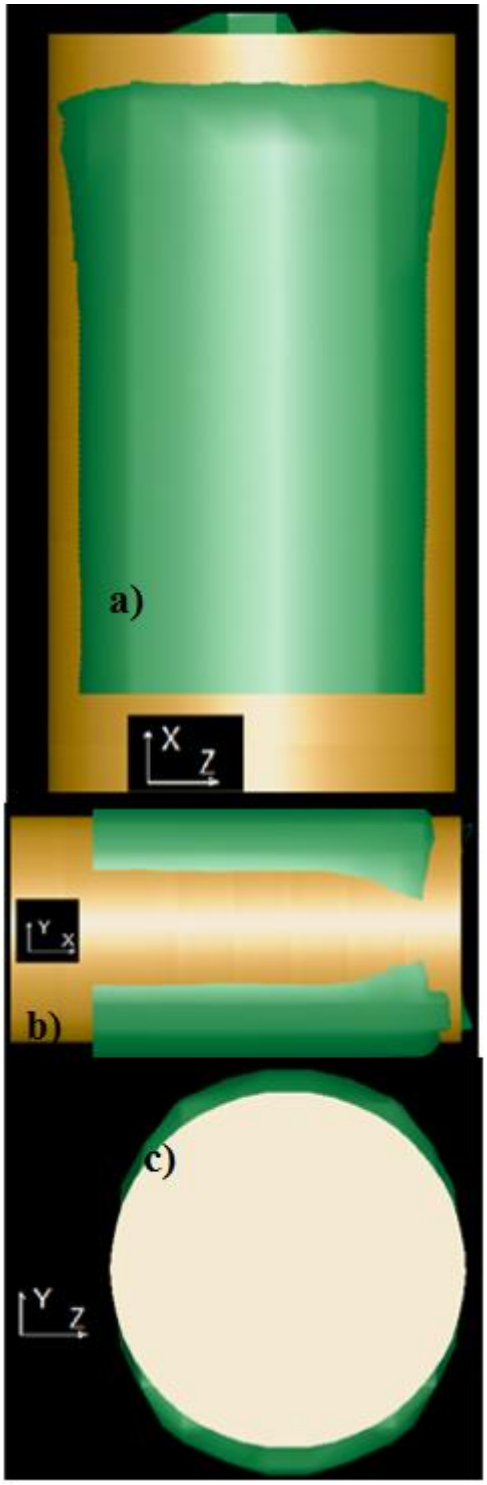


Figure 6.3.7: Isosurfaces of fracture/crack failure on an eight-metre diameter tunnel according to extension strain criterion for Poisson's ratio of 0.2, a) top view of the tunnel b) side view of the tunnel c) front view of the tunnel (σx= 70 σy= 35 σz= 70).

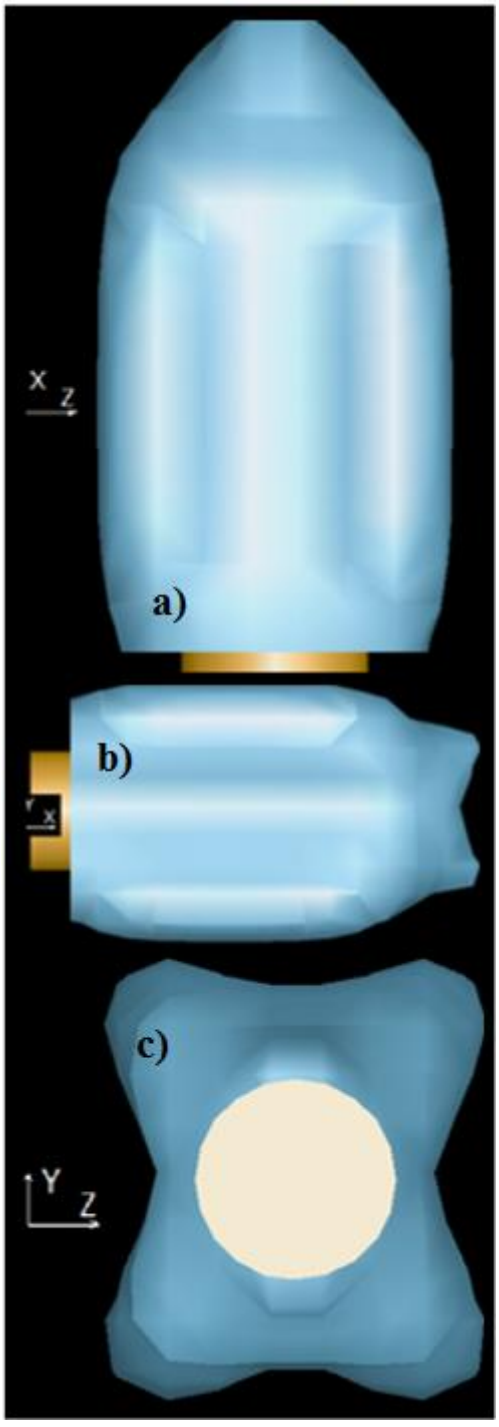


Figure 6.3.8: Isosurfaces of fracture/crack initiation for a six-metre diameter tunnel according to extension strain criterion for Poisson's ratio of 0.3, a) top view of the tunnel b) side view of the tunnel c) front view of the tunnel (σx= 70 σy= 35 σz= 70).

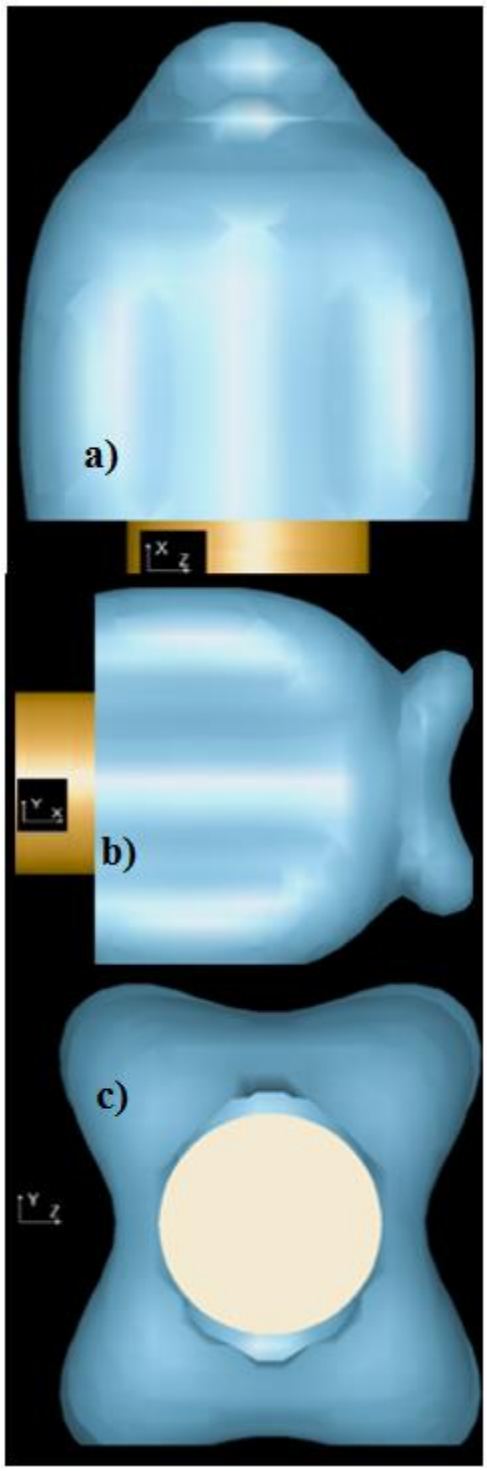


Figure 6.3.9: Isosurfaces of fracture/crack initiation for an eight-metre diameter tunnel according to extension strain criterion for Poisson's ratio of 0.3, a) top view of the tunnel b) side view of the tunnel c) front view of the tunnel (σx= 70 σy= 35 σz= 70).

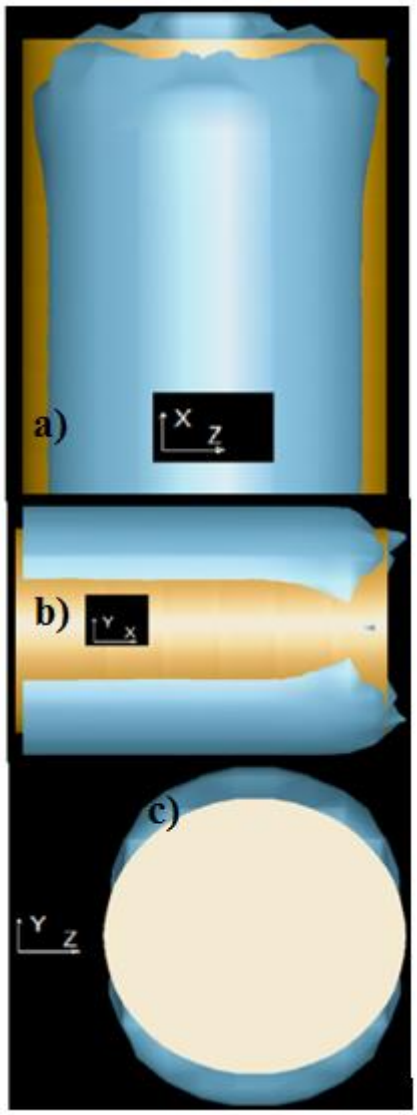


Figure 6.3.10: Isosurfaces of fracture/crack failure an eight-metre diameter tunnel according to extension strain criterion for Poisson's ratio of 0.3, a) top view of the tunnel b) side view of the tunnel c) front view of the tunnel (σx= 70 σy= 35 σz= 70).

6.4 **Orientation of Extension Fractures**

It has been learned from literature (chapter four, section 4.2) that the orientation of the extension fractures is normal to the direction of the minor principal stress. Using trajectory ribbons in Examine 3D, the three-dimensional variation of the orientation of three stresses (σ1, σ2, and σ3), can be displayed concurrently. They consist of “ribbons" passing through selected points, such that their orientations represent the principal stress directions. This is as follows: in the plane of the ribbon, the length dimension of the ribbon matches with the direction of the maximum principal stress (σ1); the width dimension matches with the direction of the intermediate principal stress (σ2); and the normal to the ribbon matches with the direction of the minimum compressive stress (σ3). Moreover, the trajectory ribbons are coloured to represent the magnitudes of the present stress component, according to the contour legend. Following the logic of the stress orientations, the ribbons depict the orientations of extension fractures across the predicted fractured zones. These are shown from Figure 6.4.1 to Figure 6.4.11 . These ribbons show the potential for slab, curved plate and shell geometries. Buckling of such geometries will result in the release of the energy stored in the “plate” due to the high stress levels. This release of energy will probably manifest as rockbursts.

It is worth noting that the orientations of fractures are dependent on the principal stress ratios. The behaviour of these fractures, relative to the advance of these tunnels, will depend on the orientation of the tunnel relative to that of the fractures, the tunnel size, and the stress magnitudes.

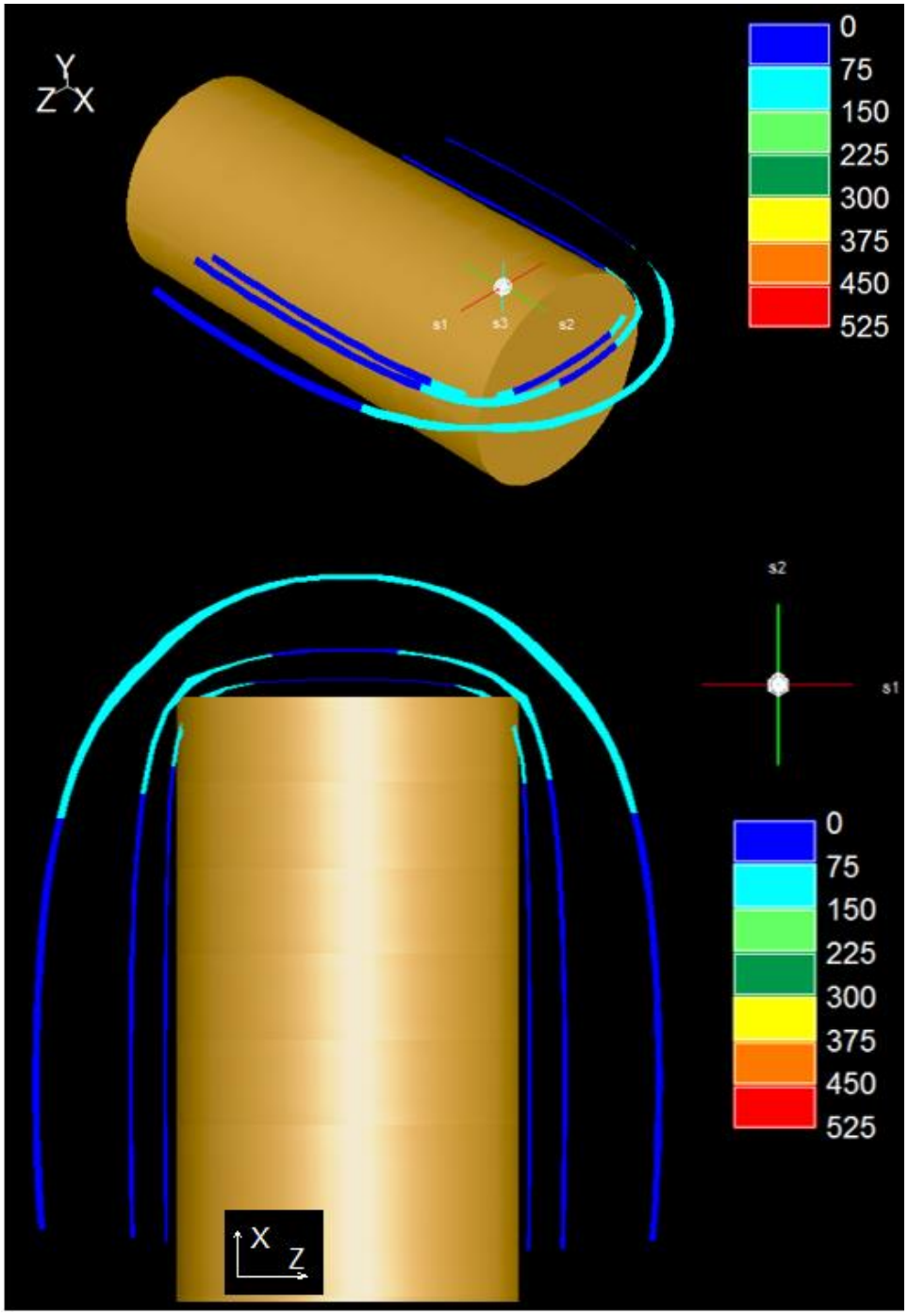


Figure 6.4.1: Orientations of fractures around an eight-metre diameter tunnel depicting σ1 values (σx= 70 MPa, σy= 35 MPa and σz= 70 MPa). Stress units above are MPa.

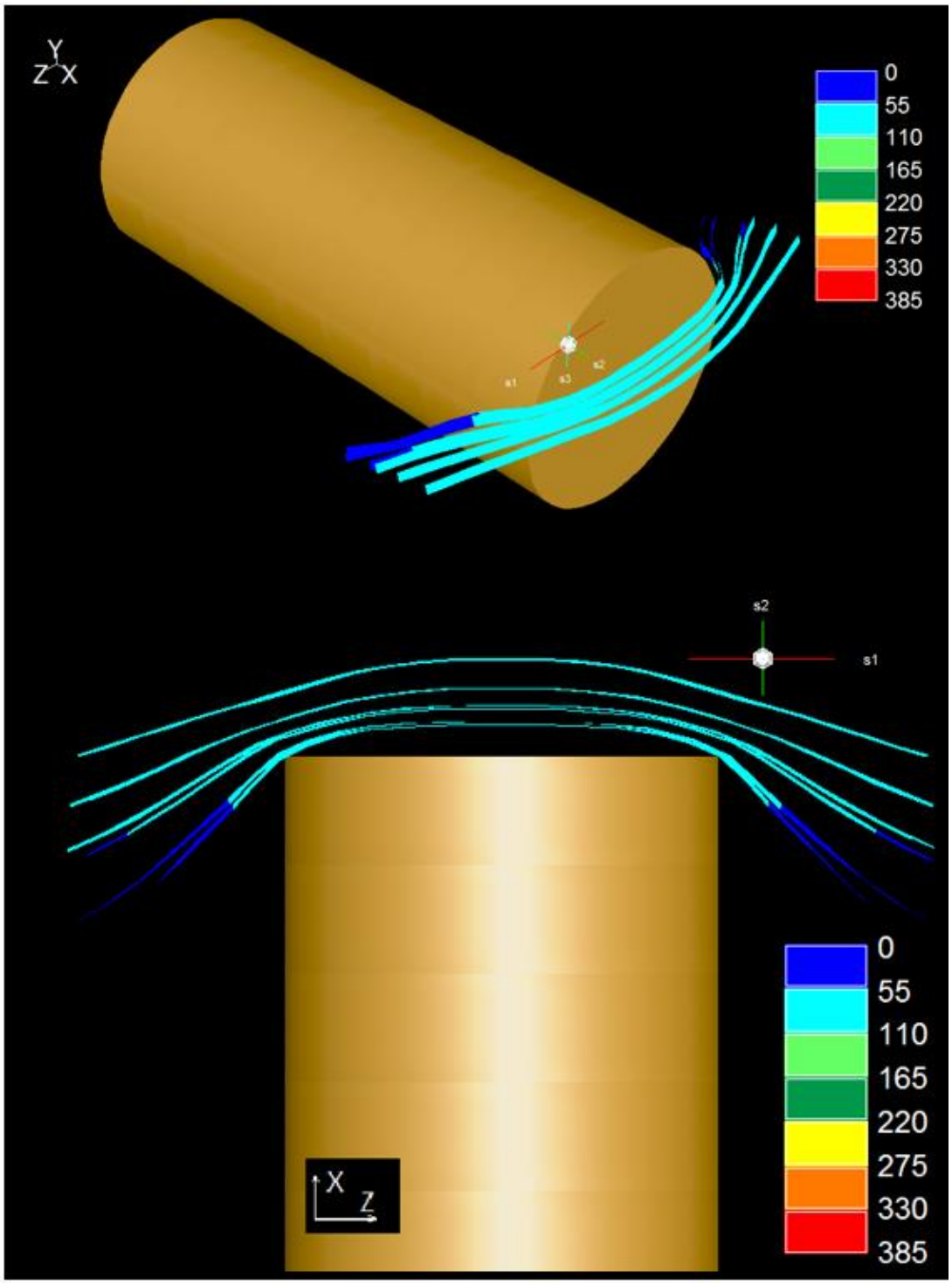


Figure 6.4.2: Orientations of fractures around an eight-metre diameter tunnel depicting σ1 values (σx= 35 MPa, σy= 35 MPa and σz= 70 MPa). Stress units above are MPa.

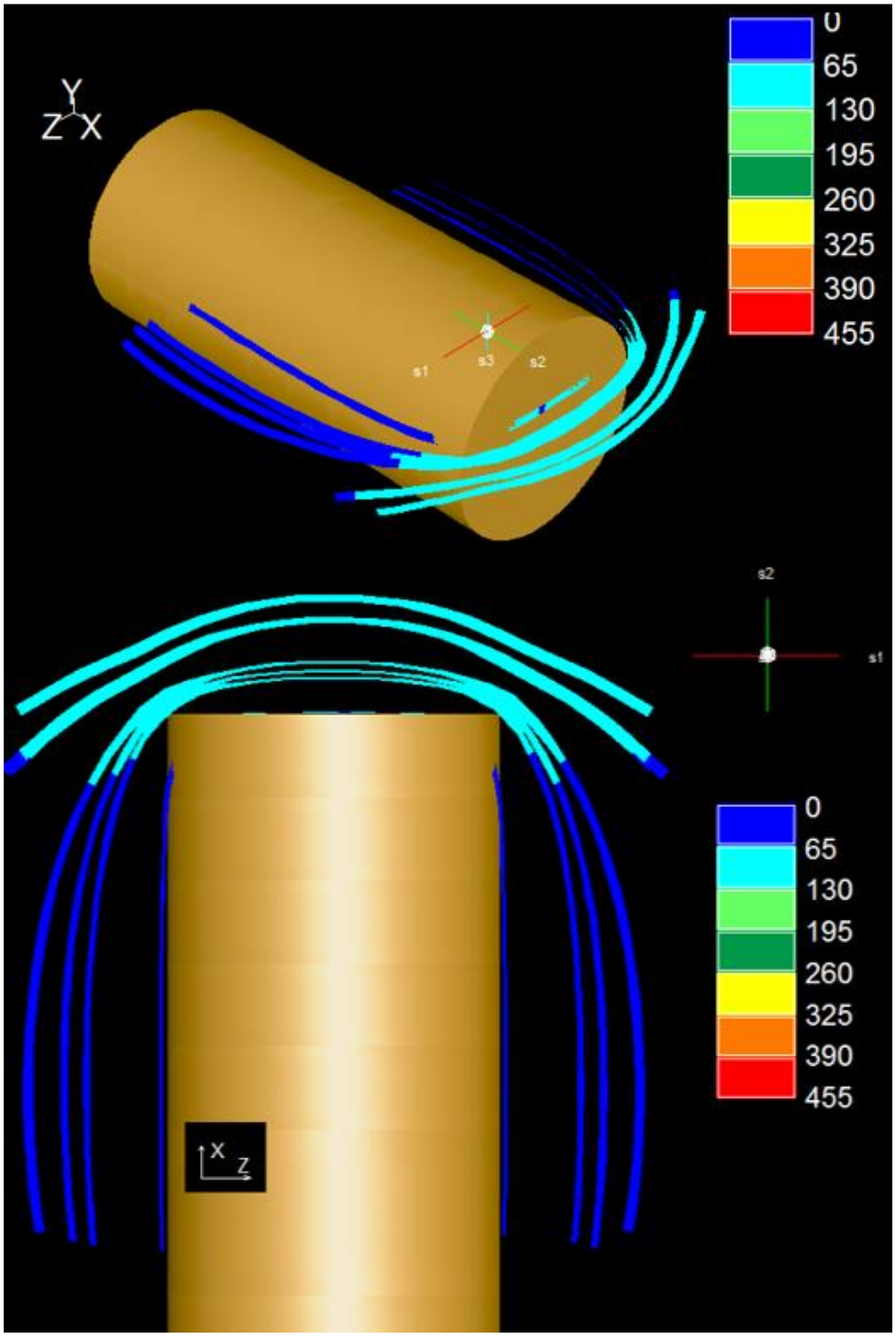


Figure 6.4.3: Orientations of fractures around an eight-metre diameter tunnel depicting σ1 values (σx= 52.5 MPa, σy= 25 MPa and σz= 70 MPa). Stress units above are MPa.

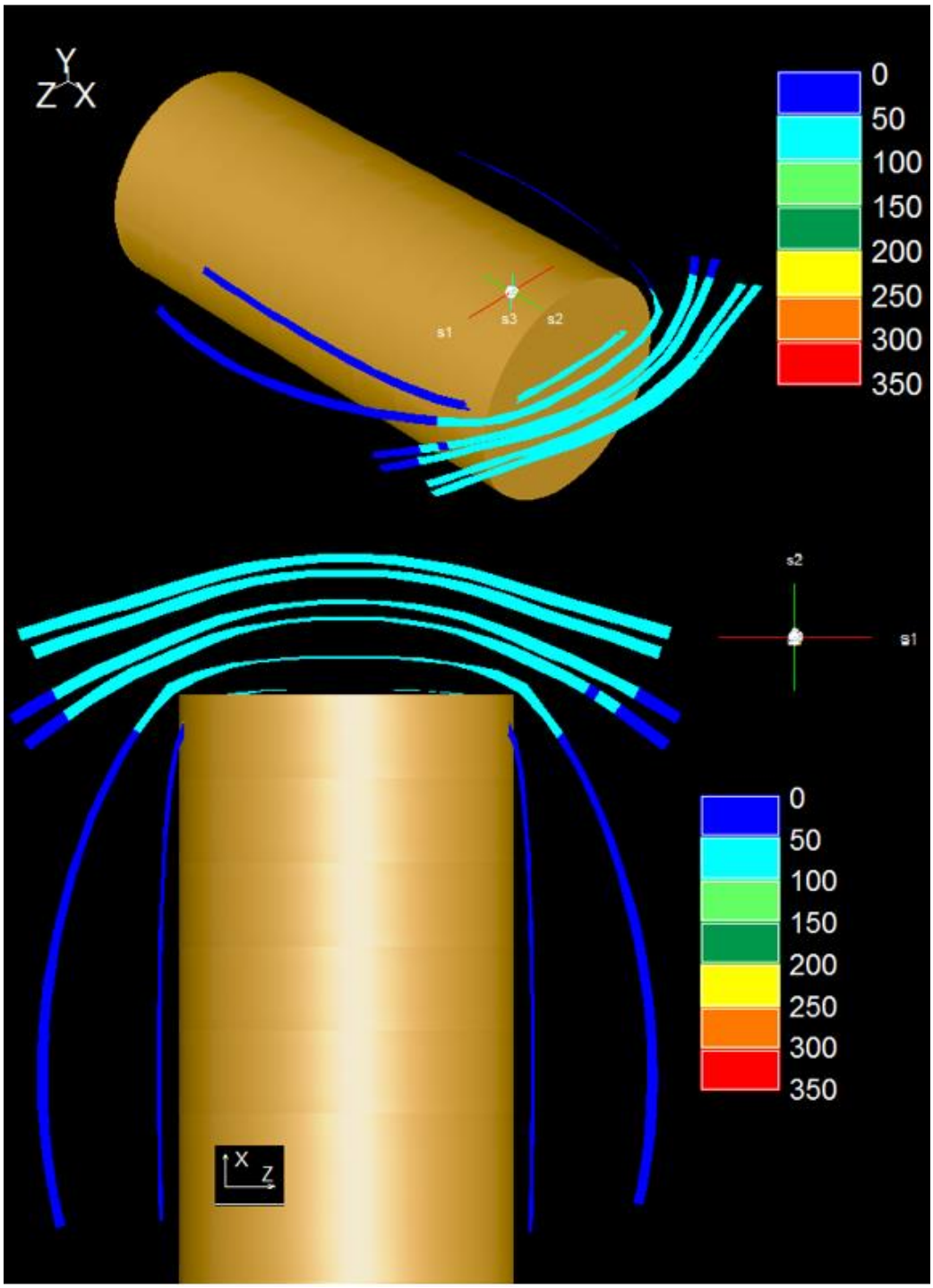


Figure 6.4.4: Orientations of fractures around an eight-metre diameter tunnel depicting σ1 values (σx= 35 MPa, σy= 17.5 MPa and σz= 52.5 MPa). Stress units above are MPa.

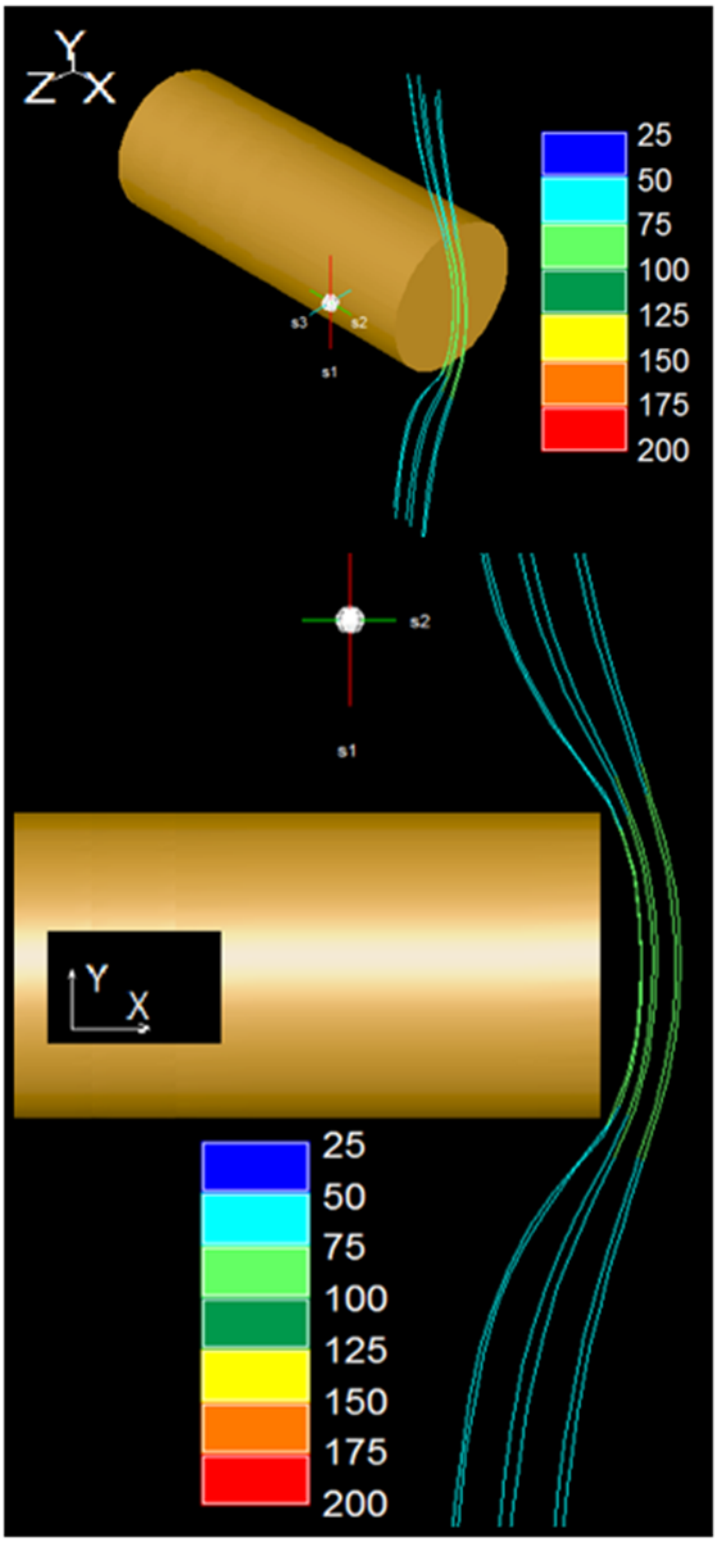


Figure 6.4.5: Orientations of fractures around an eight-metre diameter tunnel depicting σ1 values (σx= 35 MPa, σy= 70 MPa and σz= 35 MPa). Stress units above are MPa

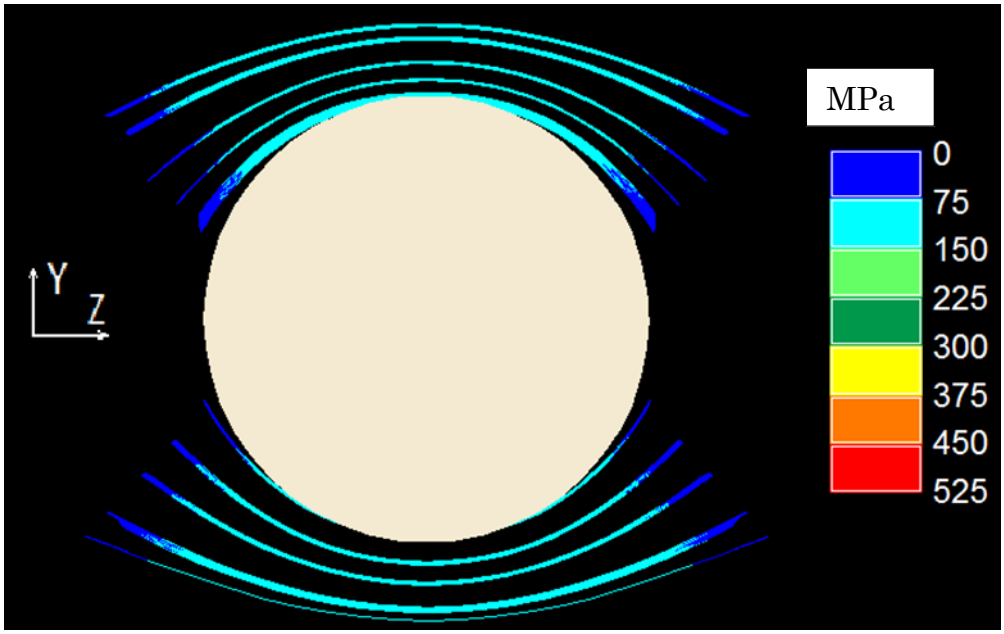


Figure 6.4.6: A vertical section across an eight-metre diameter tunnel depicting orientations of fractures on the footwall and hangingwall (σx= 70, σy= 35, σz= 70).

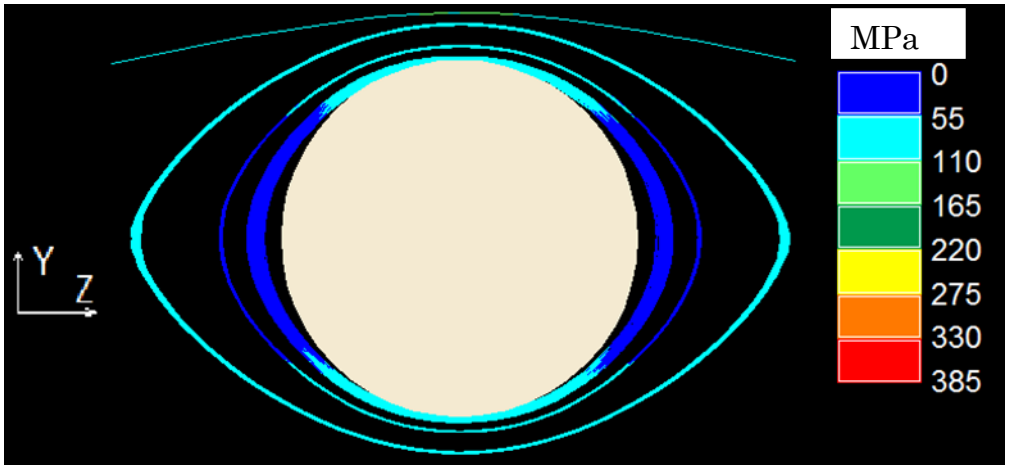


Figure 6.4.7: A vertical section across an eight-metre tunnel depicting orientations of fractures on the footwall and hangingwall (σx= 35 σy= 35, σz= 70)

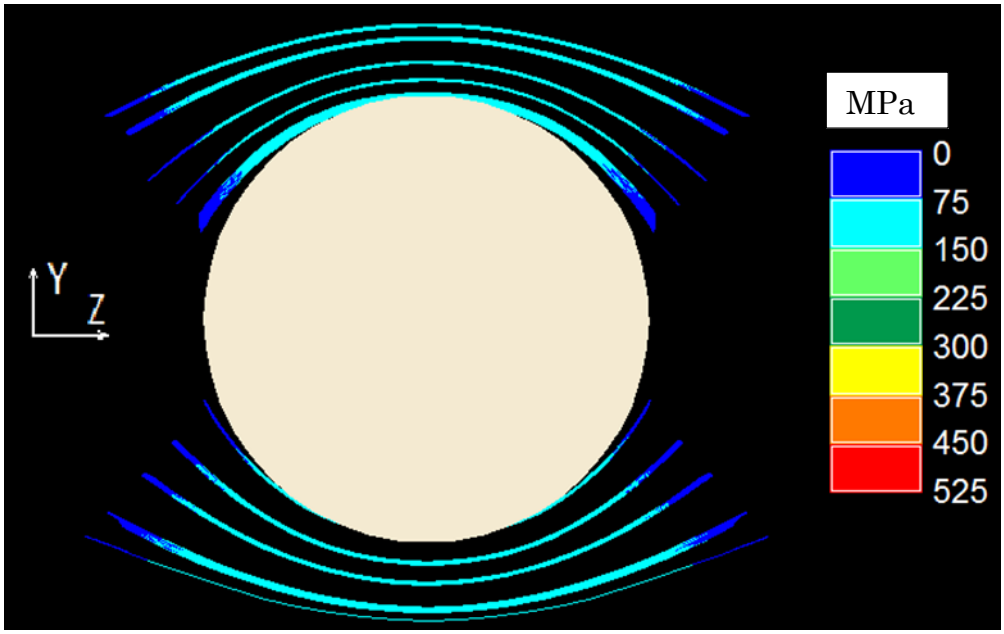


Figure 6.4.8: A vertical section across an eight-metre diameter tunnel depicting orientations of fractures on the footwall and hangingwall (σx= 52.5 σy= 25, σz= 70).

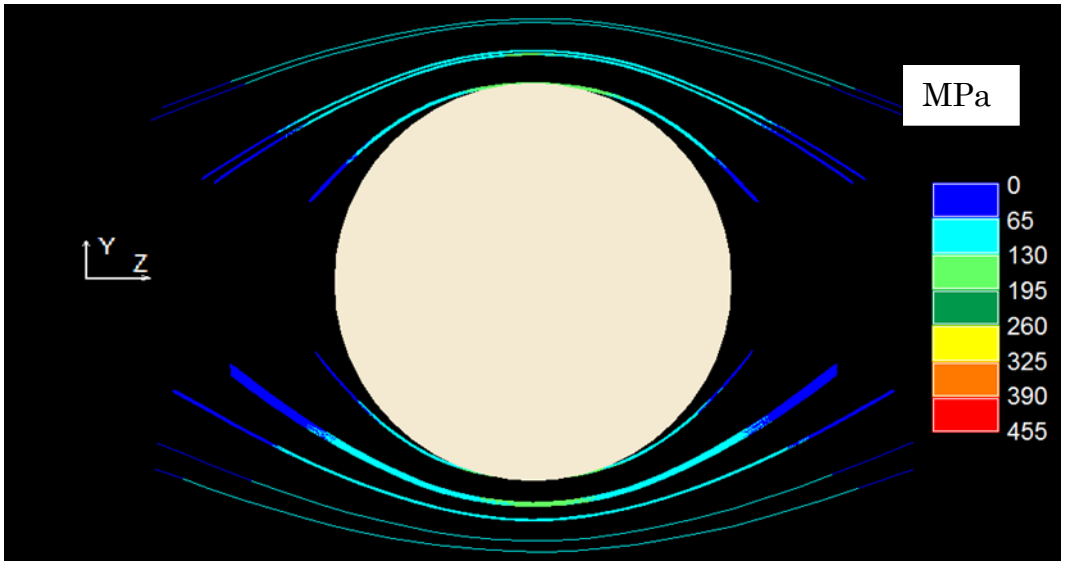


Figure 6.4.9: A vertical section across an eight-metre diameter +tunnel depicting orientations of fractures on the footwall and hangingwall (σx= 35 σy= 17.5, σz= 52.5).

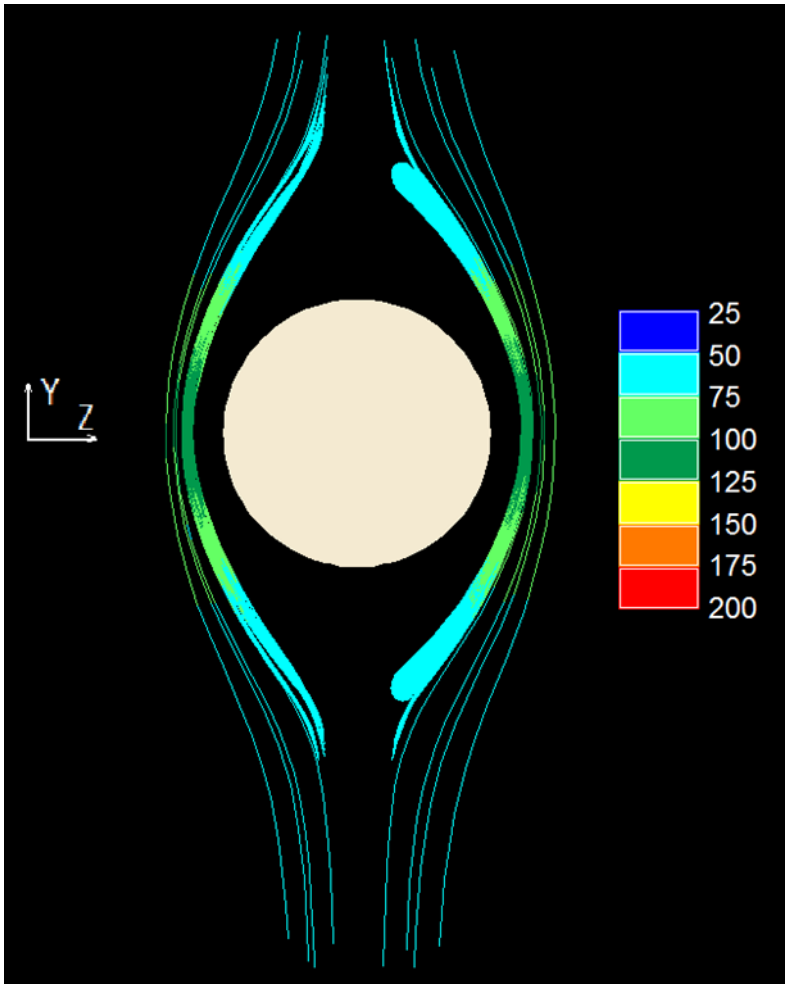


Figure 6.4.10: A vertical section across an eight-metre diameter tunnel depicting orientations of fractures on the sidewall (σx= 52.5 MPa σy= 70 MPa, σz= 25 MPa).

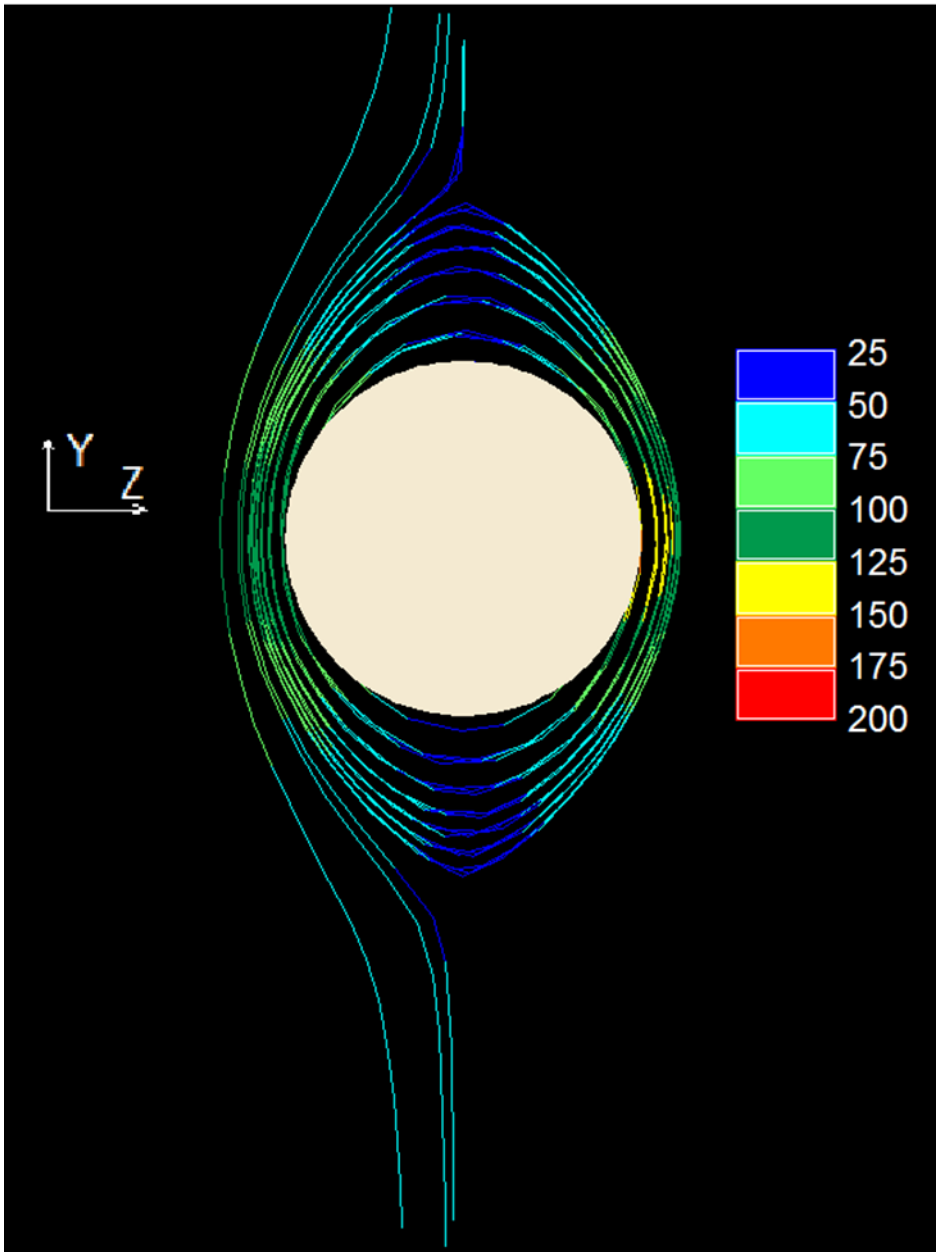


Figure 6.4.11: A vertical section across an eight-metre diameter tunnel depicting orientations of fractures on the sidewall (σx= 35 MPa σy= 70 MPa, σz= 35 MPa).

6.5 **Potential Slab for Buckling**

According to Wesseloo and Stacey (2000), a value of 200 microstrain can be considered as a reasonable critical extension strain magnitude for fracture initiation. This value allows the determination of potential thickness of 'slabs' or extent of blockiness that might be induced during boring operation. Therefore, isosurfaces were generated, similar to subsection 6.3, assuming a critical extension strain of 200 microstrain. McGarr (1997) analysed slab buckling in excavation sidewalls, with dimension L, taking the maximum stress in the excavation sidewall (σ) to be close enough to the magnitude of the UCS, which would generate several cracks parallel to the free surface. The equation below was used to analyse the generated slabs, with thickness of h. A similar approach was followed in the case of the present research, in which a UCS of 180 MPa was used. The following results were obtained:

$$\frac{\mathbf{h}}{\mathbf{L}} = \frac{\mathbf{2\sqrt{3}\sqrt{1-\upsilon^2}}}{\boldsymbol{\pi}} \sqrt{\frac{\boldsymbol{\sigma}}{\mathbf{E}}} \quad \text{.....(24)}$$

$$\frac{\mathrm{h}}{\mathrm{L}} = \frac{2\sqrt{3}\sqrt{1-0.2^2}}{\pi} \sqrt{\frac{180}{50000}} \quad \text{.....(25)}$$

$$= 0.0648$$

Therefore $\frac{L}{h} = 15.43$, (slenderness ratio) which is similar to l/t, in Kazakidis (2002) using Euler's formula to calculate buckling stress (σ_b), that is,

$$\sigma_b = \pi^2 \frac{E}{12(l/t)^2} \text{.....(26)}$$

$$= 172.8 \text{ MPa}$$

These values are indications of the critical stress at which slabbing would take place, and the slenderness ratio of 15.43, below which buckling failure will occur. The amplitude of flexure is given by:

$$c_1 = \left(2/h\right)\left(\frac{L}{\pi}\right)^2\left(\frac{1-\nu^2}{E}\right)S \quad \text{.....(27)}$$

$$= 0.000664L^2/h$$

Where:

L: Diameter

σ1 (S): Applied stress

h or t: Slab thickness

l/t or L/h: Slenderness ratio

σb: Buckling stress

C1: Amplitude of flexure

It is known from literature that the amplitude (chapter 4 subsection 4.2 b) of flexure determines the point where an extensional strain exceeds the compressive strain associated with the applied load. This serves as a point when the tensile crack would propagate, breaking the slab into two parts. It is apparent from the results obtained, that for the specified mechanical properties of rock masses, the amplitude of flexure will be dependent on the ratio of the square of the 'slab' length to 'slab' thickness.

Similar models to McGarr (1997), were generated from the results obtained in Examine 3D, as indicated in Figure 6.5.1 and Figure 6.5.2. It can be seen that, at the point where possible buckling is expected, the σ1/σ3 ratios range from 3.5 to 3.8 for a six-metre diameter tunnel

and 3 to 5 for an eight-metre diameter tunnel. The above equations were used to calculate some of the important parameters for the analysis of slab buckling. The results are summarised in Table 6.5.1 and Table 6.5.2 and other results can be seen in Appendix B. For these values, graphs of generated stress versus slenderness ratio were plotted, shown in Figure 6.5.3 and Figure 6.5.4, where an average slenderness ratio of 13 is predicted for 180 MPa, as indicated by red arrows on the graphs. It is apparent that the buckling stress is dependent on the slenderness ratio and elastic modulus.

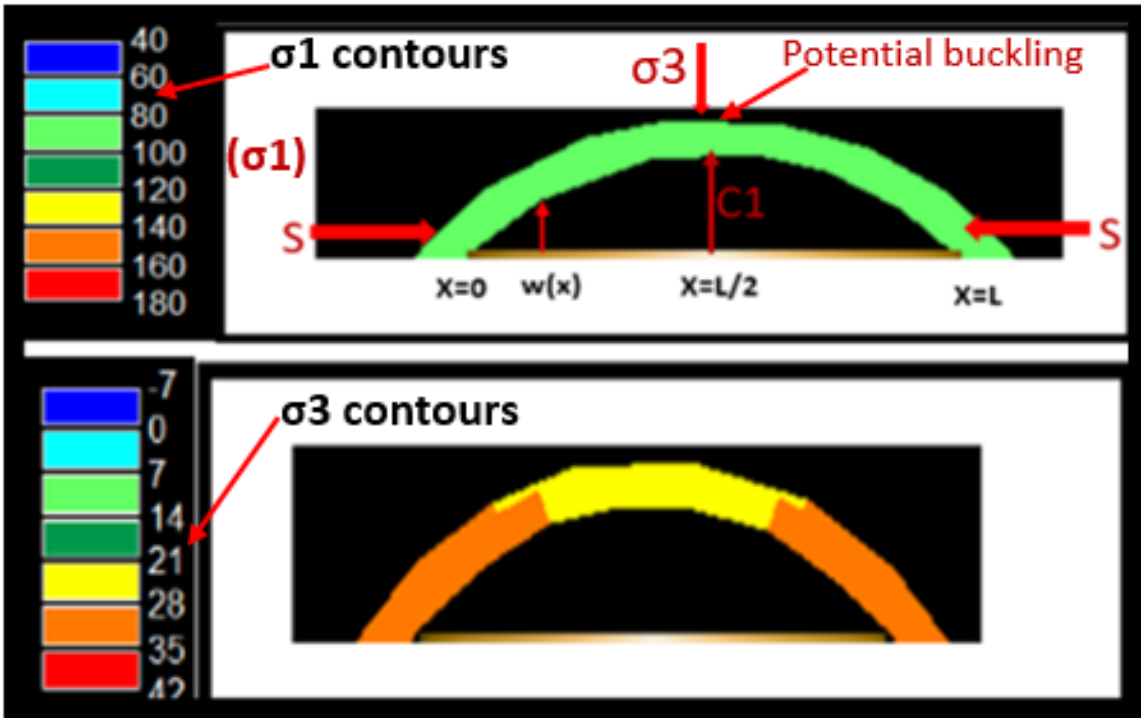


Figure 6.5.1: The potential slab geometry and the magnitudes of acting stresses depicted by contours for a six-metre diameter tunnel.

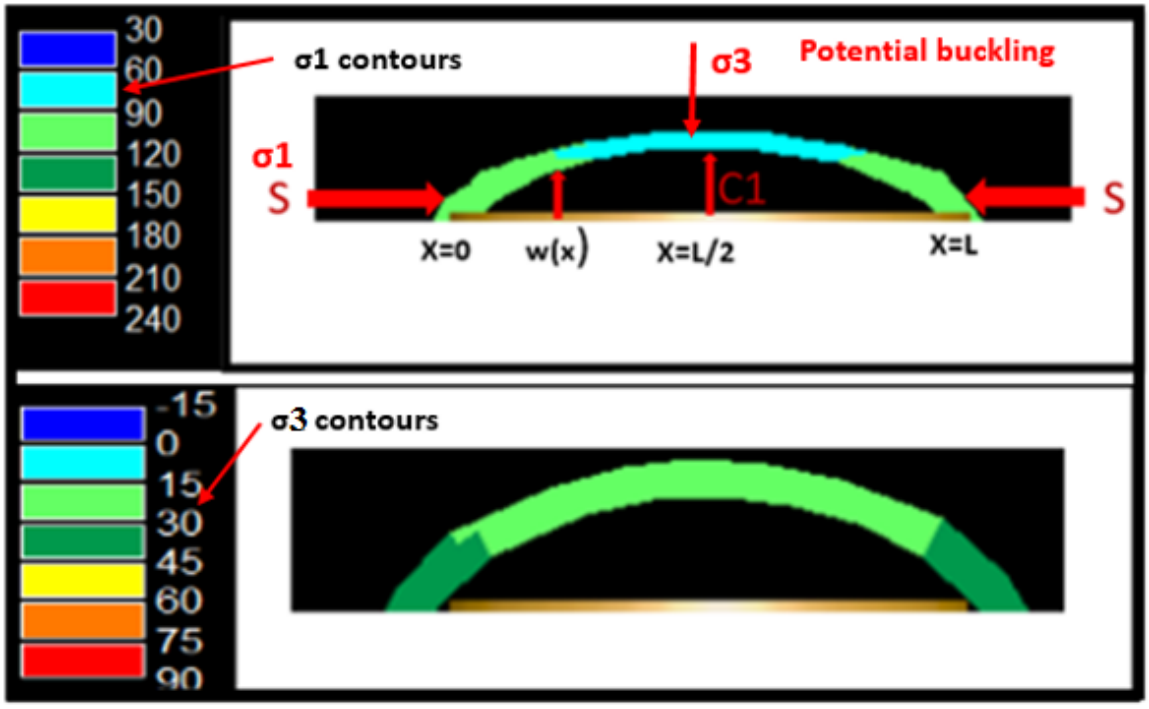


Figure 6.5.2: The potential slab geometry and the magnitudes of acting stresses depicted by contours for an eight-metre diameter tunnel.

Table 6.5.1: Summary of slab thickness, slenderness ratios and buckling stresses.

In Situ Stresses							
σx= 70 MPa, σy= 35 MPa, σz= 70 Mpa							
Diameter, L(m)	σ3 (MPa)	σ1 (MPa)	h/L or l/t	h or t (m)	(l/t)	σb (MPa)	σ1/σ3
2	33	70	0,038	0,075	26,635	57,967	2,12
4	33	70	0,038	0,150	26,635	57,967	2,12
6	28,5	90	0,043	0,255	23,490	74,529	3,16
8	15	100	0,045	0,359	22,284	82,810	6,67

Table 6.5.2: Summary of slab thickness, slenderness ratios, buckling stresses.

In Situ Stresses							
σx=35 MPa, σy= 35 MPa, σz= 70 Mpa							
Diameter, L(m)	σ3 (MPa)	σ1 (MPa)	h/L or l/t	h or t (m)	(l/t)	σb (MPa)	σ1/σ3
2	30	65	0,036	0,072	27,641	53,827	2,17
4	31,5	70	0,038	0,150	26,635	57,967	2,22
6	28	80	0,040	0,241	24,915	66,248	2,86
8	30	90	0,043	0,341	23,490	74,529	3,00

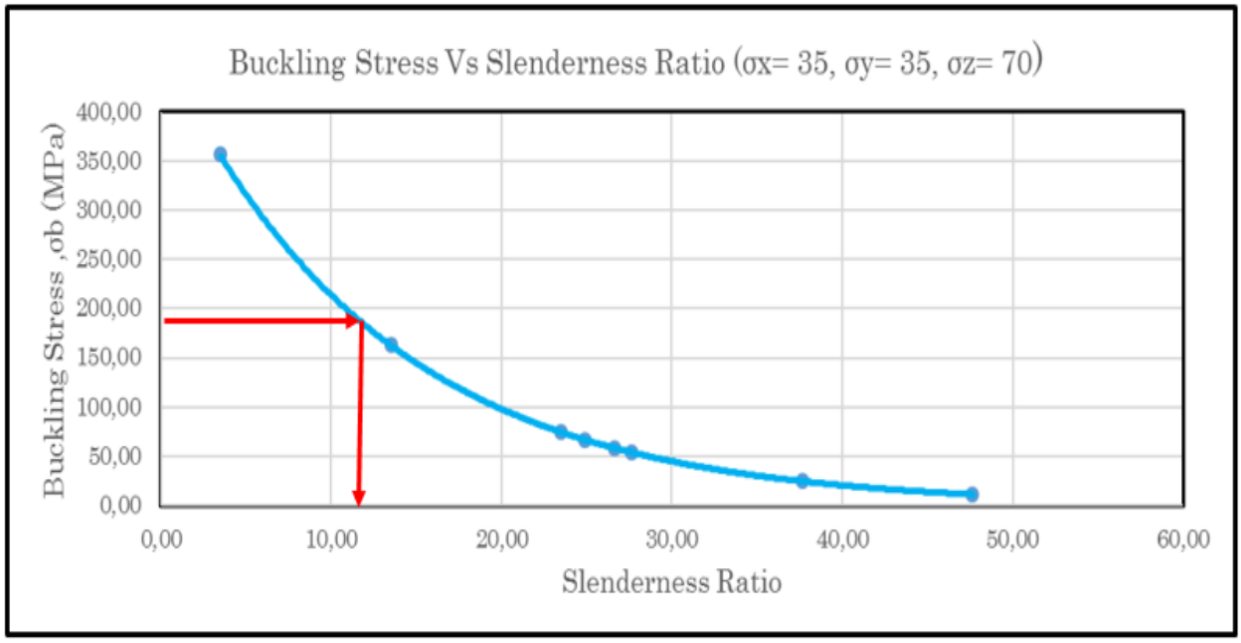


Figure 6.5.3: Buckling stress versus slenderness ratio for buckling failure.

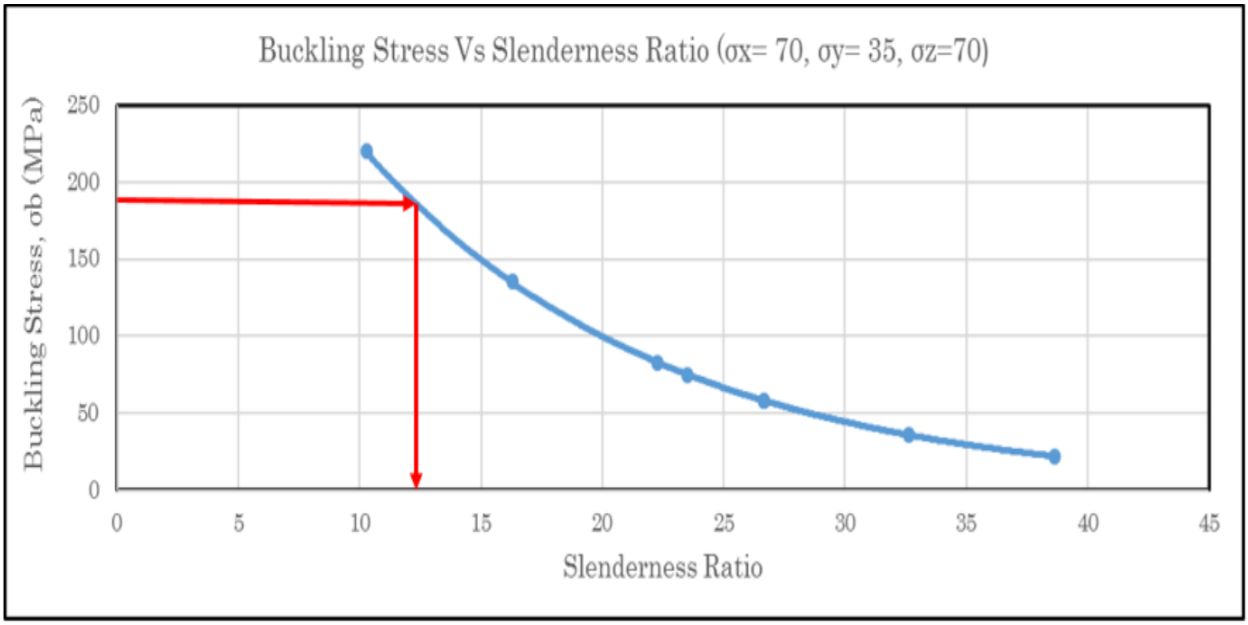


Figure 6.5.4: Buckling stress versus slenderness ratio for buckling failure

It is evident that the smaller the slenderness ratio, the larger the buckling stress needed for buckling. When comparing the applied stress (σ1) and the buckling stress (σb) it can be seen that buckling is predicted. It is worth noting that the slab thicknesses determine the extent of stability problem, in the case of this research, the boring difficulty. For instance, comparing a four-metre diameter tunnel with an eight-metre diameter tunnel, the slab thicknesses predicted are 150 mm and 340 mm, respectively. This implies that, owing to the much greater volume of rock involved, an eight-metre diameter tunnel would cause more boring problems than a four-metre tunnel at the same depth.

Contrary to this, when considering the buckling stress, taking into account the UCS of the rock, buckling is not predicted. According to Kazakidis (2002), the disadvantage of using Euler's approach is the fact that as the slenderness ratio increases, the presence of

imperfections is likely to increase. Therefore, buckling of material can still occur, even under low critical loads (P_{cr}). In order to overcome this, the eccentricity of the applied load is considered, where the strength of the material is not taken into consideration. Therefore, the criterion of failure is based on the magnitude of the compressive (σ_{compr}^{max}) and tensile(σ_{tens}^{max}) stresses in the material. The following equations are used to calculate these parameters:

$$\sigma_{compr}^{max} = \sigma + 6\frac{\sigma}{t}\left[\frac{e}{cos\left(\frac{l}{t\sqrt{3\frac{\sigma}{E}}}\right)}\right] \quad \text{.....(28)}$$

and

$$\sigma_{tens}^{max} = \sigma - 6\frac{\sigma}{t}\left[\frac{e}{cos\left(\frac{l}{t\sqrt{3\frac{\sigma}{E}}}\right)}\right] \quad \text{.....(29)}$$

Application of these formulae yields the results in Table 6.5.3, Table 6.5.4, Figure 6.5.5 and Figure 6.5.6, assuming eccentricity (e) of t/4. It can be seen that potential buckling can be predicted when slenderness ratio is 26.2 or less, indicating that compressive strength has been exceeded. This area is indicated as an unstable zone. The zone within the limits of UCS and UTS denotes stability, as can be seen in both Figure 6.5.5 and Figure 6.5.6.

Kazakidis (2002) conducted a further analysis, considering confinement, to determine the confining pressure beyond which failure would be initiated. The equations below were used to determine maximum compressive and tensile stresses:

$$\sigma_{max} = \sigma + 6\frac{\sigma}{t}\left[\frac{e}{cos\left(\frac{l}{t\sqrt{3\frac{\sigma}{E}}}\right)} - \frac{5ql^4}{32Et^3}\right] - \frac{3ql^2}{4t^2} \quad \text{.....(30)}$$

and

$$\sigma_{min} = \sigma - 6\frac{\sigma}{t}\left[\frac{e}{cos\left(\frac{l}{t\sqrt{3\frac{\sigma}{E}}}\right)} - \frac{5ql^4}{32Et^3}\right] + \frac{3ql^2}{4t^2} \text{.....(31)}$$

Table 6.5.3: Results for eccentric load approach for the determining maximum compressive and tensile stresses for σx=35 MPa, σy = 35 MPa, σz= 70 MPa.

D (m)	t (m)	σ (MPa)	l/t	σ_{compr}^{max} (MPa)	σ_{tens}^{max} (MPa)
2	0.075	65	27.64	163	-33
4	0.150	70	26.64	175	-35
6	0.255	80	24.91	200	-40
8	0.359	90	23.49	225	-45

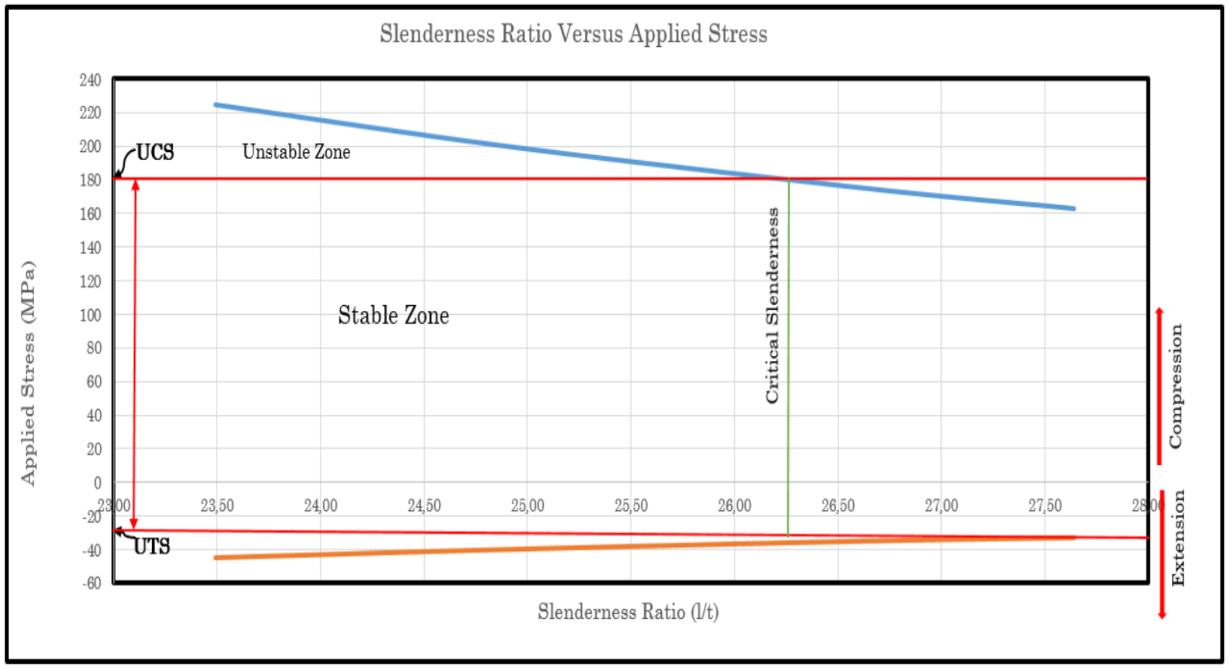


Figure 6.5.5: Determination of critical slenderness ratio for buckling analysis under eccentric load.

Table 6.5.4: Results for eccentric load approach for the determining maximum compressive and tensile stresses for σx = 70 MPa, σy = 35 MPa, σz = 70 MPa.

D (m)	t (m)	σ (Mpa)	l/t	e (t/4)	σcom(MPa)	σtens(MPa)
2,00	0,08	70,00	26,64	0,02	175,58	-35,58
4,00	0,15	70,00	26,64	0,04	175,66	-35,66
6,00	0,26	90,00	23,49	0,07	226,06	-46,06
8,00	0,36	100,00	22,28	0,09	251,34	-51,34

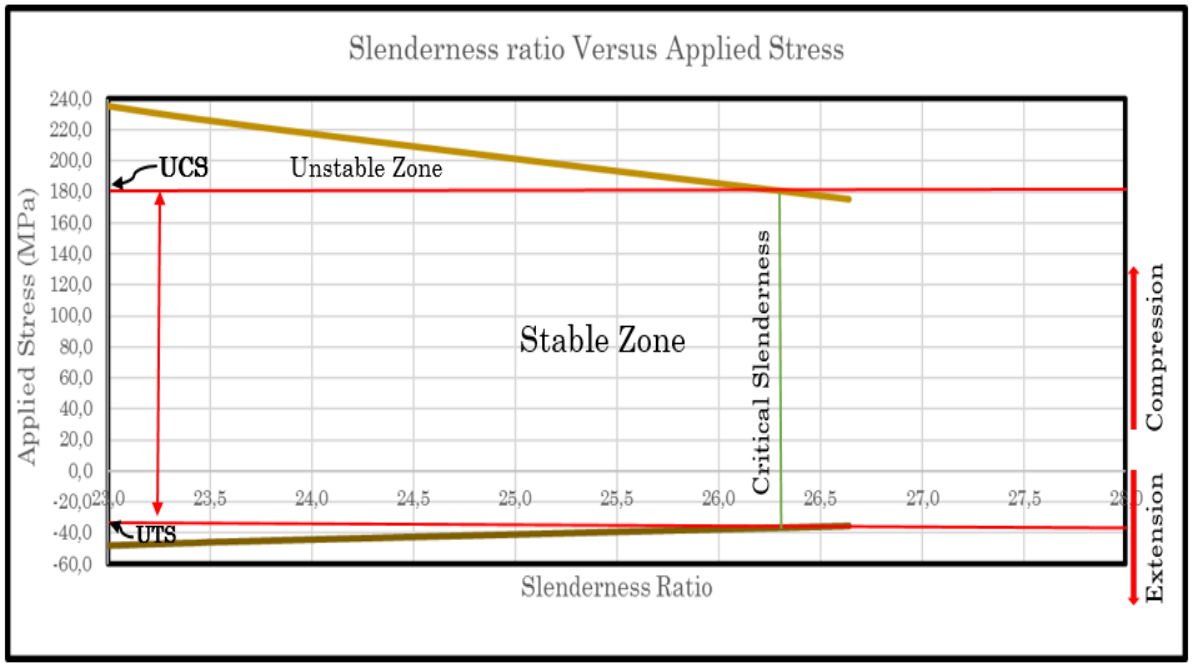


Figure 6.5.6: Determination for critical slenderness ratio of buckling analysis under eccentric load.

When using the Qiu et al. (2014) approach to analyse slab buckling, equations 19 to 21 were used. As far as this research is concerned, additional parameters used in these equations were obtained from literature, as shown in Table 6.5.5, as well as in those Table 4.2.1. A similar approach to Kazakidis (2002), was followed in order to determining maximum compressive and tensile stresses for the analysis of buckling.

Table 6.5.5: Input parameters for analysis for buckling.

Parameters	
UTS (MPa)	27
JRC	20
JCS (MPa)	180 (UCS)

L (m)	3
σ_n (MPa)	0.1
ϕ_r (°)	31.5

The slab thickness is calculated as follows:

$$\delta_{peak} = 0.0077\left[L^{0.45}\left(\frac{\sigma_n}{JCS}\right)^{0.34}\right]\cos\left[JRC\log_{10}\frac{JCS}{\sigma_n}\right] \quad \text{.....(32)}$$

$$= 0.000930388\text{m}$$

$$\tau_{peak} = \sigma_n\left[JRC\log_{10}\left(\frac{JCS}{\sigma_n}\right) + \phi_r\right] \quad \text{.....(33)}$$

$$=5.453\ \text{MPa}$$

$$k_s = \tau_{peak/\delta_{peak}} \quad \text{.....(34)}$$

$$= 5.86\ \text{GPa/m}$$

$$t = \left(\frac{0.1453\text{UTS}}{\sqrt{5}\ k_s}\right)^{2/3} \quad \text{.....(35)}$$

$$= 0.00448\ \text{m}$$

$$=4.48\text{mm}$$

Therefore, the limit load can be determined from:

$$E' = E/(1\text{-}v^2) \quad \text{.....(36)}$$

$$\lambda = \frac{G}{k_s} \quad \text{.....(37)}$$

$$= 8.89$$

$$\sigma_{cr} = -\frac{\pi^2 E' t^2}{12L^2} + \frac{t}{\lambda}G \quad \text{.....(38)}$$

$$= 25.87\ \text{MPa}$$

6.6 **Conclusion**

A series of stress analysis, using numerical modelling program, has been conducted to determine the stress and strain distribution around and ahead of the faces of circular tunnels of various dimensions. Moreover, using an extension strain fracture criterion, the potential extents of fracturing ahead of the faces were analysed, as well as the orientations of the extension fractures, relative to the direction of principal stresses. From these results, slab thicknesses and their potential for failure were assessed. Furthermore, the stability was assessed by applying Kazakidis (2002), Qiu et al. (2014) and McGarr (1997) approaches, to assess the buckling loads, minimum and maximum compressive and tensile stresses. It was apparent that tunnels with larger diameters are more prone to significant failures than smaller diameter tunnels.

CHAPTER 7

CONCLUSIONS AND RECOMMENDATIONS

Research has been carried out into the potential occurrence of fracture zones in the rock mass around and ahead of bored excavations. A review of literature has indicated the importance of the behaviour of rock in such zones under high stress conditions. Rock bursting has been reported in bored tunnels in China and Switzerland, in some cases with serious consequences. The investigations carried out for this research report have involved a substantial review of relevant literature, and a series of three dimensional numerical stress analyses to determine the stress magnitudes and orientations around and ahead of a bored tunnel. The analyses were carried out for several different sets of in situ stresses using the Examine3D package. Extension strains were calculated from the resulting stress distributions, and these were used to define potential fracture zones, assuming an extension strain criterion for initiation of fractures. Although the scope of the research and analyses carried out for this research report was necessarily limited, the results of the analyses have shown clearly that substantial fracture zones can develop around a bored excavation. The geometries of the predicted fracture zones depend on the in situ stress magnitudes and the ratios between the three principal stresses. The orientations of fractures predicted from the analyses are very conducive for the potential occurrence of slabs of rock in the form of curved plates and shells. The buckling of such plates and shells is likely to be the source of the rock bursts that have been observed. The buckling stability of these slabs was evaluated at a preliminary level, which has shown the influence of slab thickness and tunnel size.

The following conclusions have been drawn from the research carried out:

- When excavations are created, the stress concentration and zones of extension, and resulting fracture zones, are formed around and ahead of the excavations. The fractured zone is a function of tunnel size. This implies that if the size of the tunnel increases the fractured zone increases as well. For instance, a fractured zone of 1.3 m was predicted for a four-metre tunnel, whereas, a fractured zone of about 2.4 m was predicted for an eight-metre tunnel.
- The orientation of extension fractures is normal to the direction of minor principal stress (σ3).
- When tunnels advance into these fractured zones, slabs or incipient plates are formed.
- The extent of fracturing ahead of the tunnels is dependent on the ratio of the three principal stresses. Isosurfaces determined from the 3D stress analyses, indicating zones of extension, show unusual geometries. It was discovered that, under the same stress fields, an eight-metre tunnel is more prone to boring problems compared with a four-metre and six-metre tunnels. For instance, slabs of 150 mm thick, in the case of a four-metre tunnel, 255 mm thick in case of six-metre tunnel and 360 mm thick, in case of an eight-metre tunnel, are likely to be formed.
- The stability of these slabs depends on the principal stress ratio and the mechanical properties of the rock mass. Owing to probable imperfections in the rock, slab failure could occur even under low critical loads or stresses, which are below the UCS.

Finally, therefore, the research questions posed have been answered: stresses induced around a bored excavation have been determined for several in situ stress fields, and the potential for fracturing predicted using an extension strain criterion for fracture initiation. The orientations of the fractures have been determined from the stress analyses, and the impact of the fracturing, resulting from the formation of "slabs" of rock, determined by consideration of the potential for buckling of the slabs. However, further research is necessary to define the likely thicknesses of individual plates and shells, and hence their proneness to buckling.

REFERENCES

Abel, J F and Lee, F T. (1973), Stress changes ahead of an advancing tunnel, *Int. J. Rock Mech. Min. Sci. Geomech. Abstr.,* 10(6), pp. 673-697.

Aglawe, J P. (1999), *Unstable and Violent Failure around Underground Openings in Highly Stressed Ground. Ph.D. thesis, Mining Department,* Kingston, Ontario: Queen's University.

Barton, N and Choubey, V. (1976), The Shear Strength of Rock Joints in Theory and Practice, *Rock Mechanics 10,* pp. 1-54.

Barton, N and Shen, B. (2017), *Extension failure mechanisms explain failure initiation in deep tunnels and critical heights of cliff faces and near-vertical mountain walls.* San Franscisco, California, American Rock Mechanics Association.

Bazant, Z P Lin, F B and Lippmann, H. (1993), Fracture energy release and size effect in borehole breakout, *International Journal for Numerical and Analytical Methods in Geomechanics,* Volume 17, p. 1-14.

Bieniawski, Z T. (1967a), Mechanism of brittle fracture of rock Part I-Theory of the fracture of rock, *Int. J. Rock Mech. Min. Sci.,* Volume 4, pp. 395-406.

Bieniawski, Z T. (1967c), Mechanism of brittle fracture of rock Part III-Fracture in tension and under long-term loading, *Int. J. Rock Mech. Min. Sci.,* Volume 4, pp. 425-430.

Bilgin, N Copur, H and Balci, C. (2014), *Mechanical Excavation in Mining and Civil Industry,* New York: CRC Press Taylor and Francis Group.

Brace, W F and Bombolakis, E. (1963), A note on brittle crack growth in compression, *J. Geophys. Res.,* Volume 68, pp. 3709-3713.

Brace, W F Paulding, B and Scholz, C. (1966), Dilatancy in the fracture of crystalline rocks, *J Geophys. Res.,* Volume 71, pp. 3939-3953.

Brady, B H G and Brown, E T. (2004), *Rock Mechanics for underground mining,* Third edition. Dordrecht, The Netherlands. Springer.

Brown, E T. (1974), Fracture of rock under biaxial compression. In: Advances in Rock Mechanics, *Proceedings of the 3rd Congress of the International Society of Rock Mechanics, Denver, Washington (DC): National Academy Science,* Volume 2A, pp. 111-117.

Brown, E T and Trollope, D H. (1967), The failure of linear brittle material under effective tensile stress, *Rock Mech. Eng. Geol. V.,* pp. 229-241.

Brox, D. (2013), Technical considerations for TBM tunnelling for mining projects, *Transactions of the society for mining, metallurgy, and exploration,* Volume 334, pp. 498-505.

Burgess, H and Taylor, J G. (1980), Tunnel boring in a deep South African gold mine, *Trans. I.M.M., Section A, April 1980,* pp. A84-A98.

Cai, M Kaiser, P K Tasaka, Y Maejima, T Morioka, H and Minami, M. (2004), Generalized crack initiation and crack damage stress thresholds of brittle rock masses near underground excavations,

International Journal of Rock Mechanics and Mining Sciences, 41(5), pp. 833-847.

Chamber of Mines, (2015), *Integrated annual review 2015,* Johannesburg: Chamber of Mines of South Africa.

Cigla, M Yagiz, S and Ozdemir, L. (2001), *Application of tunnel boring machines in underground mine development,* Ankara, Proceedings of the 17th International Mining Congress and Exhibition of Turkey, pp. 155-164.

Coulthard, M A. (1999), Applications of numerical modelling in underground mining and construction, *Geotechnical and Geological Engineering,* Volume 17, p. 373–385.

Crowley, K (2014), *AngloGold sees reef-boring technology doubling mines life,* [Online]
Available at: http://www.mineweb.com/news/technology/anglogold-sees-reef-boring-technology-doubling-mines-life/
[Accessed 11 December 2016].

Daehnke, E T Salamon, M G and Roberts, M K C. (2000), Quantifying stable hangingwall spans between support units, *Jl. S. Afri. Inst. Min. Metall.,* pp. 375-388.

Diederichs, M S. (2007), The 2003 Canadian geotechnical colloquium: mechanistic interpretation and practical application of damage and spalling prediction criteria for deep tunnel, *Canadian Geotechnical Journal,* 44(9), pp. 1082-1116.

Diederichs, M S Kaiser, P K and Eberhardt, E. (2004), Damage initiation and propagation in hard rock during tunnelling and the influence of near-face stress rotation, *International Journal of Rock Mechanics and Mining Sciences,* Volume 41, pp. 785-812.

Durrheim, R. (2010) *Mitigating the risk of rockbursts in the deep hard rock mines of South Africa: 100 years of research,* Johannesburg, CSIR Centre for Mining Innovation and the University of the Witwatersrand, Johannesburg, South Africa.

Dyskin, A V Sahouryeh, E Jewell, R J Joer, H and Ustinov, K B. (2003), Influence of shape and locations of initial 3-D cracks on their growth in uniaxial compression, *Engineering Fracture Mechanics,* Volume 70, pp. 2115-2136.

Dyskin, A V and Salganik, R L. (1987), Model of dilatancy of brittle materials with cracks under compression, *Mech. Solids,* 22(6), pp. 165-173.

Dyskin, A Y and Germanovich, L N. (1993), Model of rockburst caused by cracks growing near free surface, In: R. P. Young, ed. *Rockbursts and Seismicity in Mines.* Rotterdam: Balkema, pp. 169-174.

Eberhardt, E. (2001), Numerical modelling of three-dimension stress rotation ahead of an advancing tunnel face, *International Journal of Rock Mechanics and Mining Science,* Volume 38, pp. 499-518.

Eberhardt, E Stead, D Stimpson, B and Read, R S. (1998) Identifying crack initiation and propagation thresholds in brittle rock, *Can. Geotech. J.,* 35(2), p. 222–233.

Fairhurst, C and Cook, N W. (1966), The phenomenon of rock splitting parallel to the direction of maximum compression in the neighbourhood of a surface, *Proc. of the 1st Congress of the Int. Society of Rock Mechanics, Lisbon,* pp. 687-692.

Ferreira, P H. n.d. *Large Diameter Vertical Raise Drilling and Shaft Boring Techniques as an Alternative to Conventional Vertical Shaft Sinking Techniques,* Johannesburg: Murray and Roberts Ruc Limited.

Gong, Q M Yin, L J Wu, S Y Zhao, J and Ting, Y. (2012), Rock burst and slabbing failure and its influence on TBM excavation at headrace tunnel in Jinping II hydropower station, *Engineering Geology,* Volume 124, pp. 98-108.

Graham, P C. (1976), *Some problems associated with the use of a tunnel machine in deep-level gold mines, in Tunnelling '79,* London, ed. M. J. Jones, I.M.M, pp 397-403.

Grimstad, E. (1986), *Rock-burst problems in road tunnels, in Norwegian Road Tunnelling, Pub. No., Norwegian Soil and Rock Engineering Association.* s.l., Tapir Publishers, University of Trondheim.

Gumede, H. (2006), *Development of data sets on joint characteristics and consideration of associated instability for a typical South African gold mine, MSc Eng. Dissertation,* Johannesburg: University of the Witwatersrand.

Haimson, B and Chang, C. (2000), A new true triaxial cell for testing mechanical properties of rock, and its use to determine rock strength and deformability of Westerly granite, *International Journal of Rock Mechanics and Mining Sciences,* Volume 37, p. 285–296.

Handin, J Heard, H C and Magouirk, J N. (1967), Effects of the intermediate principal stress on the failure of limestone, dolomite, and glass at different temperatures and strain rates, *J. Geophys. Res.,* Volume 72, pp. 611-640.

Heal, D P. (2010), *Observations and analysis of incidences of rockburst damage in underground mines, Ph.D. thesis,* Perth, Australia: The University of Western Australia, School of Civil and Resource Engineering.

Hoek, E. (1987), *Practical Rock Engineering,* Toronto: University of Toronto.

Hoek, E and Martin, C D. (2014), Fracture initiation and propagation in intact rock - A review, *Journal of Rock Mechanics and Geotechnical Engineering,* Volume 6, pp. 287-300.

Hudson, J A. (2003), *Comprehensive modelling of the underground environment: The requirement and the reality,* Lisse, The Netherlands, Swets and Zeitlinger B.V.

Huston, R and Josephs, H. (2008), *Practical Stress Analysis in Engineering Design,* Third Edition ed. New York: Taylor & Francis Group, LLC.

Iannacchione, A T Dolinar, D R Prosser, L J Marshall, T E Oyler, D C and Compton, C S. (1998), Controlling roof beam failures from horizontal stresses in underground stone mines, *In Proceeding, 17th International Conference on Ground Control in Mining,* Volume 4, pp. 102-112.

Jager, A J and Ryder, J A. (1999), *A handbook in Rock engineering practice for tabular hard rock mines,* Johannesburg: The Safety in Mines Research Advisory Committee (SIMRAC).

Jinga, L and Hudson, J A. (2002), Numerical methods in rock mechanics, *International Journal of Rock Mechanics and Mining Sciences,* Volume 39, p. 409–427.

Joughin, N C. (1976) Potential for the mechanization of stoping in gold mines, *A Journal of the South African Institute of Mining and Metallurgy,* pp. 285-300.

Kaiser, P K and Cai, M. (2012), Design of rock support system under rockburst condition, *Journal of Rock Mechanics and Geotechnical Engineering,* 4 (3), p. 215–227.

Kaiser, P K Diederichs, M S Martin, C D Sharp, J and Steiner, W. (2000), *Underground works in hard rock tunnelling and mining, In ISRM International Symposium,* s.l., International Society for Rock Mechanics.

Kaiser, P K McCreath, D and Tannant, D. (1996), *Canadian Rock burst Support Handbook,* Sudbury: Geomechanics Research Centre and CAMIRO.

Kaiser, P and McCreath, D. (1994), Rock Mechanics Considerations for Drilling or Bored Excavations in Hard Rock, *Tunnelling and Underground Space Technology,* 9(4), pp. 425-437.

Kazakidis, V N. (2002), Confinement effect and energy balance analyses for buckling failure under eccentric loading condition, *Rock Mech. Rock Engng.,* 35(2), pp. 115-126.

Kirsten, H A D and Klokow, J. (1979), Control of fracturing in mine rock passes, *Proc. 4th Int. Congr. ISRM. Montreux,* Volume 1, pp. 203-210.

Krenzke, M A and Charles, R. (1963), *The elastic buckling strength of spherical glass shells (No. DTMB-1759),* Washington DC: David Taylor Model Basin.

Kupfer, H Hilsdorf, H K and Rusch, H. (1969), Behaviour of concrete under biaxial stresses, *ACI J.,* 66(52), pp. 656-666.

Larsson, K. (2004), *Mining Induced seismicity in Sweden, MSc. research report,* Sweden: Lulea University of Technology.

Lau, J S O and Gorski, B. (1992), *Uniaxial and triaxial compression tests on URL rock samples from boreholes 207-045-GC3 and 209-069-PH3,* s.l.: CANMET Divisional Report MRL 92 – 025 (TR), Mining Research Laboratories.

Lee, S M Park, B S and Lee, S. (2004), Analysis of rockburst that have occurred in a waterway tunnel in Korea, *Int. J. Rock Mech. Min. Sci.,* 41(3), pp. 1-6.

Li, D Ngai, L and Wong, Y. (2013), The Brazilian disc test for rock mechanics applications: Review and new insights, *Rock Mech. Rock Eng.,* Volume 46, p. 269–287.

Li, S Feng, X T Li, Z Chen, B Zhang, and C Zhou, H (2012), In situ monitoring of rockburst nucleation and evolution in the deeply buried tunnels of Jinping II hydropower station, *Engineering Geology,* Volume 137–138, p. 85–96.

Li, S J Feng, X T and Li, Z H. (2011), In situ experiments on width and evolution characteristics of excavation damaged zone in deeply buried tunnels, *Science China Technological Sciences,* Volume 54 (s1), p. 167–174.

Loew, S Barla, G and Diederichs, M. (2010), Engineering geology of Alpine tunnels: Past, present and future. *In Geologically active—Proceedings of the 11th IAEG Congress,* pp. 201-253.

Maidl, B Schmid, L Ritz, W and Herrenknecht, M. (2008), *Hardrock Tunnel Boring Machines,* Switzerland: Ernst and Sohn.

Martin, C D. (1997), The effect of cohesion loss and stress path on brittle rock strength, Seventeenth Canadian Geotechnical Colloquium, *Can. Geotech. J.,* 34(5), p. 698–725.

Martin, C D and Chandler, N A. (1994), The progressive fracture of Lac du Bonnet granite, *Int. J. Rock Mech. Min. Sci. Geimech. Abstr.,* 31(6), pp. 643-659.

Martin, C D Kaiser, P and McCreath, D. (1998), *Hoek-Brown parameters for predicting the depth of brittle failure around tunnels,* Sudbury: Geomechanics Research Centre.

McCracken, A and Stacey, T R. (1989), Geotechnical risk assessment for large-diameter raise-bored shafts, *Trans. Instn Min. Metall. (Sect. A: Min. Industry),* pp. 145-150.

McGarr, A. (1997), A mechanism for high wall-rock velocities in rockbursts, *Pure appl. geophys.,* Volume 150, pp. 381-391.

Moriya, H Naoi, M Nakatani, M van aswegen, G Murakami, O Kgarume, T Ward, A K Durrheim, R J Philipp, J Yabe, Y Kawakata, H and Ogasawara, H (2015), Delineation of large localized damage structures forming ahead of inactive mining front by using advanced acoustic emission mapping techniques, *International Journal of Rock Mechanics and Mining Science,* Issue 79, pp. 157-165.

Myrvang, A M and Grimstad, E. (1983), *Rockburst problems in Norwegian highway tunnels- recent case histories,* s.l., in Rock- burst: Prediction and control, I.M.M., pp 133-139.

Ndlovu, X. (2006). *Three dimensional analyses of stress and strain distributions around bord and pillar geometries M.Sc. Eng. Dissertation,* Johannesburg: University of the Witwatersrand.

Ndlovu, X and Stacey, T R. (2007), Observations and analyses of roof guttering in a coal mine. *J. S. Afr. Inst. Min Metal.,* 107(8), p. 477–492.

Nemanashi, V. (2014), *Reef Boring: Innovative Mining,* [Online] Available at: http://cognisancemag.co.za/articles/reef-boring-inovative-mining [Accessed 11 December 2016].

Nicksiar, M and Martin, C D. (2012), Evaluation of Methods for Determining Crack Initiation in Compression Tests on Low-Porosity Rocks, *Rock Mech. Rock Eng.,* Volume 45, pp. 607-617.

Nicksiar, M and Martin, C D. (2013), Crack initiation stress in low porosity crystalline and sedimentary rocks, *Engineering Geology,* Volume 154, pp. 64-76.

Ortlepp, W. D. (1997) *Rock fracture and rockbursts-an illustrative study,* Johannesburg: The South African Institute of Mining and Metallurgy.

Ortlepp, W D and Stacey, T. (2000) *Focus on Southern African Countries, A self mined tunnel at the depth of nearly 3 km,* Johannesburg: SRK Consulting.

Ortlepp, W D and Stacey, T R. (1994), Rockburst mechanisms in tunnels and shafts. *Tunnelling and Underground Space Technology,* 9(1), pp. 59-65.

Pang, S S and Goldsmith, W. (1990), Investigation of crack formation during loading of brittle rock, *Rock Mech. Rock Eng.,* 23(1), p. 53–63.

Pickering, R. (1996) Deep level mining and the role of Rand, *The Journal of The South African Institute of Mining and Metallurgy,* pp. 173-176.

Pickering, R, Smit, A and Moxham, K. (2006), Mining by rock cutting in narrow reefs, *International Platinum Conference 'Platinum Surges*

Ahead', The Southern African Institute of Mining and Metallurgy, pp. 221-230.

Qiu, S, Feng, X and Zhang, C. (2014), Estimation of rockburst wall-rock velocity invoked by slab flexure sources in deep tunnels, *Can. Geotech. J.,* Volume 51, pp. 520-539.

Read, R S, Chandler, N A and Dzik, E J. (1998), In situ strength criteria to tunnel design in highly-stressed rock masses, *Int. J. Rock Mech. Min. Sci.,* 35(3), pp. 261-278.

Sahouryeh, E, Dyskin, A V and Germanovich, L N. (2002), Crack growth under biaxial compression, *Engineering Fracture Mechanics,* Volume 69, p. 2187–2198.

Simmons, J V and Simpson, P J. (2007), Extension, Stress, and Composite Failure in Bedded Rock Masses, *In: Potvin Y (ed) Proc. int. symp. on rock slope stability in open pit mining and civil engineering. Australian Centre for Geomechanics,* p. 213–223.

Skawina, B, Greberg, J, Salama, A and Schunnesson, H. (2014), Mechanical Excavation and Drilling and Blasting –A Comparison Using Discrete Event Simulation, *Mine Planning and Equipment Selection,* pp. 367-377.

Sperry, P E and Heuer, R E. (1972), *Excavation and support of Navajo Tunnel No.3,* New York, Proc. 1st North American RETC, ed K.S.Lane and L.A. Garfield, SME of AIME, V1, pp 539-571.

Stacey, T R. (1981), A Simple Extension Strain Criterion for Fracture of Brittle Rock, *Int. J. Rock Mech. Min. Sci. and Geomech.,* Volume 18, pp. 469-474.

Stacey, T R. (1982), Mechanical mining of strong brittle rock by large diameter "stopecoring"-rock mechanics investigations, *Canadian Rock Mech. Symp., Vancouver,* Volume 14, pp. 96-99.

Stacey, T R. (1989), Boring in massive rocks-rock fracture problems, *Proc. Seminar on Mechanised Underground Excavation, S. Afri. Nat. Council on Tunnelling, November 1989,* pp. 87-90.

Stacey, T R. (2016), Addressing the consequences of dynamic rock failure in underground excavations, *Rock Mech. Rock Eng.,* Volume 49, p. 4091–4101.

Stacey, T R and De Jongh, C L. (1977), Stress fracturing around a deep level bored tunnel, *Jl. S. Afri. Inst. Min. Metall.,* 78(5), pp. 124-133.

Stacey, T R and Harte, N. D. (1989) Deep level raise boring-prediction of rock problems, *Rock at Great Depth, Maury and Fourmaintraux (eds), A A Balkema,* Volume 2, pp. 583-588.

Stacey, T R and Thompson, P W. (1991), *A large borehole breakout?,* Johannesburg, South Africa, In. 7th ISRM Congress, International Society for Rock Mechanics.

Stacey, T R and Yathavan, K. (2003), Example of fracturing of rock at very low stress levels, *Proc.10th Int. Cong. Int. Soc. Rock Mech., Sandton, S. Afri. National Institute of Rock Engineering and S. Afr. Inst. Metall.,* Volume 2, pp. 1155-1159.

Steffanizzi, S, Barla, G and Kaiser, P K. (2007), Numerical modelling of strain driven fractures around tunnels in layered rock masses, *11th Int. Cong. Int. Soc. Rock Mech. Taylor and Francis Group, London,* pp. 971-974.

Tayler, M A, Jain, A K and Ramey, M R. (1972), Path dependent biaxial compressive testing of an all-lightweight aggregate concrete, *J. Am. Concr. Inst.,* Volume 69, p. 758–764.

Taylor, J G, Taylor, R N and Hall, A E. (1978), The introduction of a tunnel borer into a South African gold mine, *J. S. Afri. Inst. Min. Metall.,* Volume 78, pp. 188-198.

Thamer, Y. (1998), *Three-dimensional analysis of lenticular ore using displacement discontinuity elements, PhD. Thesis,* Toronto: Department of Civil Engineering, University of Toronto.

Timoshenko, S. (1936), *"Theory of Elastic Stability,* New York: McGraw-Hill Book Co. Inc.

Toan, N. (2006), *TBM and Lining Essential Interfaces, MSc in Tunnelling and Tunnel Boring Machines,* Turin, Italy: Politecnico di Torino.

van der Merwe, J N. (2011), Future of the South African mining industry and the roles of the SAIMM and the Universities, *The Journal of The Southern African Institute of Mining and Metallurgy,* Volume 111, pp. 581-592.

Vogt, D. (2015), *How technology is going to impact on deep level mining in South Africa,* [Online] Available at: http://www.mineweb.com/news/platinum-group-metals/how-technology-is-going-to-impact-on-deep-level-mining-in-south-africa/ [Accessed 30 September 2016].

Vogt, D, Rossouw A, Hooijer, D, Beech, W, and Joughin, W. (2015), *Deep level gold mining in South Africa,* [Online] Available at: http://www.srk.co.za/files/File/South-Africa/pressreleases/2015/July_2015/Mining_Review_Africa_Where_we

_are_where_were_going_01Jul15_p.44_p.52_1-7.pdf [Accessed 23 09 2016].

Waldeck, H G. (1979) The design and support of large underground chambers at depth in gold mines of Gold Fields Group of South Africa, *Proc. 4th Int. Congr. ISRM. Montreux,* Volume 1, pp. 567-571.

Wesseloo, J and Stacey, T R. (2000), Face and sidewall fracturing in circular excavations and effects on excavation support, *Proc. World Tunnel Congress "tunnel Under Pressure", Durban, South Africa, May 2000, S. Afr. Inst. Min. Metall.,* pp. 553-557.

Wesseloo, J. (2000), Predicting the extent of fracturing around underground excavations in brittle rock, Proc. S. Afr. Young Geotechnical Engineers Conference, Stellenbosch, S. Afr. Instn. Civil Engineering, 12p.

Wesseloo, J and Stacey, T R. (2006), Updated stress database for South Africa, In: *In-situ Rock Stress: Measurement, Interpretation and Application, Proceedings of the International Symposium on In-situ Rock Stress.* Trondheim, Norway, Taylor and Francis, p. 467.

Wesseloo, J and Stacey, T R. (2016), A Reconsideration of the extension strain criterion for fracture and failure of rock, *Rock Mech. Rock Eng.*

Wu, S Y, Shen, M B and Wang, J. (2010) Jinping hydropower project: main technical issues on engineering geology and rock mechanics, *Bulletin of Engineering Geology and the Environment,* Volume 69, pp. 325-332.

Zhang, C Q, Zhou, H and Feng, X (2011b), An index for estimating the stability of brittle surrounding rock mass: FAI and its engineering application, *Rock Mechanics and Rock Engineering,* Volume 44, p. 401–414.

Zhang, C S, Chu, W J and Liu, N. (2011a), Laboratory tests and numerical simulations of brittle marble and squeezing schist at Jinping II hydropower station, China. *Journal of Rock Mechanics and Geotechnical Engineering,* 3(1), pp. 30-38.

Zheng, Y, Zhang, Q and Zhao, J (2016), Challenges and opportunities of using tunnel boring machines in mining, *Tunnelling and Underground Space Technology,* Volume 57, pp. 287-299.

Zheng, Z, Kemeny, J and Cook, N G. (1989), Analysis of borehole breakouts, *Journal of Geophysical Research: Solid Earth,* 94(B6), pp. 7171-7182.

APPENDIX

8.1 Isosurfaces Depicting Areas of Extension and Summary of Results from Examine3D

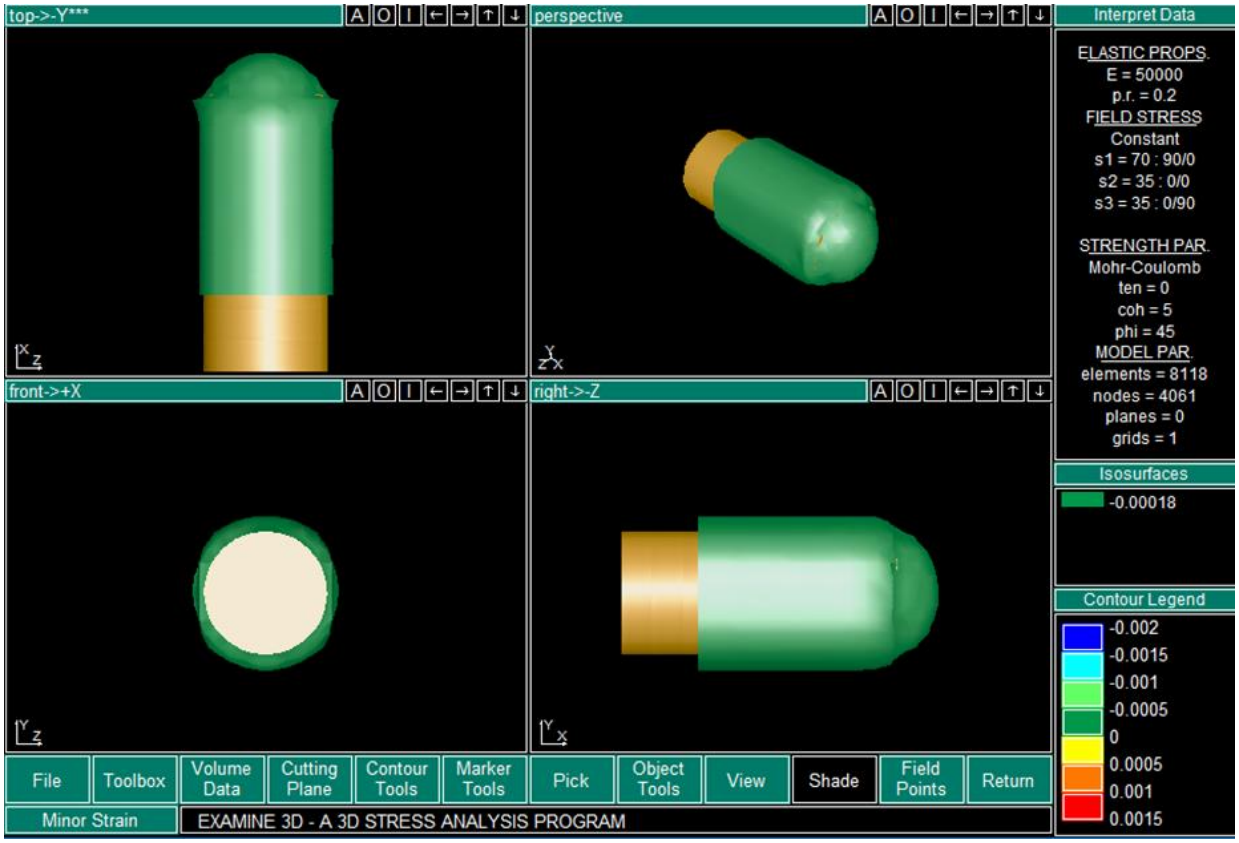


Figure 8.1.1: Isosurfaces of fracture/crack initiation for an eight-metre tunnel for Poisson's ratio of 0.2.

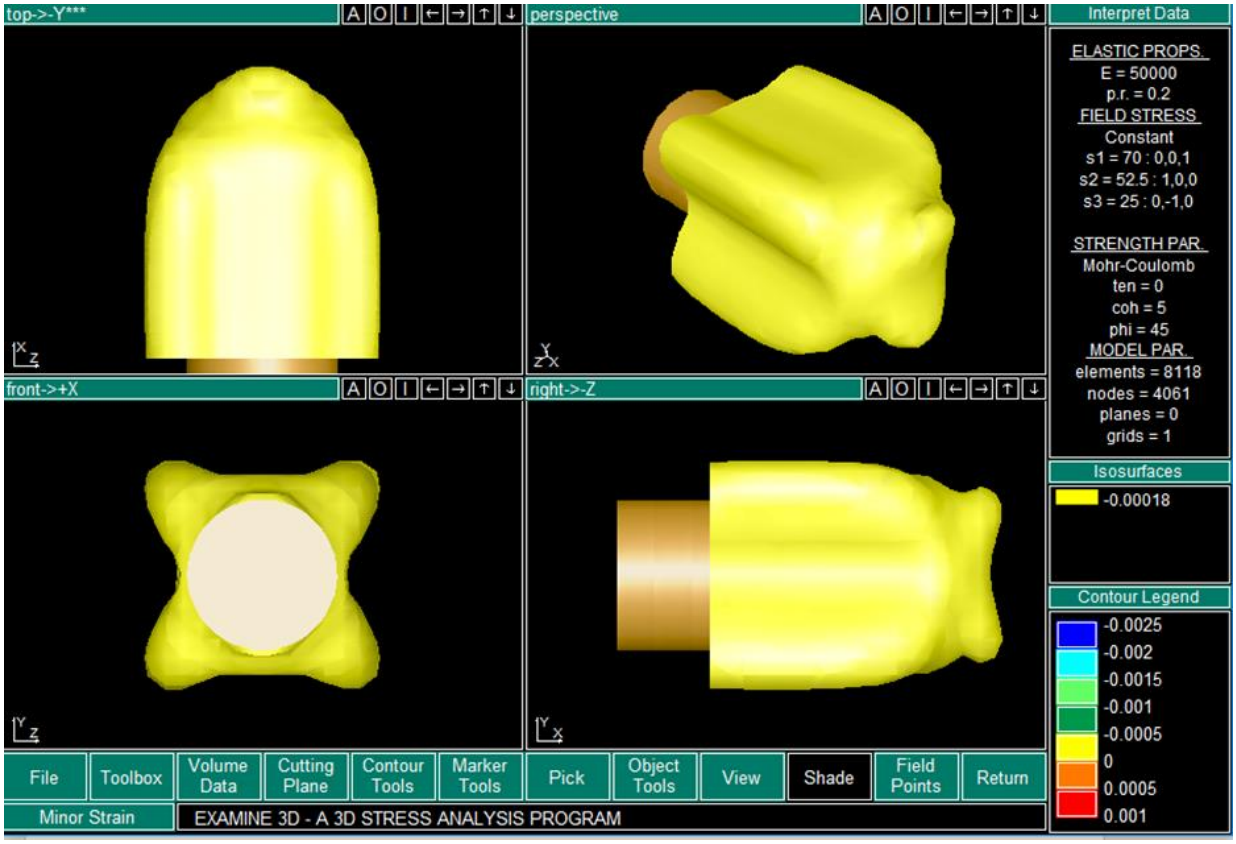


Figure 8.1.2: Isosurfaces of fracture/crack initiation for an eight-metre tunnel for Poisson's ratio of 0.2.

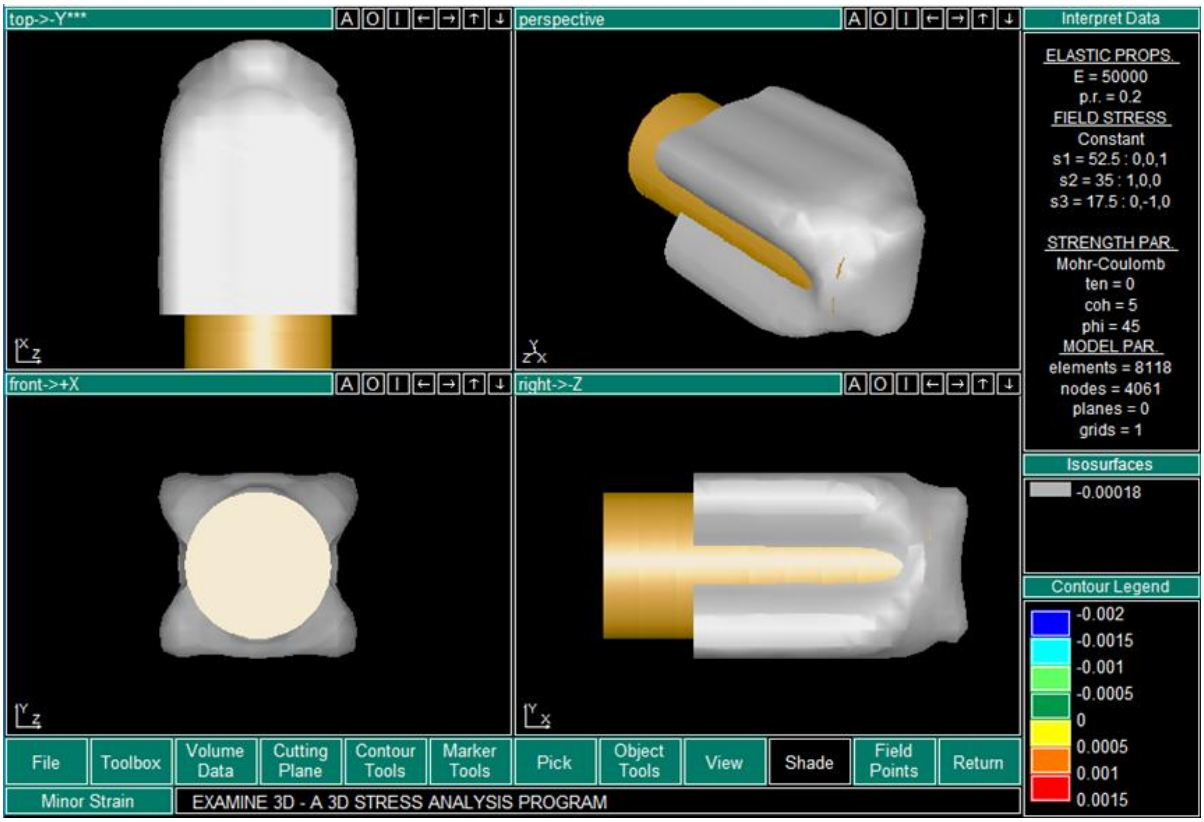


Figure 8.1.3: Isosurfaces of fracture/crack initiation for an eight-metre tunnel for Poisson's ratio of 0.2.

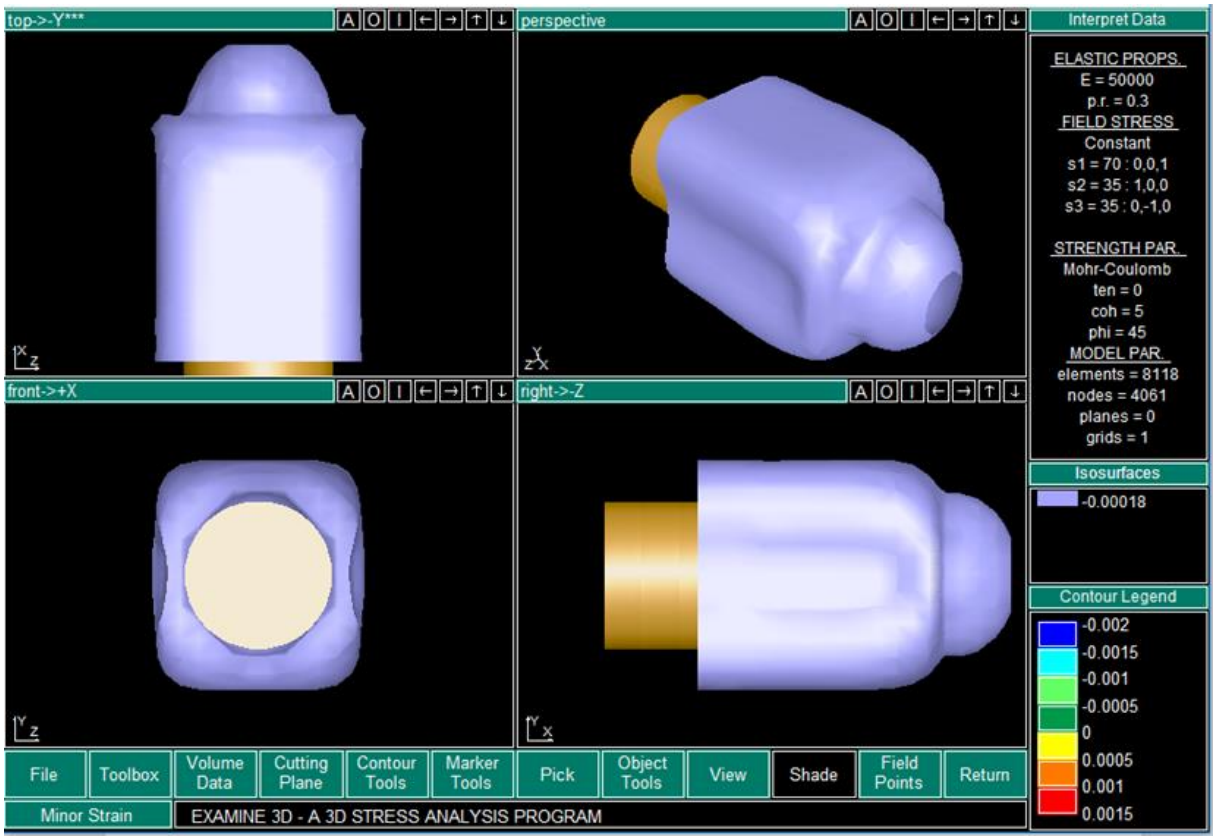


Figure 8.1.4: Isosurfaces of fracture/crack initiation for an eight-metre tunnel for Poisson's ratio of 0.3.

Table 8.1.1: Summary of slab thickness, slenderness ratios, buckling stresses

In Situ Stresses							
σx= 35 MPa, σy= 17,5 MPa, σz= 52,5 MPa							
Diameter, L(m)	σ3 (MPa)	σ1 (MPa)	h/L or l/t	h or t (m)	(l/t)	σb (MPa)	σ1/σ3
2	15,8	50	0,032	0,063	31,515	41,405	3,16
4	15	60	0,035	0,139	28,769	49,686	4,00
6	28,5	70	0,038	0,225	26,635	57,967	2,46
8	15	75	0,039	0,311	25,732	62,108	5,00

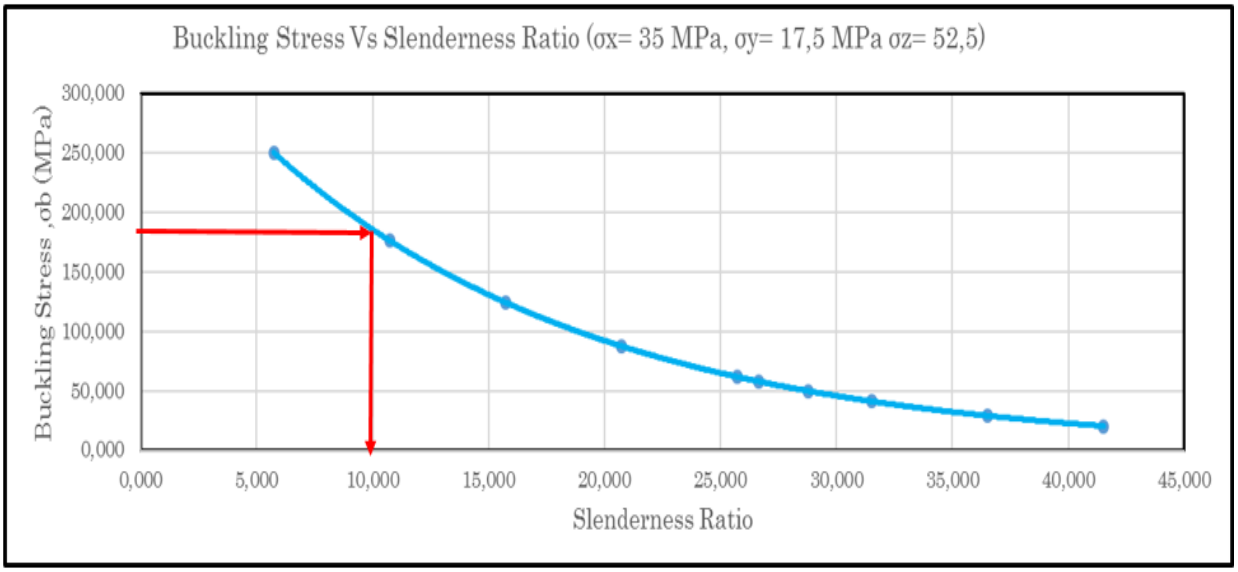


Figure 8.1.5: Buckling stress versus slenderness ratio for buckling failure using

Table 8.1.2: Summary of the results from Examine3D

Diameter (m)	σx= 70 MPa σy= 35 MPa σz= 70 MPa(v =0,2)			
	Extent of Fracturing	Principal Stresses around a fractured Zone		
		σ1(MPa)	σ3(MPa)	σ1/σ3
2	0	65	30	2,17
4	0	70	31,5	2,22
6	0,2	80	28	2,86
8	0,25	90	30	3,00
Diameter (m)	σx=35 MPa σy=17,5 MPa σz=52,5 MPa (v=0,2)			
εc=200 µstrai	Extent of Fracturng	Principal Stresses around a fractured Zone		
		σ1(MPa)	σ3(MPa)	
2	0	50	15,8	3,16
4	0	60	15	4,00
6	0,18	70	28,5	2,46
8	0,75	75	15	5,00
Diameter (m)	σx= 35 MPa σy= 35 MPa σz= 70 MPa (v=0,2)			
εc=200 µstrai	Extent of Fracturing	Principal Stresses around a fracture Zone		
		σ1(MPa)	σ3(MPa)	
2	0	70	33	2,12
4	0	70	33	2,12
6	0,3	90	28,5	3,16
8	0,29	100	15	6,67
Diameter (m)	σx=70 MPa σy= 35 MPa σz= 70 MPa (v =0,3)			
εc=200 µstrai	Extent of Fracturng	Principal Stresses around a fractured Zone		
		σ1(MPa)	σ3(MPa)	σ1/σ3
2	0,5	65	30	2,17
4	0,55	70	31,5	2,22
6	0,63	80	28	2,86
8	0,63	90	30	3,00
Diameter (m)	σx= 35 MPa σy= 17,5 MPa σz=52,5 MPa (v=0,3)			
εc=200 µstrai	Extent of Fracturing	Principal Stresses around a fractured Zone		
		σ1(MPa)	σ3(MPa)	
2	0,45	50	15,8	3,16
4	0,75	60	15	4,00
6	0,67	70	28,5	2,46
8	0,75	75	15	5,00
Diameter (m)	σx= 35 MPa σy= 35 MPa σz= 70 MPa (v=0,3)			
εc=200 µstrai	Extent of Fracturing	Principal Stresses around a fractured Zone		
		σ1(MPa)	σ3(MPa)	
2	0	70	33	2,12
4	0,4	70	33	2,12
6	0,5	90	28,5	3,16
8	0,5	100	15	6,67

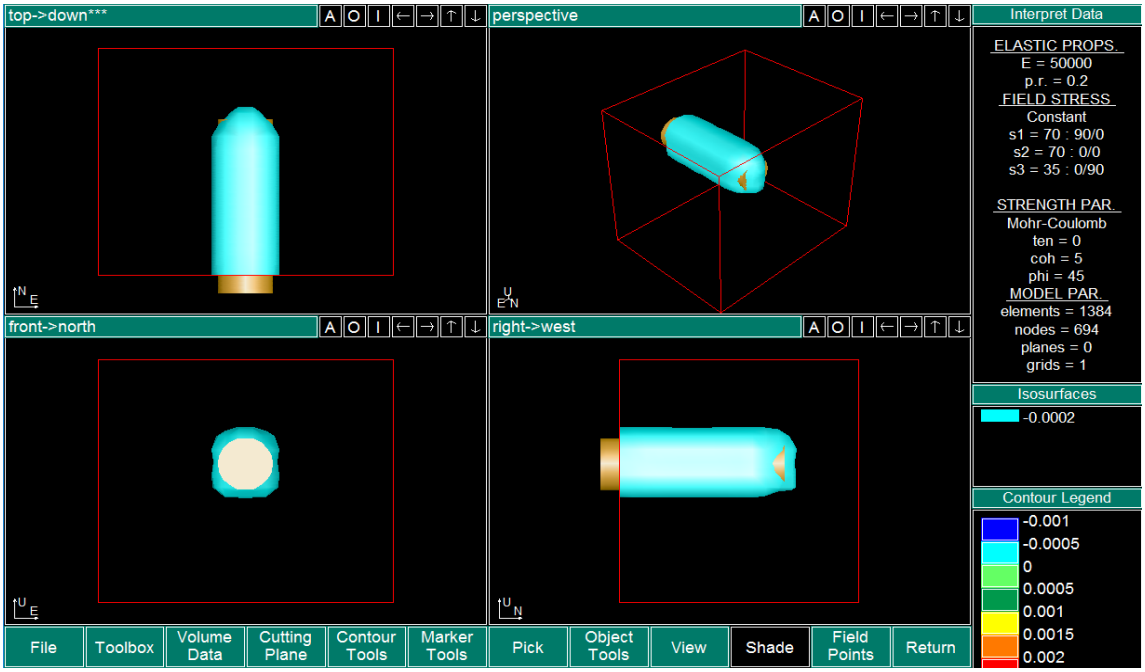


Figure 8.1.6: Isosurfaces for critical strain of 200 microstain on a four-metre tunnel depicting fractured zone

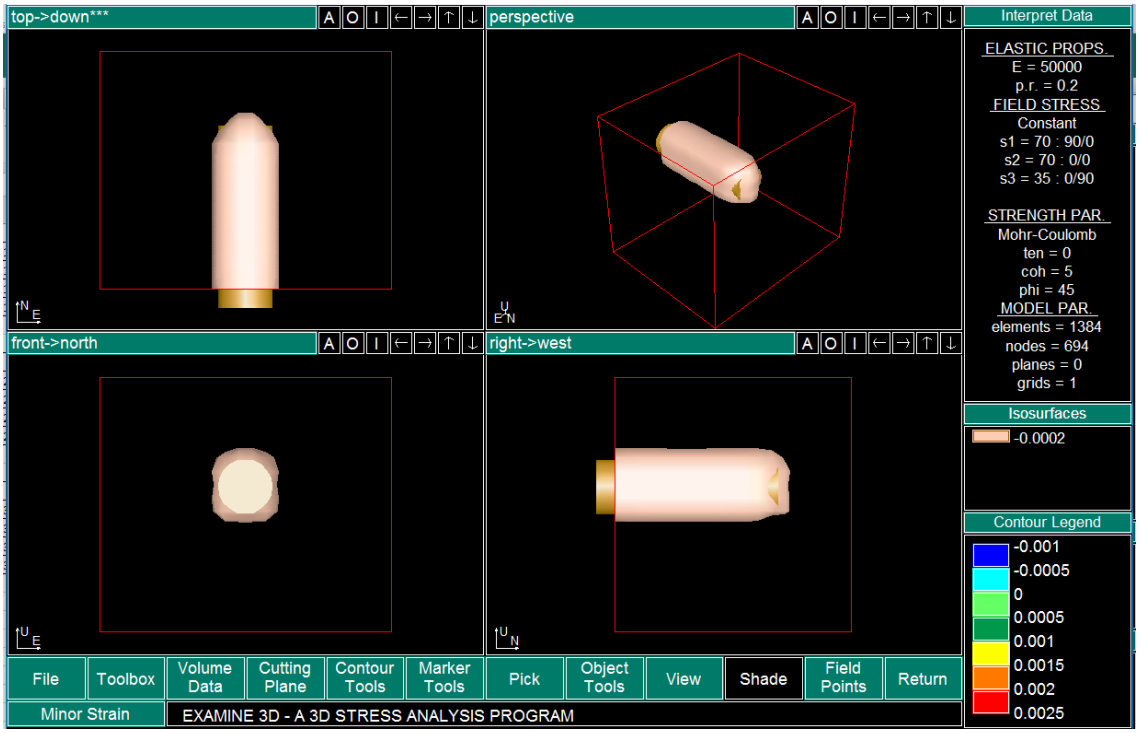


Figure 8.1.7: Isosurfaces for critical strain of 200 microstain on a six-metre tunnel depicting fractured zone

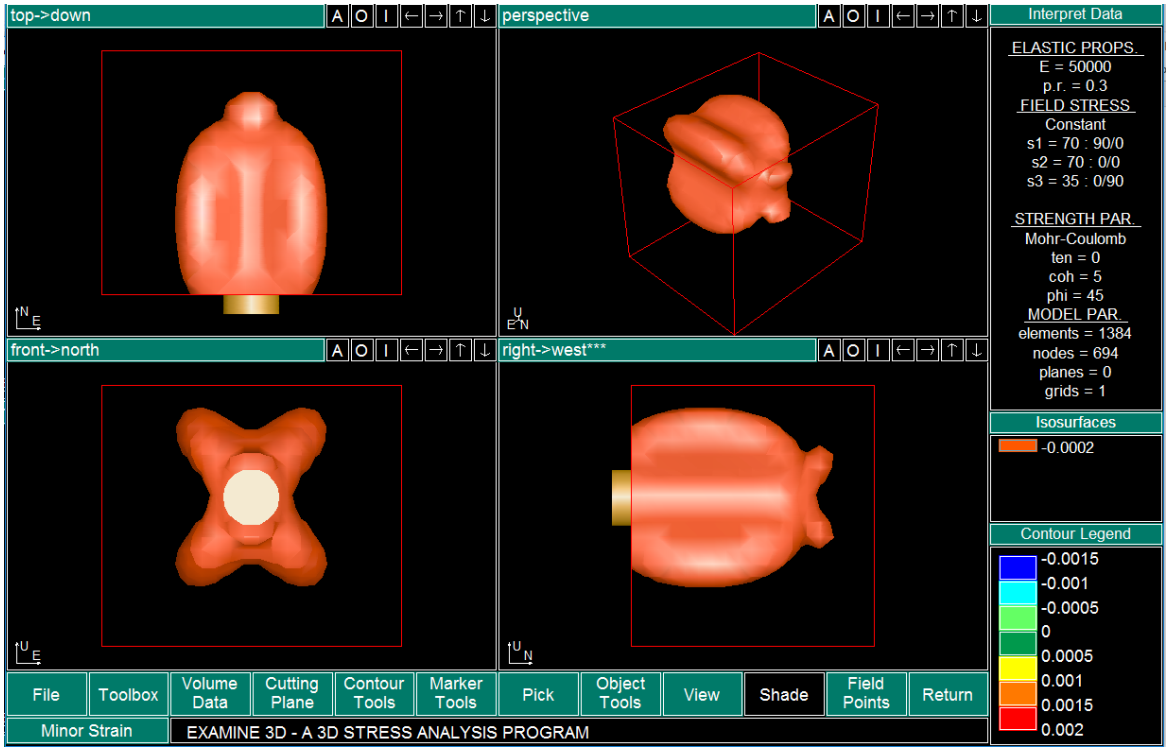


Figure 8.1.8: Isosurfaces for critical strain of 200 microstain on a six-metre tunnel depicting fractured zone.